Using Lidar to Enhance Understanding of Terrestrial Ecosystem Structure

Dafeng Zhang

A dissertation submitted to the Graduate School of Brown University in fulfillment of the requirements for the degree of Doctor of Philosophy in the Department of Ecology, Evolution, and Organismal Biology

Providence, RI

October 2024

© Copyright 2024 by Dafeng Zhang

This dissertation by Dafeng Zhang is accepted in its present form

by the Department of Ecology, Evolution, and Organismal Biology as satisfying the

dissertation requirements for the degree of Doctor of Philosophy.

Date_____ _____

James R. Kellner, Advisor

Recommended to the Graduate Council

Date_____ _____

Matthew Harrison, Reader

Date_____ _____

John F. Mustard, Reader

Date_____ _____

Stephen Porder, Reader

Date_____ _____

Sohini Ramachandran, Reader

Approved by the Graduate Council

Date_____ _____

Thomas A. Lewis, Dean of the Graduate School

Dafeng Zhang

dafeng_zhang@brown.edu

PhD Candidate, Kellner Lab

Institute at Brown for Environment and Society

Ecology, Evolution and Organismal Biology, Brown University

RESEARCH INTERESTS

I am broadly interested in understanding the response of terrestrial ecosystems to changing climate and intensified human activities. I approached this in my PhD thesis from the perspective of ecosystem structure and carbon using lidar data. Research in my dissertation chapters span from investigating how to obtain ecosystem structure measurements from drone lidar, improving aboveground biomass density data product using spaceborne lidar (GEDI), to understanding the human activities and the physical environment in explaining the variability of global ecosystem structure.

EDUCATION

Brown University

Ecology, Evolution and Organismal Biology (2019-present)

University of Chinese Academy of Sciences

M.ENG. in Surveying and Mapping Engineering (2016-2019)

Beijing University of Civil Engineering and Architecture

B.ENG. in Geographical Information System (2012-2016)

PUBLICATIONS

1. **Dafeng Zhang**, Kamil Král, Martin Krůček, KC Cushman, James R. Kellner. Near-Complete Sampling of Forest Structure from High-Density Drone Lidar Demonstrated by Ray Tracing. *Remote Sensing*. 2024, 16 (15): 2774.
2. **Dafeng Zhang**, Jianli Liu, Wenjian Ni, Guoqing Sun, Zhiyu Zhang, Qinhuo Liu, Qiang Wang. Estimation of Forest Leaf Area Index Using Height Information Extracted from Unmanned Aerial Vehicle Stereo Imagery. *IEEE Journal of Selected Topics in Applied Earth Observations and Remote Sensing*. 2019, 12 (2): 471-481.
3. Wenjian Ni, **Dafeng Zhang**, et. al. Extraction of Forest Height by Using GF-2 cross-track Stereo Images. *Journal of Remote Sensing*. 2018, 22 (3):392-399.
4. Wenjian Ni, Guoqing Sun, Yong Pang, Zhiyu Zhang, Jianli Liu, Aqiang Yang, Yao Wang,

Dafeng Zhang. Mapping Three-Dimensional Structures of Forest Canopy Using UAV Stereo Imagery: Evaluating Impacts of Forward Overlaps and Image Resolutions with LiDAR Data as Reference, *IEEE Journal of Selected Topics in Applied Earth Observations and Remote Sensing*. 2018, 11 (10):3578-3589.

5. Yao Wang, Wenjian Ni, Zhiyu Zhang, Jianli Liu, Haoyang Yu, **Dafeng Zhang**. Retrieval of Forest Canopy Heights by Using Large-footprint Waveform Data Assisted by the LiDAR Model over Hillsides. *Journal of Remote Sensing*. 2017, 22 (3):466-477.
6. Yao Wang, Zhiyu Zhang, Wenjian Ni, Jianli Liu, **Dafeng Zhang**. Comparison of Filter Algorithms and Combination Analysis for DEM Extracting Based on Airborne Laser Scanning Point Clouds. *Journal of Beijing Forestry University*. 2017, 39 (12):25-35.

PUBLICATIONS UNDER REVIEW OR IN PREPARATION

7. **Dafeng Zhang** and James R. Kellner. Human impacts on global terrestrial ecosystem structure (in prep)
8. **Dafeng Zhang**, Mona Khoshnevis, Matthew Harrison, Eugene Seo, Laura Duncanson, John Armston, James R. Kellner, and many other collaborators who provided the training data for the GEDI L4A data product. Interrogation of the GEDI aboveground biomass density data product: evaluation of prediction strata (in prep for *Environmental Research Letters*)
9. Maya Weissman, **Dafeng Zhang**, Rebecca Kartzinel, Daniel Weinreich. Balancing the risks of mating: biogeographic evidence of cleistogamy as a bet hedging strategy (submitted to *Evolution*)

RESEARCH EXPERIENCES

09/2019-present Kellner Lab (PI: James R. Kellner)

- Quantify the sampling capability of high-resolution drone lidar with ray tracing in temperate forests in Czech Republic
- Physical and anthropogenic drivers of terrestrial ecosystem structure from GEDI across the world's ecoregions
- Improvements on the GEDI aboveground biomass density data product

09/2016-06/2019 Master's Program (PI: Wenjian Ni)

- Quantification of forest structural parameters using drone stereoscopic images
- Large-scale canopy cover mapping based on individual tree segmentation
- Assisting the angle demonstration for a carbon monitoring satellite in China

- Drone and ground surveys in boreal and temperate forests in Northeastern China (350km east-west, 800km south-north, three times)

12/2015-05/2016 Honor Senior Thesis (Advisor: Shuqiang Lv)

- Unmixing of pigments in cultural relics using hyperspectral data

PRESENTATIONS

- How 3D information from lidar helps us better understand terrestrial ecosystems? Remote presentation at Quantitative Ecosystem Dynamics Lab at UC Berkeley 2024
- Evaluation of prediction strata in the GEDI04_A aboveground biomass density data product. **Dafeng Zhang**, Matthew Harrison, Eugene Seo, Mona Khoshnevis, Laura Duncanson, John Armston, James R. Kellner. Poster presentation on American Geophysical Union fall meeting 2023
- Determinants of terrestrial ecosystem structure from spaceborne lidar in temperate and tropical ecoregions. **Dafeng Zhang** and James R. Kellner. Poster presentation on Ecological Society of America annual meeting 2023
- Anthropogenic and Physical Determinants of Ecosystem Structure from GEDI Lidar. **Dafeng Zhang** and James R. Kellner. Poster presentation on American Geophysical Union fall meeting 2022
- Oral presentation at the 21st Conference on Remote Sensing of China 2018
- National Graduate Forum of Remote Sensing and Geographic Information Science in China 2018

TEACHING/OUTREACH/SERVICE

- Public talk for Stories with Scientists session, the Division of BioMed, Brown University Summer 2024
- Teaching assistant for BIOL 0210: Diversity of Life Fall 2023
  More than 300 students, one of the three grad TAs
- Teaching assistant for BIOL 0210: Diversity of Life Fall 2019
  More than 300 students, one of the five grad TAs
- Earth Science curriculum development for Hope high school in DEEPS CORES outreach program Summer 2023
- The Sheridan Teaching Seminar: Reflective Teaching (Certificate I) Fall 2023
- Judge for Outstanding Student Presentation Awards on American Geophysical Union Fall

Meeting 2022

- Graduate Student Peer Mentor, Brown EEOB Fall 2022
- Department representative for Graduate Student Council general body meetings at Brown University 2021 & 2022
- Volunteer for World Geospatial Developers Conference (Beijing, China) 2015

FUNDING

- IBES Graduate student research and travel funds 2023
- EEOB Doctoral Dissertation Enhancement Grant 2023
- GSC Conference and Professional Development Travel Fund 2022 & 2023
- Brown University BioMed Conference Travel Funding 2022 & 2023

AWARDS

- The Merit Student of University of Chinese Academy of Sciences 2017 & 2018
- Outstanding Graduates in Beijing 2016
- The 3rd prize of National GIS Applied Skills Competition for College Students 2015
- The 2nd prize of National English Contest for College Students 2014
- The 1st-class scholarship of Beijing University of Civil Engineering & Architecture 2013 & 2014
- The Merit Student of Beijing University of Civil Engineering &Architecture 2013 & 2014

PROGRAMMING/COMPUTING/SOFTWARES

R, Bash, MATLAB, Python, ENVI/IDL, ArcGIS/ArcPy, Agisoft Metashape, Google Earth Engine, High Performance Computing

PREFACE

Ecosystem structure, or vegetation structure, is the arrangement and distribution of vegetation material in three-dimensional space within an ecosystem (Gils and Wijngaarden, 1984; Graetz, 1990). It is a fundamental property of terrestrial ecosystems (Spies, 1998; Migliavacca et al., 2021), and is both an essential determinant and a result of ecosystem functioning and biodiversity (MacArthur and MacArthur, 1961; Graetz, 1990; Spies, 1998; Béland and Baldocchi, 2021; Novella-Fernandez et al., 2022). Understanding the variability in ecosystem structure is critical in projecting the response of terrestrial ecosystems to climate change (Li et al., 2023; Ma et al., 2023).

Our understanding of terrestrial ecosystem structure has been confined by the availability of data. Earliest ecological studies tend to describe the variability in ecosystem structure by at most four layers (i.e., stratification): the emergent layer, the canopy, the understory, and the forest floor (Smith, 1973). Our understanding of the variation in ecosystem structure from traditional ecological studies is mostly based on sites of up to a few hundred square kilometers in area (Clark and Clark, 2000; Higgins et al., 2015).

Airborne and spaceborne lidar instruments alleviate the limitation by generating direct ecosystem structure measurements throughout the canopy height profile and by characterizing ecosystem structure at finer vertical resolutions across the world's terrestrial biomes (Tang et al., 2019; Kellner et al., 2019; Dubayah et al., 2020, 2022; Akturk et al., 2023; Ma et al., 2024). Different dimensions (e.g., vertical, horizontal) and various perspectives (e.g., leaf area, mass) of ecosystem structure can be characterized by lidar data through structure metrics. For example, height that represents vertical structure (Lang et al., 2022) and foliage height diversity (FHD) that represents the heterogeneity of vertical structure (Dubayah et al., 2021), cover that

represents the horizontal distribution of vegetation (Akturk et al., 2023; Tang et al., 2019), plant area index (PAI) (or leaf area index if leaves and stems are distinguished) or aboveground biomass density (AGBD) that depict ecosystem structure from a more synthesized dimension (Dubayah et al., 2022; Ma et al., 2024). Such structure metrics are widely used to understand and predict the past, current and future of terrestrial ecosystems under changing climate and intensified human land use (Le Toan et al., 2011; Chen et al., 2019; Ma et al., 2023; Li et al., 2023).

Although ecosystem structure has been characterized by lidar data from different perspectives and across various spatial scales as mentioned above, there are two major limitations on our understanding of the variation in ecosystem structure using lidar. First, the measurement characteristics and algorithms used to quantify the structure metrics could influence our conclusions about ecosystem structure (Kellner et al., 2019; Brede et al., 2022). Second, it is unclear if the variability of ecosystem structure is still primarily predicted by the physical environment considering the widespread human modification to global land surface (Brandt et al., 2017; Song et al., 2018)

The objective of my dissertation is to enhance our understanding of terrestrial ecosystem structure using lidar by addressing the limitations. My dissertation asks the question, what explains the variation in ecosystem structure, and answers it from two perspectives with three chapters: (1) measurement characteristics and algorithms, (2) the role of human impacts and the physical environment in explaining the variation in ecosystem structure.

In chapter 1, I used high density drone lidar data in the Czech Republic to disentangle the impact of two measurement characteristics on obtaining complete samples of forests. I used ray-tracing in voxel space to quantify the sampling completeness under different measurement

characteristics throughout the canopy height profile. I found that, although the drone lidar data searched 98.1% of the voxels, there were three ways a voxel could be undetected and they all existed in the drone lidar data. Voxels that were searched but did not trigger a return existed both at near-ground and canopy top, even when pulse density was as great as 1000 pulses /m^2. I also found that the impact of scan-angle range was limited when it was decoupled from pulse density. This research advances our understanding of the impact of measurement characteristics on drone lidar sampling and demonstrates the importance of using ray-tracing to assess the sampling completeness of drone lidar.

In chapter 2, I explored the role of human impacts and the physical environment in explaining the variation in ecosystem structure using various environmental and socio-economic datasets that represent the physical environment and human impacts. I linked them to structure metrics from a spaceborne lidar across the world's regions covering different terrestrial ecosystems and human activities. I used a machine learning model and permutation analyses to investigate if human impacts add additional explanatory power to the variability of ecosystem structure. I found human impacts did not add much additional explanatory power. I tested three hypotheses that explained the result and found that, although human impacts explained some variation in ecosystem structure, an explanation for the result was the limited number of anthropogenic variables and the correlation between physical variables and anthropogenic variables. The results suggest that it is not feasible to disentangle human and physical impacts in some regions based on the data we have. This chapter demonstrated the necessity of checking some assumptions when using global environment and socio-economic datasets to explain the variability in ecosystem structure.

In chapter 3, I interrogated the current aboveground biomass density (AGBD) data product from Global Ecosystem Dynamics Investigation (GEDI) by examining the prediction strata used for the AGBD models. To examine if there was within-strata variation in the relationship between structure metrics and AGBD, I developed local models within geographic subsets of current prediction strata. I checked the difference of the local models within each prediction stratum by checking model coefficients statistically and by comparing model predictions. I used on-orbit GEDI footprints to predict AGBD based on the local models and used three types of regularized models to avoid extreme predictions. I found within-strata variation in current prediction strata, which suggests the heterogeneity of the relationship between AGBD and structure in current prediction strata. The research provides insights to the next version of the AGBD data product from GEDI.

To conclude, my dissertation enhanced our understanding of the variation in global ecosystem structure using lidar. I developed a method to quantify the sampling capability of drone lidar with ray-tracing and disentangled the impact of important measurement characteristics on sampling completeness (chapter 1). I interrogated the algorithm stratification of current AGBD data product from GEDI and found that the relationship between structure and biomass may be more complex than the current stratification by continent and plant functional type (chapter 3). I explored the impact of human activities in comparison to the physical environment in explaining the spatial variation in ecosystem structure and found that it is hard to disentangle human and physical impacts due to the redundancy and the degree of informativity of the anthropogenic variables in comparison to physical variables.

References

Akturk, E., Popescu, S.C., Malambo, L., 2023. ICESat-2 for Canopy Cover Estimation at Large-Scale on a Cloud-Based Platform. Sensors 23, 3394. https://doi.org/10.3390/s23073394

Béland, M., Baldocchi, D.D., 2021. Vertical structure heterogeneity in broadleaf forests: Effects on light interception and canopy photosynthesis. Agric. For. Meteorol. 307, 108525. https://doi.org/10.1016/j.agrformet.2021.108525

Brandt, M., Rasmussen, K., Peñuelas, J., Tian, F., Schurgers, G., Verger, A., Mertz, O., Palmer, J.R.B., Fensholt, R., 2017. Human population growth offsets climate-driven increase in woody vegetation in sub-Saharan Africa. Nat. Ecol. Evol. 1, 1–6. https://doi.org/10.1038/s41559-017-0081

Brede, B., Bartholomeus, H.M., Barbier, N., Pimont, F., Vincent, G., Herold, M., 2022. Peering through the thicket: Effects of UAV LiDAR scanner settings and flight planning on canopy volume discovery. Int. J. Appl. Earth Obs. Geoinformation 114, 103056. https://doi.org/10.1016/j.jag.2022.103056

Chen, C., Park, T., Wang, X., Piao, S., Xu, B., Chaturvedi, R.K., Fuchs, R., Brovkin, V., Ciais, P., Fensholt, R., Tømmervik, H., Bala, G., Zhu, Z., Nemani, R.R., Myneni, R.B., 2019. China and India lead in greening of the world through land-use management. Nat. Sustain. 2, 122–129. https://doi.org/10.1038/s41893-019-0220-7

Clark, D.B., Clark, D.A., 2000. Landscape-scale variation in forest structure and biomass in a tropical rain forest. For. Ecol. Manag. 137, 185–198. https://doi.org/10.1016/S0378-1127(99)00327-8

Dubayah, R., Armston, J., Healey, S.P., Bruening, J.M., Patterson, P.L., Kellner, J.R., Duncanson, L., Saarela, S., Ståhl, G., Yang, Z., Tang, H., Blair, J.B., Fatoyinbo, L., Goetz, S., Hancock, S., Hansen, M., Hofton, M., Hurtt, G., Luthcke, S., 2022. GEDI

launches a new era of biomass inference from space. Environ. Res. Lett. 17, 095001. https://doi.org/10.1088/1748-9326/ac8694

Dubayah, R., Blair, J.B., Goetz, S., Fatoyinbo, L., Hansen, M., Healey, S., Hofton, M., Hurtt, G., Kellner, J., Luthcke, S., Armston, J., Tang, H., Duncanson, L., Hancock, S., Jantz, P., Marselis, S., Patterson, P.L., Qi, W., Silva, C., 2020. The Global Ecosystem Dynamics Investigation: High-resolution laser ranging of the Earth's forests and topography. Sci. Remote Sens. 1, 100002. https://doi.org/10.1016/j.srs.2020.100002

Dubayah, R., Tang, H., Armston, J., Luthcke, S., Hofton, M., Blair, J., 2021. GEDI L2B Canopy Cover and Vertical Profile Metrics Data Global Footprint Level V002. https://doi.org/10.5067/GEDI/GEDI02_B.002

Gils, H.V., Wijngaarden, W.V., 1984. Vegetation structure in reconnaissance and semi-detailed vegetation surveys. ITC J. 213–218.

Graetz, R.D., 1990. Remote Sensing of Terrestrial Ecosystem Structure: An Ecologist's Pragmatic View, in: Hobbs, R.J., Mooney, H.A. (Eds.), Remote Sensing of Biosphere Functioning, Ecological Studies. Springer, New York, NY, pp. 5–30. https://doi.org/10.1007/978-1-4612-3302-2_2

Higgins, M.A., Asner, G.P., Anderson, C.B., Martin, R.E., Knapp, D.E., Tupayachi, R., Perez, E., Elespuru, N., Alonso, A., 2015. Regional-Scale Drivers of Forest Structure and Function in Northwestern Amazonia. PLOS ONE 10, e0119887. https://doi.org/10.1371/journal.pone.0119887

Kellner, J.R., Armston, J., Birrer, M., Cushman, K.C., Duncanson, L., Eck, C., Falleger, C., Imbach, B., Král, K., Krůček, M., 2019. New opportunities for forest remote sensing through ultra-high-density drone lidar. Surv. Geophys. 40, 959–977.

Lang, N., Kalischek, N., Armston, J., Schindler, K., Dubayah, R., Wegner, J.D., 2022. Global canopy height regression and uncertainty estimation from GEDI LIDAR waveforms with deep ensembles. Remote Sens. Environ. 268, 112760. https://doi.org/10.1016/j.rse.2021.112760

Le Toan, T., Quegan, S., Davidson, M.W.J., Balzter, H., Paillou, P., Papathanassiou, K., Plummer, S., Rocca, F., Saatchi, S., Shugart, H., Ulander, L., 2011. The BIOMASS mission: Mapping global forest biomass to better understand the terrestrial carbon cycle. Remote Sens. Environ., DESDynI VEG-3D Special Issue 115, 2850–2860. https://doi.org/10.1016/j.rse.2011.03.020

Li, W., Guo, W.-Y., Pasgaard, M., Niu, Z., Wang, L., Chen, F., Qin, Y., Svenning, J.-C., 2023. Human fingerprint on structural density of forests globally. Nat. Sustain. 6, 368–379. https://doi.org/10.1038/s41893-022-01020-5

Ma, L., Hurtt, G., Tang, H., Lamb, R., Lister, A., Chini, L., Dubayah, R., Armston, J., Campbell, E., Duncanson, L., Healey, S., O'Neil-Dunne, J., Ott, L., Poulter, B., Shen, Q., 2023. Spatial heterogeneity of global forest aboveground carbon stocks and fluxes constrained by spaceborne lidar data and mechanistic modeling. Glob. Change Biol. 29, 3378–3394. https://doi.org/10.1111/gcb.16682

Ma, L., Yu, D., Chen, Y., Feng, K., Tang, H., Sumnall, M.J., Zheng, G., 2024. Quantifying the Plant Area Index of Overstory and Understory Vegetation on Sloped Terrain Using Single-Station Terrestrial Laser Scanner. IEEE Trans. Geosci. Remote Sens. 62, 1–19. https://doi.org/10.1109/TGRS.2024.3395584

MacArthur, R.H., MacArthur, J.W., 1961. On Bird Species Diversity. Ecology 42, 594–598. https://doi.org/10.2307/1932254

Migliavacca, M., Musavi, T., Mahecha, M.D., Nelson, J.A., Knauer, J., Baldocchi, D.D., Perez-Priego, O., Christiansen, R., Peters, J., Anderson, K., Bahn, M., Black, T.A., Blanken, P.D., Bonal, D., Buchmann, N., Caldararu, S., Carrara, A., Carvalhais, N., Cescatti, A., Chen, J., Cleverly, J., Cremonese, E., Desai, A.R., El-Madany, T.S., Farella, M.M., Fernández-Martínez, M., Filippa, G., Forkel, M., Galvagno, M., Gomarasca, U., Gough, C.M., Göckede, M., Ibrom, A., Ikawa, H., Janssens, I.A., Jung, M., Kattge, J., Keenan, T.F., Knohl, A., Kobayashi, H., Kraemer, G., Law, B.E., Liddell, M.J., Ma, X., Mammarella, I., Martini, D., Macfarlane, C., Matteucci, G., Montagnani, L., Pabon-Moreno, D.E., Panigada, C., Papale, D., Pendall, E., Penuelas, J., Phillips, R.P., Reich, P.B., Rossini, M., Rotenberg, E., Scott, R.L., Stahl, C., Weber, U., Wohlfahrt, G., Wolf, S., Wright, I.J., Yakir, D., Zaehle, S., Reichstein, M., 2021. The three major axes of terrestrial ecosystem function. Nature 598, 468–472. https://doi.org/10.1038/s41586-021-03939-9

Novella-Fernandez, R., Juste, J., Ibañez, C., Nogueras, J., Osborne, P.E., Razgour, O., 2022. The role of forest structure and composition in driving the distribution of bats in Mediterranean regions. Sci. Rep. 12, 3224. https://doi.org/10.1038/s41598-022-07229-w

Smith, A.P., 1973. Stratification of Temperature and Tropical Forests. Am. Nat. 107, 671–683. https://doi.org/10.1086/282866

Song, X.-P., Hansen, M.C., Stehman, S.V., Potapov, P.V., Tyukavina, A., Vermote, E.F., Townshend, J.R., 2018. Global land change 1982-2016. Nature 560, 639–643. https://doi.org/10.1038/s41586-018-0411-9

Spies, T.A., 1998. Forest structure: a key to the ecosystem. Northwest Sci. 72, 34–36.

Tang, H., Armston, J., Hancock, S., Marselis, S., Goetz, S., Dubayah, R., 2019. Characterizing global forest canopy cover distribution using spaceborne lidar. Remote Sens. Environ. 231, 111262. https://doi.org/10.1016/j.rse.2019.111262

Acknowledgments

Pursuing a PhD degree is a journey full of challenges and growth. I felt lucky and grateful every time when I thought of the people I have met on this journey. I have learned more than I expected from them and I am grateful for all the support and help.

First and foremost, thank my advisor, Jim Kellner, for being a supportive and encouraging advisor no matter what challenges I faced. I learned a lot from him, not only about how to do research, but also about how to be professional and confident as a scientist. Thank my committee members, Matthew Harrison, John F. Mustard, Stephen Porder, Sohini Ramachandran for their insightful input on my research. Thank IBES and EEOB staff, especially Henry Johnson and Serena Burt, for administrative support and Center for Computation and Visualization at Brown University, especially Ashok Ragavendran, for computational support. Thank my collaborators, KC Cushman, Kamil Král, Martin Krůček, Mona Khoshnevis, Eugene Seo, current and former Kellner Lab and Porder Lab members, John Burley, Loren Albert, Ahya Rezaei, Lindsay McCulloch, Audrey Massmann, for all the input and feedback on my projects. Thank IBES and EEOB friends, Natasha Sekhon, Sonam Sherpa, Aryan Jakhar, Jada Ko, Ji Soo Hong, Maya Weissman, Ezequiel Vanderhoeven, Ziang Liu, for being pleasant company in IBES, WH or off campus. I enjoyed our conversations about research and life, and I would miss those days.

Thank my friends, Kexin Qu, Ranran Chen, Sophia Song, Wenjun Ma, Xi Chen, and furry friends, Ke Le, Mochi, Jackie, Sumac for delightful presence. It was so joyful to spend time

with you all. Thank my parents and my grandparents who have supported what I planned to pursue and especially my mom, who is always open-minded and supportive. Her positive attitude to life has encouraged me along the way.

Lastly, I would like to thank myself for being persistent, resilient, and mentally positive in such a journey full of intellectual and personal challenges.

TABLE OF CONTENTS

LIST OF TABLES

CHAPTER 1

CHAPTER 2

CHAPTER 3

LIST OF ILLUSTRATIONS

CHAPTER 1

CHAPTER 2

CHAPTER 3

CHAPTER 1

Nearly-complete sampling of forest structure from high-density drone lidar demonstrated by ray tracing

Dafeng Zhang[1,2], Kamil Král[3], Martin Krůček[3], KC Cushman[1,2,4], James R. Kellner[1,2]

1. Department of Ecology, Evolution and Organismal Biology, Brown University, Providence RI, 02912, United States of America

2. Institute at Brown for Environment and Society, Brown University, Providence RI, 02912, United States of America

3. Department of Forest Ecology, The Silva Tarouca Research Institute, 60200 Brno, Czech Republic

4. Environmental Sciences Division, Oak Ridge National Laboratory, Oak Ridge TN, 37830, United States of America

Modified from publication in *Remote Sensing* (2024), 16 (15): 2774

Abstract

Drone lidar has the potential to provide detailed measurements of vertical forest structure throughout large areas. But a systematic evaluation of unsampled forest structure in comparison to independent reference data has not been performed. Here we used ray tracing on a high-resolution voxel grid to quantify sampling variation in a temperate mountain forest in the southwest Czech Republic. We decoupled the impact of pulse density and scan-angle range on the likelihood of generating a return using spatially and temporally coincident TLS data. We show three ways that a return can fail to be generated in the presence of vegetation: first, voxels can be searched without producing a return, even when vegetation is present; second, voxels can be shadowed (occluded) by other material in the beam path, preventing a pulse from searching a given voxel; and third, some voxels are unsearched because no pulse was fired in that direction. We show that all three types exist, and that the proportion of each of them varies with pulse density and scan-angle range throughout the canopy height profile. Across the entire data set, 98.1% of voxels known to contain vegetation from a combination of coincident drone lidar and TLS data were searched by low-altitude drone lidar, and 81.8% of voxels that were occupied by vegetation generated at least one return. By decoupling the impacts of pulse density and scan angle range, we show that sampling completeness is more sensitive to pulse density than to scan angle range. There are important differences in the causes of sampling variation that change with pulse density, scan angle range, and canopy height. Our findings demonstrate the value of ray tracing to quantifying sampling completeness in drone lidar.

Keywords: forest; drone; lidar; voxel; ray tracing; terrestrial laser scanning

1. Introduction

Forests are important terrestrial ecosystems covering 31% of the terrestrial land surface and accounting for 75% of terrestrial gross primary production (Beer et al., 2010; Pan et al., 2013; FAO and UNEP, 2020). Lidar observations of forests are essential for deriving key traits (e.g., leaf area index), depicting tree morphology, and monitoring spatiotemporal changes (Coops et al., 2021; Disney et al., 2020; Li et al., 2017; Liu et al., 2019; Morsdorf et al., 2006; Olsoy et al., 2014; Pueschel et al., 2013; Roşca et al., 2018; X. Yang et al., 2013). Detailed lidar observations can also serve as independent estimates to calibrate and validate global data products from spaceborne lidar and radar missions (Committee on Earth Observation Satellites, 2021; Disney et al., 2019; Duncanson et al., 2019; Saatchi et al., 2011; Stovall and Shugart, 2018). The application of lidar observations in these studies has been advancing our understanding of the functioning of forest ecosystems and their roles in the carbon and water cycles under changing climates (Beland et al., 2019; Ma et al., 2023; Smith et al., 2019).

Terrestrial laser scanning (TLS), with its high point density, captures forest structure in great detail (Calders et al., 2020; Liang et al., 2016). It is therefore promising for accurately estimating aboveground biomass based on structural metrics such as diameter at breast height (DBH), various crown dimensions, and wood volume on as fine a level as the individual tree (Bornand et al., 2023; Calders et al., 2015; Dassot et al., 2012; Strahler et al., 2008; Wang et al., 2021; Zheng et al., 2013). Ground-based scanning tends to prevent laser pulses from reaching canopy tops, especially during leaf-on seasons in dense forests (Brede et al., 2017; Disney et al., 2019). Multiple scans from different locations can reduce occlusion, but the data acquisition can be labor-intensive and time-consuming for large areas and requires careful planning (Wilkes et al., 2017). Some regions may be inaccessible for acquiring extra scans, and scans may be influenced

by wind effects (Calders et al., 2014). Airborne laser scanning (ALS) generates more detailed measurements at upper canopies than at lower canopies (Chasmer et al., 2004; Brede et al., 2017), usually with much lower point density compared to TLS (LaRue et al., 2020). ALS observations or products are essential for scaling between field measurements and satellite data products (Saarela et al., 2020; Xu et al., 2017; Zhao et al., 2009).

Backpack and handheld laser scanning (Ryding et al., 2015; Bauwens et al., 2016; Hyyppä et al., 2020) have become popular due to their lower costs and greater mobility in comparison to TLS (Liang et al., 2014b). But they are still mostly used within small areas, since large-area mapping with these systems is labor-intensive, and most regions remain inaccessible. Mobile laser scanning (MLS), such as car-based systems or lidar onboard all-terrain vehicles (Liang et al., 2014a), can map larger areas than backpack or handheld lidar systems with less human labor (Jaakkola et al., 2010), but these approaches are more common in urban mapping (Yang et al., 2013) and have limited applications in forests (Bauwens et al., 2016).

Low-altitude drone lidar can produce point clouds with orders of magnitude greater sampling densities than traditional ALS (Brede et al., 2022; Calders et al., 2020; Kellner et al., 2019; Puliti et al., 2020; Qi et al., 2022; Resop et al., 2019) and can scan regions that are inaccessible on the ground (Barazzetti et al., 2023; Shui et al., 2022). Because sampling densities and scan-angle ranges are greater, drone lidar may be able to resolve understory structure that traditional ALS cannot. Overlapping flight lines from low-altitude drones, analogous to multiple TLS scans from different locations, can significantly increase the observed canopy volume due to greater scan-angle ranges and pulse densities (Pueschel et al., 2013; Kükenbrink et al., 2017; Kellner et al., 2019; Brede et al., 2022). However, it remains unknown how scan-angle ranges and pulse densities interact to influence the sampling properties of lidar data from airborne sensors

throughout the canopy height profile. Airborne sensors tend to acquire relatively few returns near the ground. But it remains unclear whether measurement characteristics can be modified to produce a more complete sample within canopy volume.

Ray tracing in voxel space, originally used for radiative transfer modeling in three dimensions (Cifuentes et al., 2014; Li et al., 2018; Magney et al., 2016; Musselman et al., 2013; Xie et al., 2018), is widely used to analyze TLS data (Béland et al., 2014, 2011; Bienert et al., 2010; Disney et al., 2006; Paynter et al., 2018; Stovall et al., 2017; Van der Zande et al., 2009; Zong et al., 2021). Fewer studies have applied ray tracing to ALS or drone lidar data (Dayal et al., 2022; Korpela et al., 2012; Morsdorf et al., 2007; Vincent et al., 2017). When ray tracing is employed, the path of each laser pulse is tracked as it travels through voxels (Amanatides and Woo, 1987). A return is generated when a laser pulse is reflected by vegetation or other material. In forests, voxels that contain a return are known to be occupied by vegetation. However, voxels that do not contain a return may be unoccupied, and therefore no return can be generated; or they can be occupied but not detected. Voxels that are occupied and not detected can exist in a lidar data set for a variety of reasons: they can be unsearched by laser pulses, for example, because pulse density is insufficient, occluded due to the presence of other occupied voxels within the beam path, or searched but not detected. A voxel can be searched and not detected when a laser pulse passes through empty space within an occupied voxel, or not enough laser energy is reflected to be recognized as a discrete return by post-processing algorithms.

We define sampling completeness, p, as the number of detected voxels divided by the number of voxels that are occupied. Sampling completeness is a ratio between 0 and 1:

$$p = \frac{n_{detected}}{n_{occupied}} \quad (1)$$

Its complement, sampling incompleteness, is $1 - p$. Sampling incompleteness can be represented by different types of undetected voxels. Few studies using ALS or drone lidar have used ray tracing to quantify different types of undetected voxels (Kükenbrink et al., 2017; Brede et al., 2022).

Here we use ray tracing to quantify sampling completeness using data from high-density drone lidar in a temperate mountain forest in the southwest Czech Republic. By using ultra-high-density measurements collected under a wide scan-angle range, we generate simulated datasets using subsampling to evaluate the consequences of different pulse densities and scan-angle ranges on sampling completeness. We benchmark understory to near-ground measurements from drone lidar using TLS data that was collected on the same day. We use this analysis to address four questions: (1) Is sampling completeness more sensitive to pulse density or scan-angle range? (2) How do different types of undetected voxels covary with pulse density and scan-angle range? (3) How does sampling completeness vary within the canopy height profile? (4) What kinds of undetected voxels are responsible for unsampled forest structure?

2. Materials and Methods

2.1 Drone lidar

We collected lidar data over a temperate mountain forest in the southern Czech Republic using a low-altitude drone (Kellner et al., 2019). The site contained the Zofin forest dynamics plot, a 25 ha permanent-inventory plot in which all free-standing woody plants with DBH greater than 1 cm were mapped and monitored since 2012 (Anderson-Teixeira et al., 2015; Janík et al., 2016). The forest was dominated by old-growth European beech (*Fagus sylvatica*) and Norway spruce (*Picea abies*), with occasional silver fir (*Abies alba*) (Cushman et al., 2023; Janík et al., 2016).

Data were collected using a RIEGL VUX-1 laser scanner coupled to an Oxford Technical Solutions (OxTS) Survey+2 GPS-IMU. The VUX-1 could record up to 500,000 measurements per second at a wavelength of 1,550 nm. The sensor recorded the return-time of emitted laser pulses and processed the recorded waveform to identify discrete reflective surfaces (returns) within every emitted laser pulse. It could record more than 3 returns per emitted pulse. The OxTS GPS-IMU was a survey-grade instrument designed for aerial mapping applications. The nominal roll and pitch accuracy were 0.03 degrees, and the nominal heading accuracy in dual-antenna mode was 0.05 degrees. During flight operations we collected an independent Global Navigation Satellite System (GNSS) data stream using a Novatel FlexPak 6 Triple Frequency + L-band GNSS receiver. We used this data stream to differentially correct the OxTS GPS-IMU measurements in post processing. A previous analysis demonstrated that post-processed range accuracy was less than 5 cm (one sigma) on a heterogeneous target (a fallen dead tree; Kellner et al., 2019).

The data were collected in two sets of orthogonal flight lines on June 6, 2018 under leaf-on conditions. There were 45 flight lines in the NW-SE direction, and 45 flight lines in the NE-SW direction (Figure 1A). We used two sets of flight lines over the same area to ensure high-density point coverage of stem and branch structure. The nominal flight altitude was 110 m aboveground, and the nominal flight speed was 6 m/s. The maximum scan-angle range was ± 60 degrees. Mean point density in the leaf-on point cloud was 2,166 points / m^2. We classified ground returns within the calibrated and georeferenced point cloud using a progressive morphological filter (Zhang et al., 2003) and excluded ground returns from the following analyses (Figure 2).

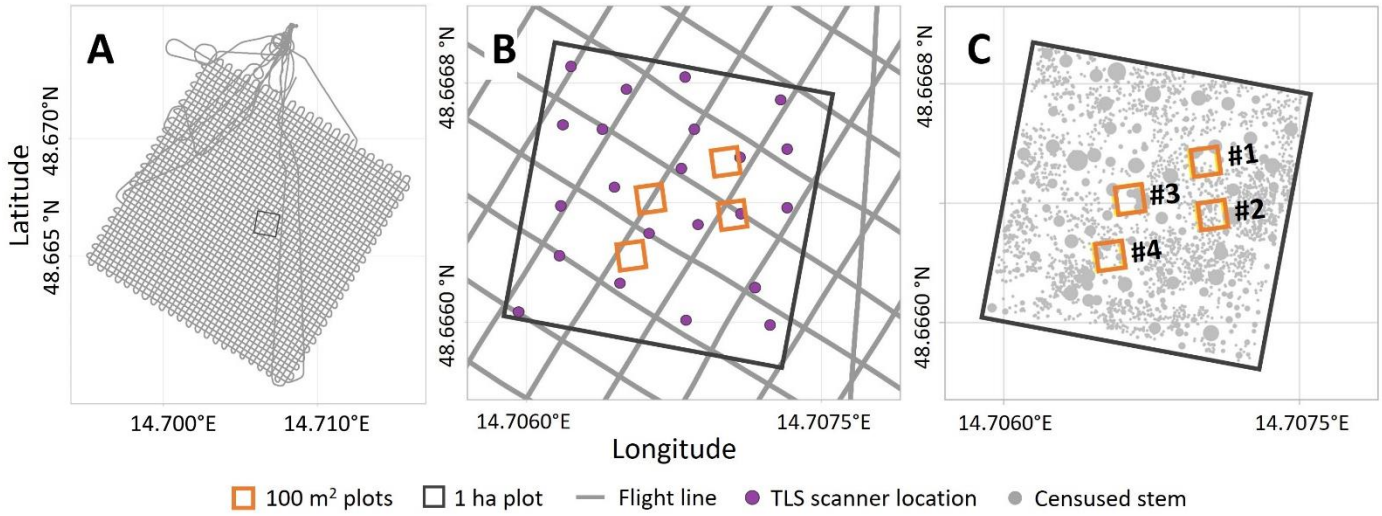

Figure 1. (A) Flight lines from drone lidar in a temperate mountain forest in the southwest Czech Republic. We completed two sets of orthogonal flight lines. (B) Locations of TLS scans and 100 m^2 plots used in this study. (C) The 100 m^2 plots used in this study in relation to censused stems. The point size of the censused stems is proportional to DBH.

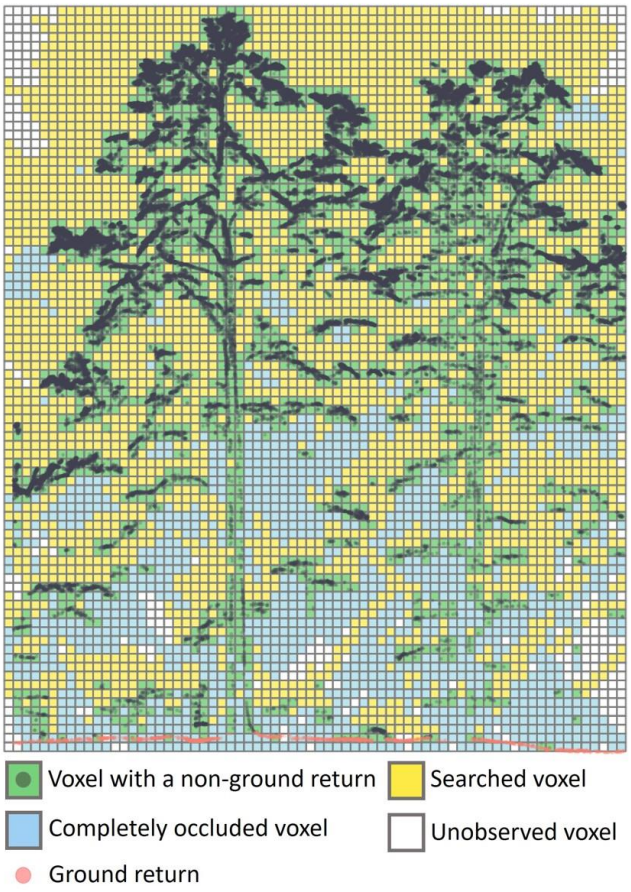

Figure 2. High-resolution forest structure from a low-altitude drone. Squares are 0.5 m voxels. Voxels were classified into four categories using non-ground returns from drone lidar: voxels with one or more returns (green), voxels that were searched by laser pulses and contain no return (yellow), voxels with only occluded pulses (blue), and voxels with no returns, laser pulses or occluded pulses (white). Grey dots on green voxels represent lidar returns. Darker grey dots indicate more returns in the voxel.

2.2 Terrestrial laser scanning

We collected TLS data within a 1 ha area at 22 scanning positions using a Leica P20 ScanStation on June 6, 2018 (Figure 1B). All TLS data were co-registered using ground-based reflective targets. The mean absolute co-registration error was 1 mm (Krůček et al., 2020). We

classified ground returns in the calibrated and georeferenced point cloud using the terrain-from-octree algorithm in 3D Forest (Trochta et al., 2017). We then manually co-registered TLS data to the drone lidar point cloud. To estimate the registration error between TLS and drone lidar data, we measured the distance between 20 pairs of TLS and drone lidar points in each of the four 100 m^2 plots (80 pairs in total) and calculated the arithmetic mean. The mean distance was 0.25 m, and the standard deviation was 0.2 m.

2.3 Ray tracing and voxel-traversal

We assessed the impact of pulse density and scan-angle range on detected and different types of undetected voxels using a grid with 0.5 m voxels. For each voxel, we determined whether the voxel was occupied by vegetation or not based on the union of the TLS and drone lidar points. Occupied voxels were voxels containing at least one return from TLS or drone lidar data. Part of our analysis was to investigate under what pulse density and scan-angle range the occupied voxels would be detected by simulating different pulse densities and scan-angle ranges. Our analysis identified three types of undetected voxels (Figure 3). First, we describe the reconstruction of pulse trajectories and the determination of different undetected voxels with ray tracing. We then document how different pulse densities and scan-angle ranges were simulated in section 2.4.

2.3.1 Reconstruction of pulse trajectories

We considered pulse trajectories as line segments with a starting point and an ending point. The location of the ending point was determined by the coordinates of a lidar return. To denote the starting point, we used the aircraft location at the time a return was recorded. For each recorded return, we determined the aircraft's location in latitude (Y), longitude (X), and elevation (Z) using linear interpolation of the 100 Hz GPS trajectory. After determining starting points of pulse

trajectories, we identified multiple returns associated with the same pulse using the recorded return number and the GPS time.

2.3.2 Voxel traversal

We calculated searching distances of the pulse trajectories within each voxel to identify different types of undetected voxels. Before calculating the searching distances, we determined the intersection points of each pulse trajectory with each voxel based on Eq. (2 – 4). First, we assessed whether the pulse was parallel to any plane of a voxel using

$$\vec{u} \cdot \overrightarrow{np} \neq 0, \tag{2}$$

where $\vec{u}$ represents the direction vector of a pulse trajectory, and $\overrightarrow{np}$ represents the normal vector of a plane coinciding with one of the six voxel surfaces. When the dot product of the two vectors was equal to 0, the pulse was parallel to the plane of the voxel and could not intersect that plane.

When the pulse was not parallel to a voxel plane, a line (not a line segment) sharing the same direction as the pulse trajectory intersects the infinite plane that coincides with the voxel plane. The intersection point between the line and the infinite plane was denoted by P. Solving for P requires the distance from the aircraft location, $u0$, to P, denoted using the scalar t. We solved for P and t using Eq. (3 – 4):

$$P = u0 + t \cdot \vec{u}, \tag{3}$$

$$(P - P0) \cdot \overrightarrow{np} = 0, \tag{4}$$

where $P0$ represents a random point on the plane.

After determining all intersection points based on the line and the infinite planes of a voxel, we excluded intersection points outside the voxel. Each voxel had at most two intersection points. We denominated the distances from the aircraft location to the intersection points D_{min} and D_{max}

according to the relative quantity of the distances, where D_{min} represented the distance from the starting point of the pulse trajectory to the entry point into the voxel, and D_{max} represented the distance to the departure point. The distance from the aircraft location to the lidar return point was D. If, for a given voxel, $D < D_{min}$ or $D > D_{max}$, the lidar return was generated in a different voxel.

The searched distance of a pulse trajectory concerning a given voxel was calculated under four scenarios (Figure 3A). In scenario #1 (Figure 3A: c, d, g, h), there were no intersection points for a given voxel, meaning that the searched distance of pulses inside the voxel was 0 because the laser was not fired in the direction of the voxel. In scenario #2 (Figure 3A: f, i), $D < D_{min}$. Here the searched distance within the voxel was 0 because the lidar return was triggered in a voxel closer to the sensor along the beam path. Scenario #3 (Figure 3A: e) illustrated a searched voxel where $D_{min} < D < D_{max}$. Here the searched distance was $D - D_{min}$ and a lidar return was generated inside the voxel. Lastly, in scenario #4 (Figure 3A: a, b), $D > D_{max}$, representing a voxel searched without producing a lidar return. The searched distance was $D_{max} - D_{min}$. The total distance searched for a given voxel was the sum of the searched distances produced by all pulse trajectories within the voxel.

When a voxel could have been traversed by a pulse, but it was not due to interception by other material along the beam path, this voxel was an occluded voxel. Voxels could be partially occluded or completely occluded. A voxel was partially occluded when non-occluded pulses also traversed it. A voxel was completely occluded when it was never traversed by a pulse, despite individual pulses being fired in the direction of the voxel.

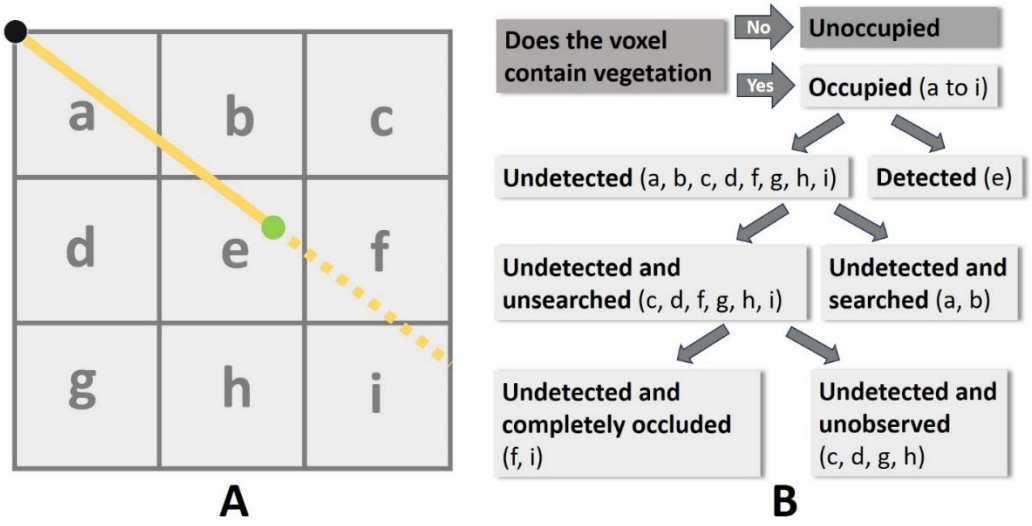

Figure 3. Voxel traversal and voxel type determination. (A) Illustration of voxel traversal in a 2-D view featuring nine voxels and a laser pulse generating a return. Suppose all the squares represent occupied voxels. The solid yellow line segment represents a pulse trajectory. The green dot represents a lidar return. The black dot is the starting point of the pulse trajectory. Letters a – i are labels for the voxels. (B) Relationships among the voxels depicted in (A).

2.4 Quantifying sampling completeness under simulated conditions

We quantified sampling completeness and proportions of three types of undetected voxels (Figure 3B; undetected and searched voxels, undetected and unobserved voxels, and undetected and completely occluded voxels) under simulated pulse densities and scan-angle ranges. Sampling completeness was quantified using the proportion of occupied voxels that were detected. The proportions of each type of undetected voxel were the ratios of those voxels relative to the total number of occupied voxels. Sampling completeness was quantified in both a 1 ha plot and four 100 m^2 plots, while proportions of different types of undetected voxels were quantified in the 100 m^2 plots (Figure 1C, Table 1). Note that for the 100 m^2 plots, only returns within each plot were considered. The undetected voxels were only studied in the 100 m^2 plots because the three types

of undetected voxels need to be determined by tracing pulse trajectories based on this high-resolution dataset at each pulse density and scan-angle range, which was computationally demanding for the 1 ha plot. The mean point density in the 1 ha plot was 3,354 points / m^2. The mean point density in each of the 100 m^2 plots was 3,870 points / m^2 (plot #1), 3,881 points / m^2 (plot #2), 3,828 points / m^2 (plot #3), and 2,953 points / m^2 (plot #4), respectively.

Table 1. Stem density and DBH within each plot used in the study.

Plot	**1 ha**	**100 m^2**			
		#1	#2	#3	#4
Stems (number / m^2)	0.3	0.2	0.5	0.03	0.2
Mean DBH (cm)	5.2	9.3	2.4	47.7	9.6
Maximum DBH (cm)	134.2	60.0	37.0	61.5	73.0
Minimum DBH (cm)	1.0	1.1	1.0	39.4	1.0

To quantify sampling completeness, we simulated different conditions by changing pulse density and scan-angle range. We considered pulse densities of 1 pulse / m^2, 10 pulses / m^2, 50 pulses / m^2, 100 pulses / m^2, 200 pulses / m^2, 300 pulses / m^2, 400 pulses / m^2, 500 pulses / m^2, 1,000 pulses / m^2 and 1,500 pulses / m^2. The nominal scan-angle range in our data was ± 60 degrees. We therefore considered scan-angle ranges of ± 5 degrees to ± 60 degrees in increments of ± 5 degrees (± 5 degrees, ± 10 degrees, ± 15 degrees, ± 20 degrees, ± 25 degrees, ± 30 degrees, ± 35 degrees, ± 40 degrees, ± 45 degrees, ± 50 degrees, ± 55 degrees, ± 60 degrees). For example, a scan-angle range of ± 5 means that the observations were acquired within a scan-angle range of -5 to 5 degrees; a scan-angle range of ± 30 means that the observations were acquired within a scan-angle range of -30 to 30 degrees. For each combination of pulse density and scan-angle range,

we excluded returns outside the specific scan-angle range, randomly sampled pulses from drone lidar, identified voxel types, and calculated proportions of different types of voxels. We repeated this process 10 times for each combination of pulse density and scan-angle range. The proportions were the arithmetic mean over these 10 simulations. Each combination of pulse density and scan-angle range was generated within tiles to reduce computation time, and results from tiles were then aggregated to derive results. Each tile in the 1 ha plot was 50 m^2, and each tile in a 100 m^2 plot was 4 m^2. Note that in the simulations based on tiles, the number of pulses under a simulated scan-angle range might be smaller than the pulse density to be simulated. Thus, there were missing simulated combinations for certain scan-angle ranges and pulse densities.

Although our flight plan was designed to minimize sampling variation from different observation angles, the observation angle may have an impact on sampling completeness. Therefore, we sampled combinations of four azimuth-angle ranges crossed by pulse density. The azimuth angle of each pulse was defined as the angle from 0 degrees to the projected pulse trajectory on the horizontal plane. We considered four azimuth-angle ranges: 0 – 90 degrees, 90 – 180 degrees, 180 – 270 degrees, and 270 – 360 degrees.

To gain a deeper understanding of the sampling capability of the high-density drone lidar, we investigated voxels at different heights by quantifying the different types of voxels throughout the canopy height profile. We obtained the ground elevation beneath each voxel using a digital terrain model (DTM) generated from ground returns. The height aboveground for each voxel was calculated by subtracting the ground elevation from the voxel elevation. We classified voxels based on their heights aboveground. Voxel heights aboveground used in this study ranged from 0 to 46 m, with increments of 0.5 m (e.g., 0 refers to the 0 – 0.5 m height class, 0.5 refers to the 0.5 – 1 m height class, and so forth). For each height increment, we quantified proportions of detected

and different undetected voxels in the 100 m^2 plots under each combination of simulated pulse density and scan-angle range.

3. Results

Results from all four 100 m^2 plots were broadly consistent, so we report results in the main text from plot #1. Summaries for the remaining plots are in Appendix 1.

3.1 Sampling completeness under different pulse densities and scan-angle ranges

Sampling completeness was more sensitive to pulse density than to scan-angle range (Figure 4). Although a strong relationship existed between sampling completeness and scan-angle range (Figure 4B), decoupling scan-angle range from pulse density revealed that most of the variation in sampling completeness was driven by pulse density (Figure 4A). For example, even with a scan-angle range as large as ± 60 degrees, a pulse density smaller than 100 pulses / m^2 could not achieve sampling completeness > 30% (Figure 4A).

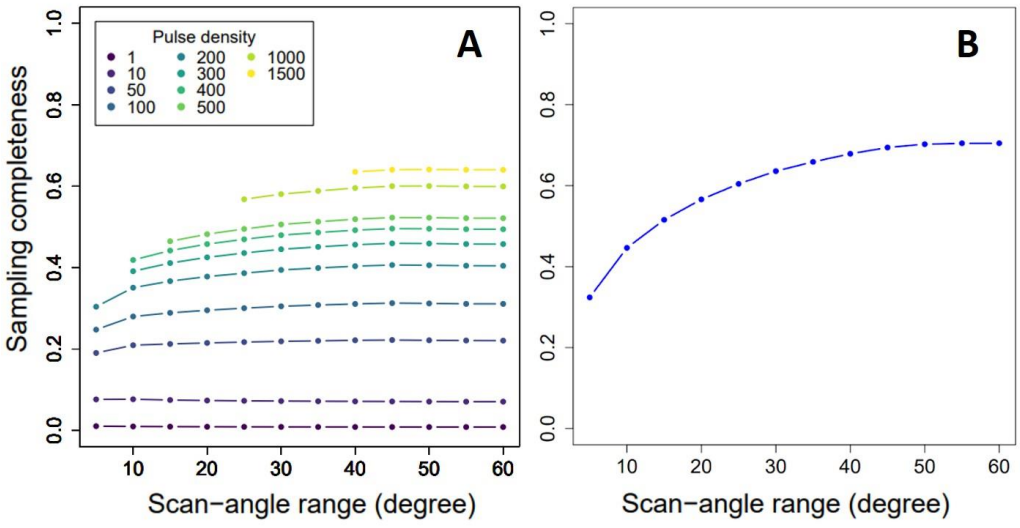

Figure 4. Sampling completeness (the proportion of occupied voxels that were detected) as a function of pulse density and scan-angle range (plot #1). (A) When scan-angle range was

decoupled from pulse density, sampling completeness was more strongly associated with pulse density than with scan-angle range. (B) Sampling completeness when scan-angle range was not decoupled from pulse density. Missing data points in (A) are associated with small sample sizes at certain combinations of scan-angle range and pulse density.

3.2 Undetected voxels under different pulse densities and scan-angle ranges

Combining data from drone lidar and TLS, we identified 12,823 occupied voxels in the 100 m^2 study area (plot #1). Before subsampling to limit pulse density and scan-angle range, the drone lidar searched 12,577 of the occupied voxels (98.1%) and detected 10,486 of the occupied voxels (81.8%). 2,091 of the searched voxels (16.6%) remained undetected. There were no undetected and unobserved voxels in the original data, meaning that all the undetected and unsearched voxels were unsearched due to occlusion, and are therefore regarded as undetected and completely occluded voxels.

When the pulse density and the scan-angle range were at their maximum subsampled value (1,500 pulses / m^2, ± 60 degrees), 3,065 (23.9%), 10 (0.1%), and 465 (3.6%) undetected voxels were identified as undetected and searched, undetected and unobserved, and undetected and completely occluded, respectively (Figure 5). However, when we simulated smaller pulse densities and narrower scan-angle ranges, proportions of different undetected voxels varied substantially (Figure 5, 6). For example, with a scan-angle range of ± 10 degrees and a pulse density of 1 pulse / m^2, the proportions of undetected and searched, undetected and unobserved, and undetected and completely occluded voxels were 8.7%, 76.7% and 13.7%, respectively (Figure 5). At 300 pulses / m^2 with the same scan-angle range, these values changed to 33.6%, 4.4% and 20.3%. Holding the pulse density at 300 pulses / m^2 and increasing the scan-angle range to ± 60 degrees resulted in values of 40.9%, 0.9% and 9.0%, respectively (Figure 5).

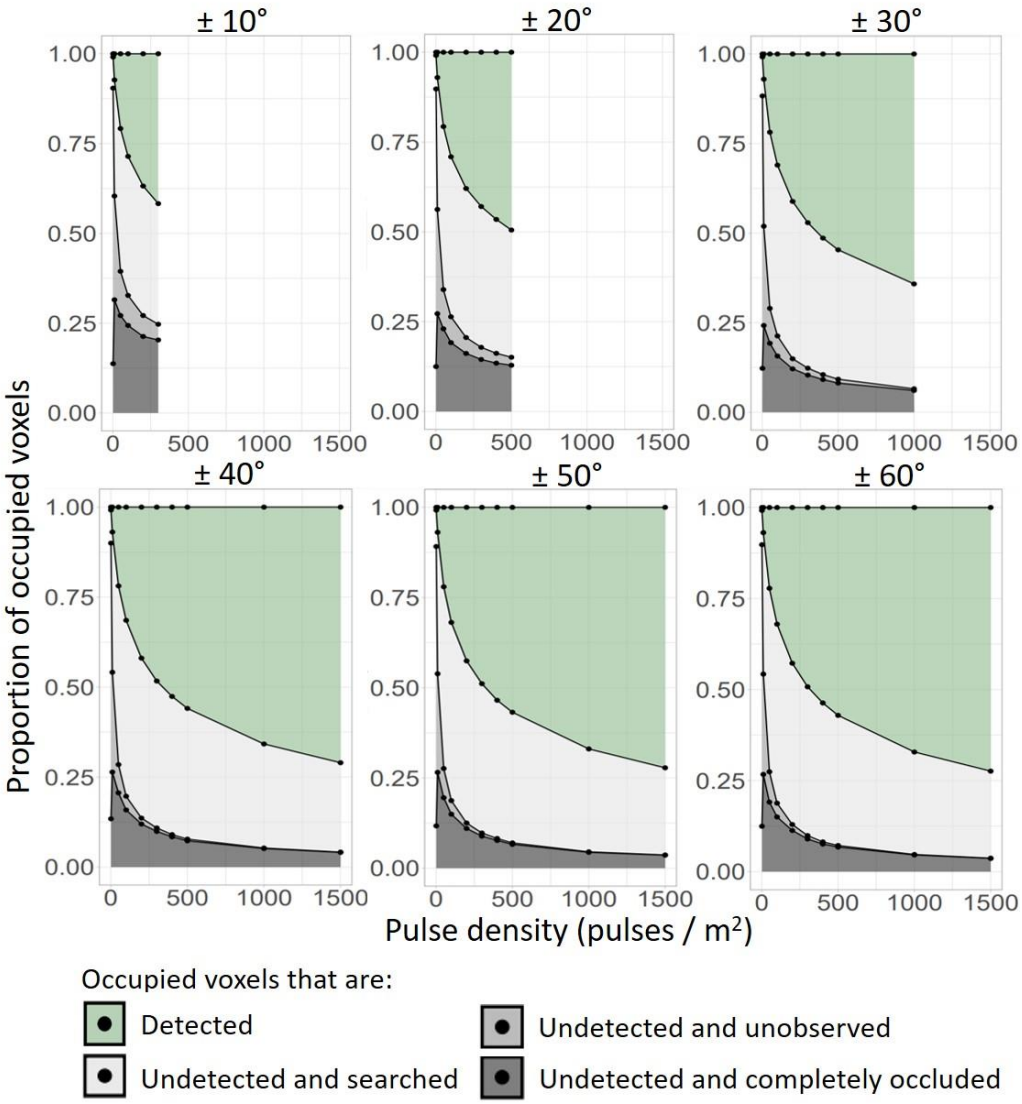

Figure 5. Proportions of occupied voxels that are detected and undetected as a function of pulse density and scan-angle range (plot #1). On each of the six panels, from left to right, the black dots represent pulse densities of 1, 10, 50, 100, 200, 300, 400, 500, 1,000, 1,500 pulses / m^2. Only 6 levels of scan-angle range (± 10 degrees, ± 20 degrees, ± 30 degrees, ± 40 degrees, ± 50 degrees, ± 60 degrees) are shown here because Figure 4 shows limited impact of scan-angle range after decoupling its impact from pulse density. Missing data points are associated with

small sample sizes at certain combinations of scan-angle range and pulse density. Proportions in the figure are also in Table S1 – S4.

The types of undetected voxels depended strongly on pulse density and weakly on scan-angle range (Figure 5, 6). Increasing pulse density or scan-angle range always reduced the proportion of undetected and unsearched and undetected and unobserved voxels (Figure 6A, 6C). However, this was not always the case for undetected and searched voxels, and undetected and completely occluded voxels: whether the numbers of these two types of undetected voxels decreased or increased depended on the pulse density and the scan-angle range. As the pulse density increased, the numbers of undetected searched and undetected, completely occluded voxels first increased and then decreased. For example, the proportion of undetected and searched voxels increased when the pulse density increased from 1 to 50 pulses / m^2 (Figure 6B), as did undetected and completely occluded voxels when the pulse density increased from 1 to 10 pulses / m^2 (Figure 6D). When the scan-angle range increased, the proportion of undetected and searched voxels increased (Figure 6B), while the proportions of the other three types of voxels decreased (Figure 6A, 6C, 6D). For all three types of undetected voxels, when the pulse density was as low as 1 pulse / m^2, the scan-angle range had little impact.

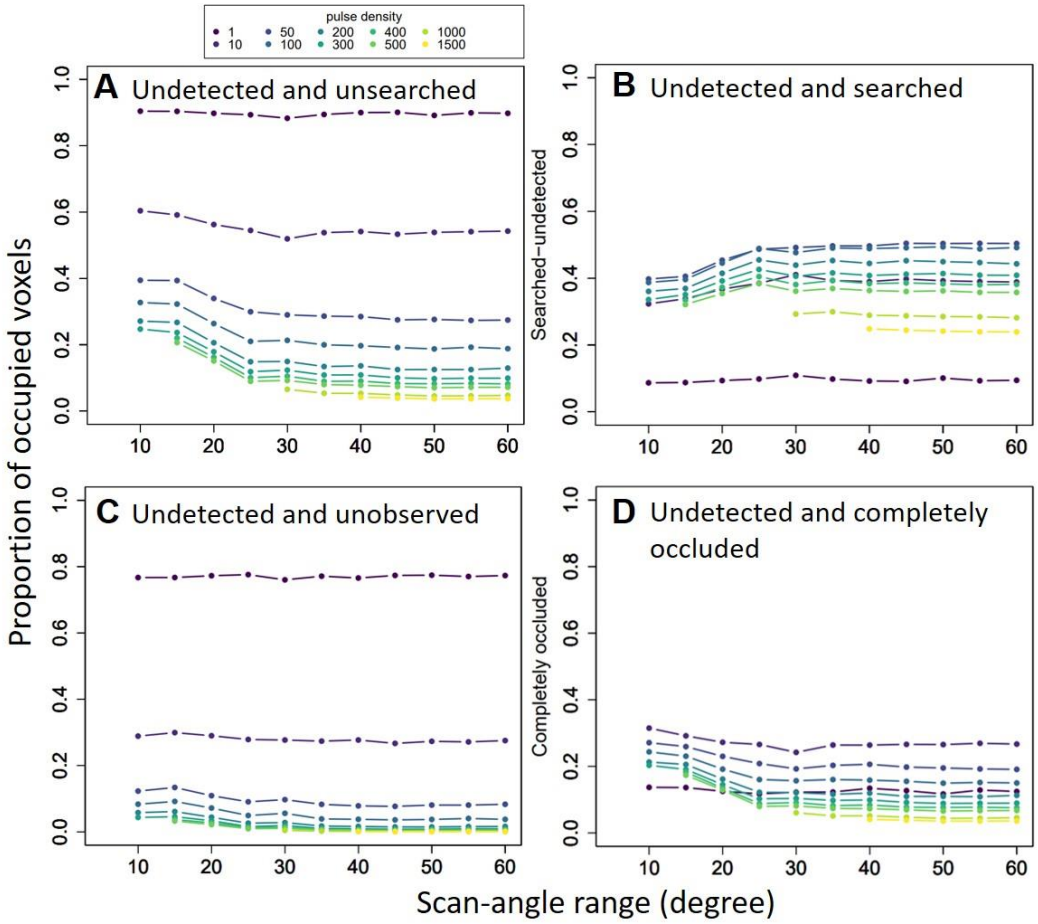

Figure 6. Proportions of different types of undetected voxels under different pulse densities and scan-angle ranges (plot #1). (A) Undetected and unsearched voxels. (B) Undetected and searched voxels. (C) Undetected and unobserved voxels. (D) Undetected and completely occluded voxels. Missing data points in each panel are associated with small sample sizes at some combinations of scan-angle range and pulse density. The number of undetected and unsearched voxels (A) is equal to the number of undetected and unobserved voxels (C) plus the number of undetected and completely occluded voxels (D).

3.3 Vertical variability of proportions of different types of voxels

High-density drone lidar detected voxels throughout the canopy height profile. There was a greater likelihood of detection near the top of the canopy (Figure 7, 8). For example, at 30 – 30.5 m aboveground, 91.3% of occupied voxels were detected when the pulse density was 1,000 pulses / m^2 and the scan-angle range was ± 60 degrees. These percentages decreased to 57.7%, 52.4%, and 29.9% at 20 – 20.5 m, 11 – 11.5 m, and 3 – 3.5 m aboveground, respectively (Figure 7). In general, almost no voxels were undetected and completely occluded near the top of the canopy. Both types of undetected and unsearched voxels (i.e., undetected and unobserved voxels, and undetected and completely occluded voxels) were more common at lower heights and at narrower scan-angle ranges. For example, in the upper canopy (30 – 30.5 m in Figure 7), there were no undetected and completely occluded voxels and all voxels were searched when the scan-angle range exceeded ± 20 degrees and pulse density was greater than 100 pulses / m^2. At 10 – 11.5 m aboveground, some voxels were consistently occluded, regardless of the scan-angle range and the pulse density (Figure 7, 8).

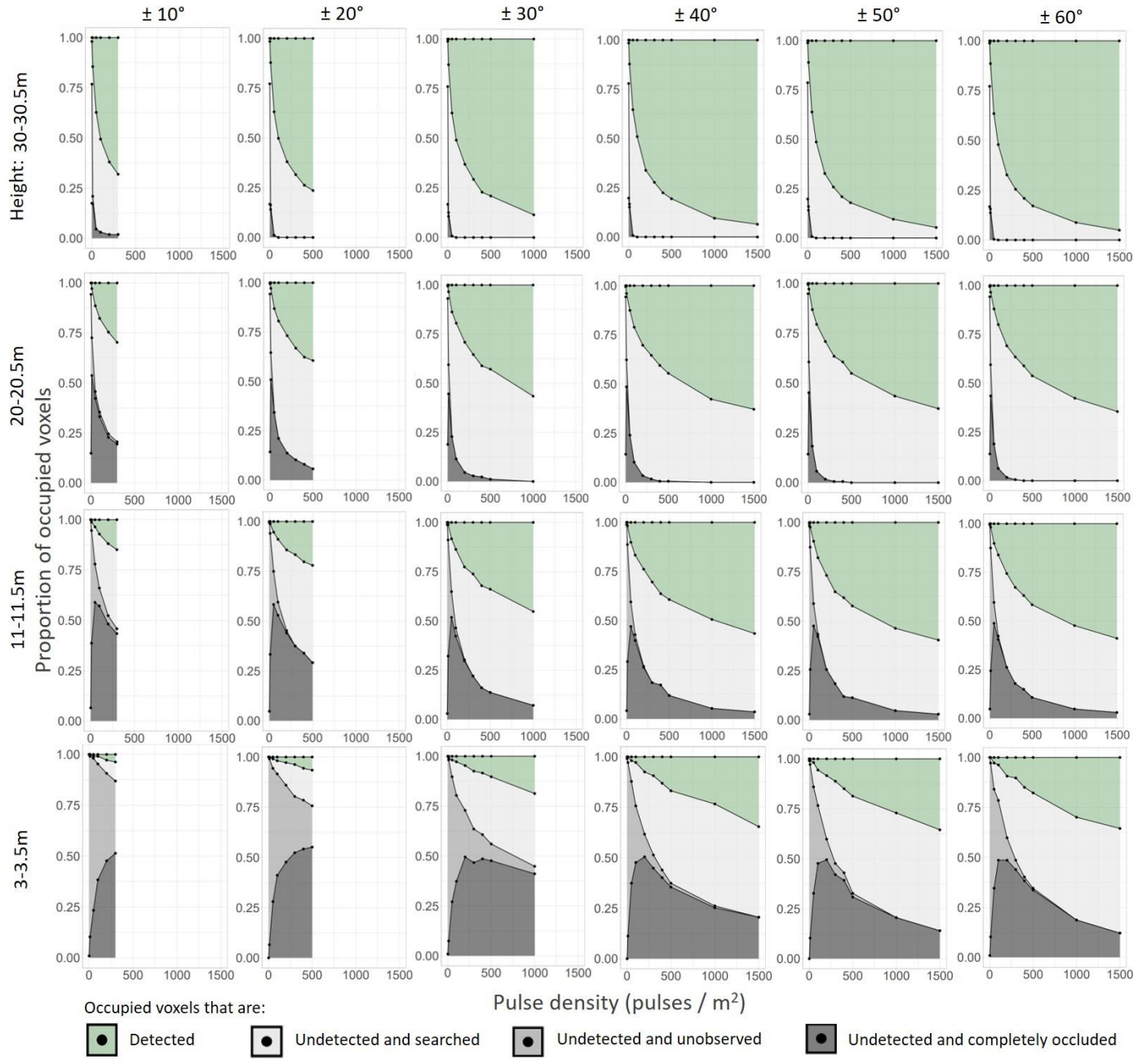

Figure 7. Proportions of occupied voxels that are detected and undetected as a function of pulse density and scan-angle range at multiple heights aboveground (plot #1). Only 6 levels of scan-angle range (± 10 degrees, ± 20 degrees, ± 30 degrees, ± 40 degrees, ± 50 degrees, ± 60 degrees) are shown here because Figure 4 shows limited impact of scan-angle range after decoupling its impact from pulse density. Missing data points are associated with small sample sizes at certain

combinations of scan-angle range and pulse density. The number of occupied voxels at each height (i.e., the denominator for calculating proportions of different undetected voxels at each height) is shown in Figure S15.

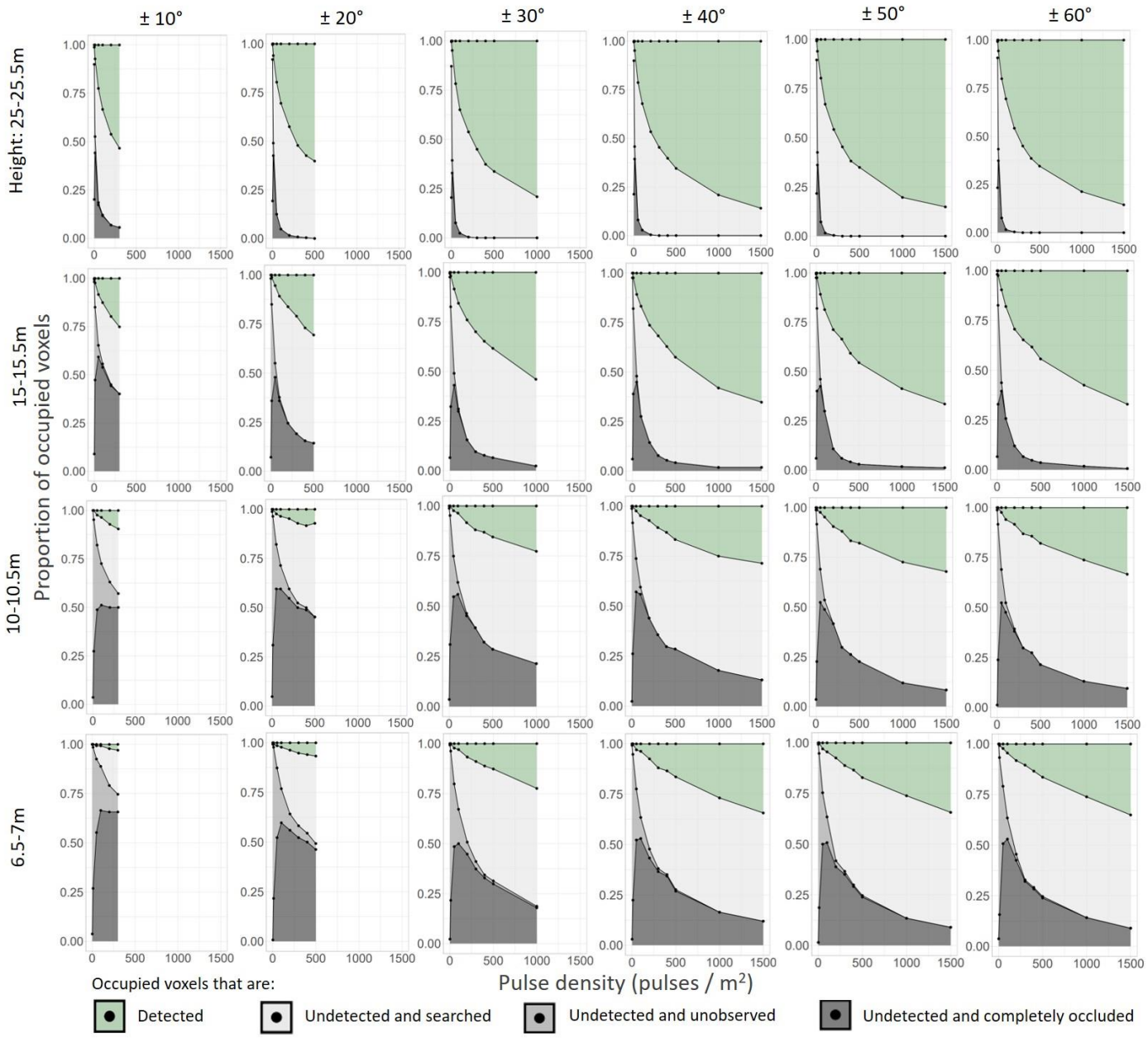

Figure 8. Proportions of occupied voxels that are detected and undetected as a function of pulse density and scan-angle range at multiple heights aboveground (plot #1). Only 6 levels of scan-

angle range (± 10 degrees, ± 20 degrees, ± 30 degrees, ± 40 degrees, ± 50 degrees, ± 60 degrees) are shown here because Figure 4 shows limited impact of scan-angle range after decoupling its impact from pulse density. Missing data points are associated with small sample sizes at certain combinations of scan-angle range and pulse density. The number of occupied voxels at each height (i.e., the denominator for calculating proportions of different undetected voxels at each height) is shown in Figure S15.

At different heights, the proportion of undetected voxels varied with pulse densities and scan-angle ranges differently (Figure 7). For example, undetected and unobserved voxels decreased as the pulse density increased at both lower and higher heights. However, undetected and searched voxels increased with pulse density at lower heights (e.g., scan-angle range ± 20 degrees, heights 3 – 3.5 m, in Figure 7; Figure 9) and decreased with pulse density at higher heights (e.g., scan-angle range ± 20 degrees, heights 30 – 30.5 m in Figure 7; Figure 9). At lower heights (Figure 7: 3 – 3.5 m, 11 – 11.5 m), undetected and completely occluded voxels first increased then decreased as the pulse density increased at most scan-angle ranges, while at higher heights they decreased with increasing pulse density (Figure 10).

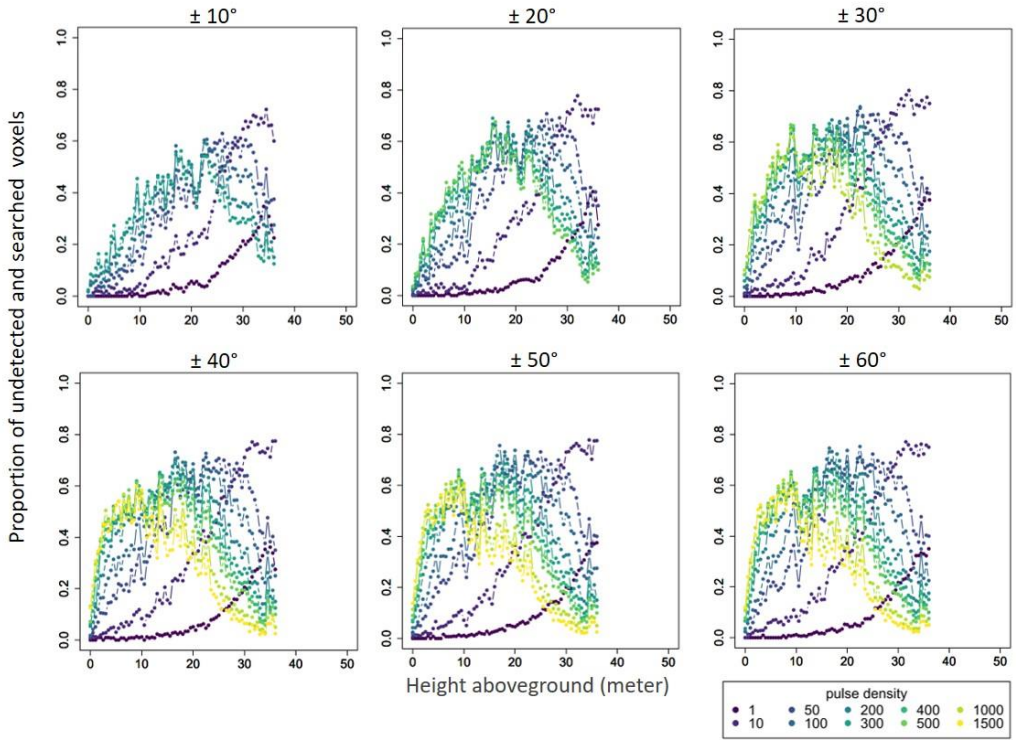

Figure 9. The proportion of undetected and searched voxels at different heights as a function of pulse density and scan-angle range in the 100 m^2 plot (plot #1). Only 6 levels of scan-angle range (± 10 degrees, ± 20 degrees, ± 30 degrees, ± 40 degrees, ± 50 degrees, ± 60 degrees) are shown here because Figure 4 shows limited impact of scan-angle range after decoupling its impact from pulse density. Missing data points are associated with small sample sizes at certain combinations of scan-angle range and pulse density.

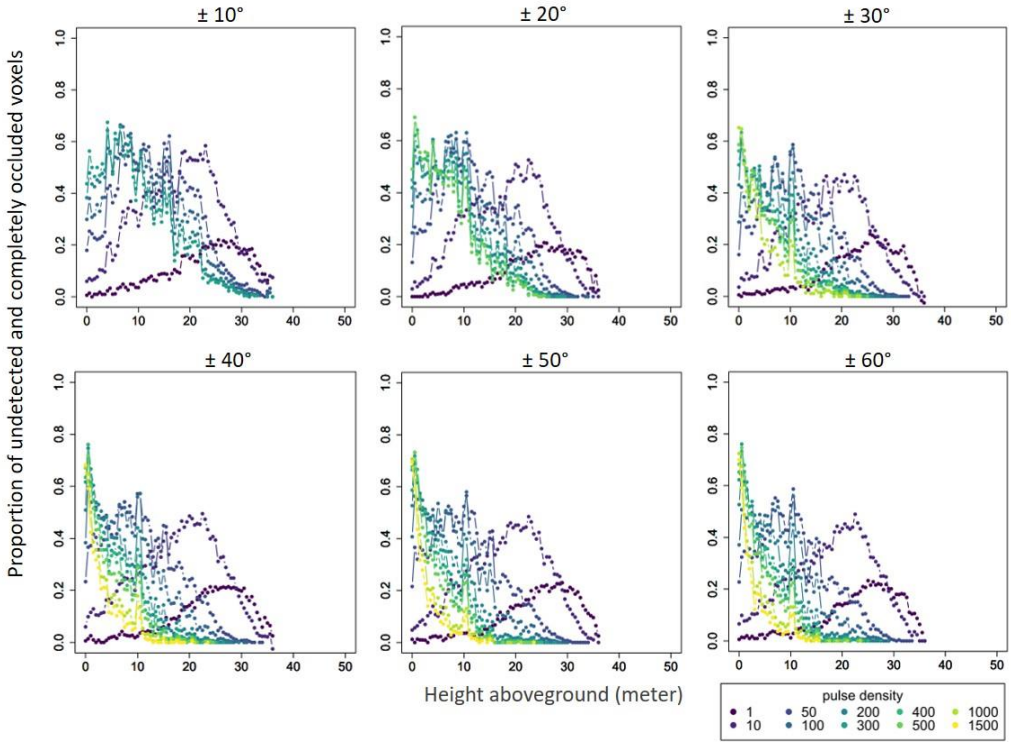

Figure 10. The proportion of undetected and completely occluded voxels at different heights as a function of pulse density and scan-angle range in the 100 m^2 plot (plot #1). Only 6 levels of scan-angle range (± 10 degrees, ± 20 degrees, ± 30 degrees, ± 40 degrees, ± 50 degrees, ± 60 degrees) are shown here because Figure 4 shows limited impact of scan-angle range after decoupling its impact from pulse density. Missing data points are associated with small sample sizes at some combinations of scan-angle range and pulse density.

The types of undetected voxels that are mainly responsible for unsampled forest structure changed with pulse density and height aboveground. Closer to the ground (3 – 3.5 m and 11 – 11.5 m in Figure 7), undetected voxels were mostly completely occluded. As pulse density increased, undetected voxels were more likely to have been searched, but undetected. For example, at 11 – 11.5 m aboveground, when the pulse density was 100 pulses / m^2 and the scan-angle range was ± 10 degrees, 66% of the occupied voxels were undetected and unsearched voxels (8.9% were

undetected and unobserved voxels and 57.1% were undetected and completely occluded voxels), 26.8% were undetected and searched voxels, and the detected voxels were 7.2%. At the same height, when the pulse density was 1,500 pulses / m^2, and the scan-angle range was ± 60 degrees, the proportion of undetected and searched voxels increased to 38.1%. Closer to the canopy (20 – 20.5 m and 30 – 30.5 m in Figure 7), the proportion of undetected and searched voxels was greater than that of undetected and completely occluded voxels for most of the pulse densities examined. There were undetected and searched voxels even at a high pulse density of 1,500 pulses / m^2 (Figure 7).

4. Discussion

4.1 Sampling completeness under different pulse densities and scan-angle ranges

Our study shows that scan-angle range had a limited impact on sampling completeness after it was decoupled from pulse density (Figure 4). We quantified the impact of pulse density and scan-angle range on sampling completeness and found that sampling completeness is more sensitive to pulse density than to scan-angle range. Increasing the pulse density increased the percentage of occupied voxels that were detected among all pulse densities examined, but increasing the scan-angle range did not necessarily increase sampling completeness. Thus, pulse density is the driver of sampling completeness in low-altitude lidar data, no matter how large the scan-angle range is.

Although scan-angle range was less important than pulse density to sampling completeness, some voxels were more likely to be observed at wide scan-angle ranges, including voxels occupied by vertical stems (Figure S1 – S3). This finding is consistent with previous work which shows that a wide scan-angle range or multiple view angles are important to generate stem returns (Brede et al., 2017; Dayal et al., 2022; Kellner et al., 2019; Terryn et al., 2022).

4.2 Undetected voxels under different pulse densities and scan-angle ranges

We observed that undetected voxels exhibited distinct covariation patterns with pulse density and scan-angle range. Undetected and searched voxels or undetected and completely occluded voxels did not necessarily decrease with greater pulse densities or scan-angle ranges, whereas undetected and unobserved voxels consistently decreased as the pulse density increased. Whether the former two types of undetected voxels decrease or increase with greater pulse densities depended on the specific pulse density and scan-angle range. As the pulse density increased, voxels that were undetected and searched or undetected and completely occluded first increased and then decreased (Figure 5, 6).

This study demonstrates that the undetected and searched voxels were the most common type of undetected voxels under the investigated voxel size (0.5 m), even under the largest possible pulse density and scan-angle range, followed by undetected and completely occluded voxels, and undetected and unobserved voxels (Figure 5, when the scan-angle range is ± 60 degrees). The existence of undetected and searched voxels underscores that space searched by pulses in the absence of a return is not necessarily unoccupied. The proportion of undetected and searched voxels was negatively related to pulse density (Figure 5, 6B). This was probably caused by insufficient searching distance within the voxel, although it could also be linked to voxel size, the number of pulses, and the distribution of vegetation in the voxel. The existence of such voxels could also depend on the amount of vegetation in comparison to other factors (i.e., footprint size, and laser power). If there is too little vegetation inside the voxel, the reflected pulse might be insufficient to trigger a return, especially when footprint size is large relative to the amount of vegetation in the voxel.

A majority of undetected and searched voxels had a large proportion of occluded pulses (Figure S16). When the pulse density was 1500 pulses / m^2 and the scan-angle range was ± 60 degrees, most of the undetected and searched voxels were occluded by more than half the pulses. The number of undetected and searched voxels with pulses that were occluded > 50% of the time increased with pulse density and scan-angle range.

Azimuth angle range had less impact on detected voxels than undetected voxels (Figure S7 – S10). When the pulse density was < 100 pulses / m^2, the proportions of detected voxels from the four azimuth-angle ranges were similar. Variation in sampling completeness from different azimuth-angle ranges was greater at large pulse densities. This probably reflects local differences in forest structure within 100 m^2 plots.

Pulses outside a plot may have influenced our results, but we believe the impact is small. Because we tracked all pulse trajectories associated with returns inside the plot, pulses outside the plot can affect the proportions of undetected and unsearched voxels, but not the proportions of detected voxels. By tracing additional pulses outside the plot, some undetected and unobserved voxels may be reclassified as undetected and searched or undetected and completely occluded voxels. Voxels that are undetected and completely occluded may remain the same or be reclassified as undetected and searched voxels in this scenario. Because the proportion of undetected and unsearched voxels was small (Figure 5, especially when the pulse density was greater than 1000 pulses / m^2), pulses outside the plot would have limited impact on our results.

4.3 Vertical variability of proportions of different types of voxels

Our study demonstrates that, despite a reduction in sampling completeness as pulses penetrated deeper into the canopy (i.e., as the height aboveground decreased; Figure 7), drone lidar data with a wide scan-angle range was able to achieve sampling completeness > 50% close to

ground level (Figure S14). For example, when the pulse density was 1,000 pulses / m^2, approximately half of the occupied voxels at 5 – 5.5 m aboveground were detected, even with a scan-angle range of ± 30 degrees (Figure S14, when the scan-angle range is ± 30 degrees). When the pulse density was as high as 1,500 pulses / m^2 and the scan-angle range was ± 60 degrees, nearly 60% of the occupied voxels at 10 – 10.5 m aboveground were detected (Figure S14, when the scan-angle range is ± 60 degrees).

Nevertheless, undetected voxels persisted at both lower and higher heights, even when pulse density was large and scan-angle range was wide (Figure 7). For example, at lower heights, greater pulse densities eliminated undetected and unobserved voxels, but undetected and completely occluded voxels, and undetected and searched voxels remained. In the upper canopies, greater pulse densities eliminated undetected and completely occluded voxels, and undetected and unobserved voxels, but undetected and searched voxels persisted. The persistence of undetected voxels at lower heights was probably due to the scarcity of pulses at these heights. A similar challenge near the top of the canopy exists in TLS sampling, where previous studies have shown that even multiple TLS scans do not guarantee complete sampling of canopy volume or stem structure (Liang et al., 2016; Paynter et al., 2018).

4.4 Future work

Some of our findings are likely to depend on voxel size. For example, undetected and searched voxels may be more common among larger individual voxel sizes than smaller ones. A future investigation should consider voxels of different sizes, including sizes that approach the diameter of the laser footprint.

We anticipate that when the voxel size is smaller, especially when voxel size is close to the laser footprint size, there will be relatively fewer undetected and searched voxels, and relatively

more undetected and unsearched voxels. The proportion of detected voxels in this study was from a 1 ha area in an old-growth temperate mountain forest, and proportions of undetected voxels were quantified in 100 m^2 plots. Coincident drone lidar and TLS collected at different locations with different canopy densities can be used to test the generality of these findings.

Our approach to sub-setting lidar data used tiles overlaid on each plot. Generating samples within each tile independently may have an influence on our conclusions by preventing spatial heterogeneity in the density of returns.

5. Conclusions

High-resolution drone lidar can acquire detailed measurements of vertical and horizontal forest structure. Drone lidar searched 98.1% of voxels known to contain vegetation in our study area, and generated returns in 81.8% of these voxels. By decoupling the impact of pulse density and scan-angle range on the likelihood of generating a return, this study demonstrates that nearly complete sampling of forest structure is possible using high-density drone lidar in a temperate mountain forest. The ability to generate a return when vegetation was present was more sensitive to pulse density than to scan-angle range. At very large pulse densities (> 1,000 pulses / m^2), failure to generate a return was almost exclusively associated with searched voxels that contained vegetation, but did not trigger a return.

This study documents three ways that a return can fail to be generated in the presence of vegetation: (1) the voxel could be searched but no return was generated, for example, because the voxel was sparsely populated and mostly empty space, (2) the voxel could be unsearched because it was occluded, and (3) the voxel could be unsearched because no pulse was fired in the direction of the voxel. Our findings demonstrate that all types of undetected voxels exist, and the proportion of each type changes with pulse density and scan-angle range. The strength and form of the

relationships depend on canopy height, pulse density and scan-angle range. These findings provide an empirical assessment of sampling completeness using a combination of high-resolution drone lidar and coincident TLS data. Our findings demonstrate the value of ray tracing to questions of sampling completeness in drone lidar data.

Acknowledgments

This research was funded by the Institute at Brown for Environment and Society, Peggy and Henry D. Sharpe Jr., INTER-COST project LUC23023, and the National Aeronautics and Space Administration of the United States of America. We gratefully acknowledge the ForestGEO Annual Analytical Workshop program funded by the Smithsonian Institution. We thank Christoph Eck, Christoph Falleger, Benedikt Imbach, Carlo Zgraggen and the Center for Computation and Visualization at Brown University.

References

Amanatides, J., Woo, A., 1987. A fast voxel traversal algorithm for ray tracing. Presented at the Eurographics, pp. 3–10.

Anderson-Teixeira, K.J., Davies, S.J., Bennett, A.C., Gonzalez-Akre, E.B., Muller-Landau, H.C., Wright, S.J., Abu Salim, K., Almeyda Zambrano, A.M., Alonso, A., Baltzer, J.L., Basset, Y., Bourg, N.A., Broadbent, E.N., Brockelman, W.Y., Bunyavejchewin, S., Burslem, D.F.R.P., Butt, N., Cao, M., Cardenas, D., Chuyong, G.B., Clay, K., Cordell, S., Dattaraja, H.S., Deng, X., Detto, M., Du, X., Duque, A., Erikson, D.L., Ewango, C.E.N., Fischer, G.A., Fletcher, C., Foster, R.B., Giardina, C.P., Gilbert, G.S., Gunatilleke, N., Gunatilleke, S., Hao, Z., Hargrove, W.W., Hart, T.B., Hau, B.C.H., He, F., Hoffman, F.M., Howe, R.W., Hubbell, S.P., Inman-Narahari, F.M., Jansen, P.A., Jiang, M.,

Johnson, D.J., Kanzaki, M., Kassim, A.R., Kenfack, D., Kibet, S., Kinnaird, M.F., Korte, L., Kral, K., Kumar, J., Larson, A.J., Li, Y., Li, X., Liu, S., Lum, S.K.Y., Lutz, J.A., Ma, K., Maddalena, D.M., Makana, J.-R., Malhi, Y., Marthews, T., Mat Serudin, R., McMahon, S.M., McShea, W.J., Memiaghe, H.R., Mi, X., Mizuno, T., Morecroft, M., Myers, J.A., Novotny, V., de Oliveira, A.A., Ong, P.S., Orwig, D.A., Ostertag, R., den Ouden, J., Parker, G.G., Phillips, R.P., Sack, L., Sainge, M.N., Sang, W., Sri-Ngernyuang, K., Sukumar, R., Sun, I.-F., Sungpalee, W., Suresh, H.S., Tan, S., Thomas, S.C., Thomas, D.W., Thompson, J., Turner, B.L., Uriarte, M., Valencia, R., Vallejo, M.I., Vicentini, A., Vrška, T., Wang, Xihua, Wang, Xugao, Weiblen, G., Wolf, A., Xu, H., Yap, S., Zimmerman, J., 2015. CTFS-ForestGEO: a worldwide network monitoring forests in an era of global change. Glob Chang Biol 21, 528–549. https://doi.org/10.1111/gcb.12712

Barazzetti, L., Previtali, M., Cantini, L., Oteri, A.M., 2023. Digital Recording of Historical Defensive Structures in Mountainous Areas Using Drones: Considerations and Comparisons. Drones 7, 512. https://doi.org/10.3390/drones7080512

Bauwens, S., Bartholomeus, H., Calders, K., Lejeune, P., 2016. Forest Inventory with Terrestrial LiDAR: A Comparison of Static and Hand-Held Mobile Laser Scanning. Forests 7, 127. https://doi.org/10.3390/f7060127

Beer, C., Reichstein, M., Tomelleri, E., Ciais, P., Jung, M., Carvalhais, N., Rödenbeck, C., Arain, M.A., Baldocchi, D., Bonan, G.B., Bondeau, A., Cescatti, A., Lasslop, G., Lindroth, A., Lomas, M., Luyssaert, S., Margolis, H., Oleson, K.W., Roupsard, O., Veenendaal, E., Viovy, N., Williams, C., Woodward, F.I., Papale, D., 2010. Terrestrial

Gross Carbon Dioxide Uptake: Global Distribution and Covariation with Climate. Science 329, 834–838. https://doi.org/10.1126/science.1184984

Beland, M., Parker, G., Sparrow, B., Harding, D., Chasmer, L., Phinn, S., Antonarakis, A., Strahler, A., 2019. On promoting the use of lidar systems in forest ecosystem research. Forest Ecology and Management 450, 117484. https://doi.org/10.1016/j.foreco.2019.117484

Béland, M., Widlowski, J.-L., Fournier, R.A., 2014. A model for deriving voxel-level tree leaf area density estimates from ground-based LiDAR. Environmental Modelling & Software 51, 184–189. https://doi.org/10.1016/j.envsoft.2013.09.034

Béland, M., Widlowski, J.-L., Fournier, R.A., Côté, J.-F., Verstraete, M.M., 2011. Estimating leaf area distribution in savanna trees from terrestrial LiDAR measurements. Agricultural and Forest Meteorology 151, 1252–1266. https://doi.org/10.1016/j.agrformet.2011.05.004

Bienert, A., Queck, R., Schmidt, A., Bernhofer, C., Maas, H.-G., 2010. Voxel space analysis of terrestrial laser scans in forests for wind field modelling. International Archives of Photogrammetry.Remote Sensing and Spatial Information Sciences 38, 92–97.

Bornand, A., Rehush, N., Morsdorf, F., Thürig, E., Abegg, M., 2023. Individual tree volume estimation with terrestrial laser scanning: Evaluating reconstructive and allometric approaches. Agricultural and Forest Meteorology 341, 109654. https://doi.org/10.1016/j.agrformet.2023.109654

Brede, B., Bartholomeus, H.M., Barbier, N., Pimont, F., Vincent, G., Herold, M., 2022. Peering through the thicket: Effects of UAV LiDAR scanner settings and flight planning on

canopy volume discovery. International Journal of Applied Earth Observation and Geoinformation 114, 103056. https://doi.org/10.1016/j.jag.2022.103056

Brede, B., Lau, A., Bartholomeus, H.M., Kooistra, L., 2017. Comparing RIEGL RiCOPTER UAV LiDAR Derived Canopy Height and DBH with Terrestrial LiDAR. Sensors 17, 2371. https://doi.org/10.3390/s17102371

Calders, K., Adams, J., Armston, J., Bartholomeus, H., Bauwens, S., Bentley, L.P., Chave, J., Danson, F.M., Demol, M., Disney, M., Gaulton, R., Krishna Moorthy, S.M., Levick, S.R., Saarinen, N., Schaaf, C., Stovall, A., Terryn, L., Wilkes, P., Verbeeck, H., 2020. Terrestrial laser scanning in forest ecology: Expanding the horizon. Remote Sensing of Environment 251, 112102. https://doi.org/10.1016/j.rse.2020.112102

Calders, K., Armston, J., Newnham, G., Herold, M., Goodwin, N., 2014. Implications of sensor configuration and topography on vertical plant profiles derived from terrestrial LiDAR. Agricultural and Forest Meteorology 194, 104–117. https://doi.org/10.1016/j.agrformet.2014.03.022

Calders, K., Newnham, G., Burt, A., Murphy, S., Raumonen, P., Herold, M., Culvenor, D., Avitabile, V., Disney, M., Armston, J., Kaasalainen, M., 2015. Nondestructive estimates of above-ground biomass using terrestrial laser scanning. Methods in Ecology and Evolution 6, 198–208. https://doi.org/10.1111/2041-210X.12301

Chasmer, L., Hopkinson, C., Treitz, P., 2004. Assessing the three-dimensional frequency distribution of airborne and ground-based lidar data for red pine and mixed deciduous forest plots. Int Arch Photogramm Remote Sens Spat Inf Sci 36, W2.

Cifuentes, R., Van der Zande, D., Farifteh, J., Salas, C., Coppin, P., 2014. Effects of voxel size and sampling setup on the estimation of forest canopy gap fraction from terrestrial laser

scanning data. Agricultural and Forest Meteorology 194, 230–240. https://doi.org/10.1016/j.agrformet.2014.04.013

Committee on Earth Observation Satellites, 2021. Aboveground Woody Biomass Product Validation Good Practices Protocol.

Coops, N.C., Tompalski, P., Goodbody, T.R.H., Queinnec, M., Luther, J.E., Bolton, D.K., White, J.C., Wulder, M.A., van Lier, O.R., Hermosilla, T., 2021. Modelling lidar-derived estimates of forest attributes over space and time: A review of approaches and future trends. Remote Sensing of Environment 260, 112477. https://doi.org/10.1016/j.rse.2021.112477

Cushman, K.C., Armston, J., Dubayah, R., Duncanson, L., Hancock, S., Janík, D., Král, K., Krůček, M., Minor, D.M., Tang, H., Kellner, J.R., 2023. Impact of leaf phenology on estimates of aboveground biomass density in a deciduous broadleaf forest from simulated GEDI lidar. Environ. Res. Lett. 18, 065009. https://doi.org/10.1088/1748-9326/acd2ec

Dassot, M., Colin, A., Santenoise, P., Fournier, M., Constant, T., 2012. Terrestrial laser scanning for measuring the solid wood volume, including branches, of adult standing trees in the forest environment. Computers and Electronics in Agriculture 89, 86–93. https://doi.org/10.1016/j.compag.2012.08.005

Dayal, K.R., Durrieu, S., Lahssini, K., Alleaume, S., Bouvier, M., Monnet, J.-M., Renaud, J.-P., Revers, F., 2022. An investigation into lidar scan angle impacts on stand attribute predictions in different forest environments. ISPRS Journal of Photogrammetry and Remote Sensing 193, 314–338. https://doi.org/10.1016/j.isprsjprs.2022.08.013

Disney, M., Burt, A., Calders, K., Schaaf, C., Stovall, A., 2019. Innovations in Ground and Airborne Technologies as Reference and for Training and Validation: Terrestrial Laser

Scanning (TLS). Surv Geophys 40, 937–958. https://doi.org/10.1007/s10712-019-09527-x

Disney, M., Burt, A., Wilkes, P., Armston, J., Duncanson, L., 2020. New 3D measurements of large redwood trees for biomass and structure. Sci Rep 10, 16721. https://doi.org/10.1038/s41598-020-73733-6

Disney, M., Lewis, P., Saich, P., 2006. 3D modelling of forest canopy structure for remote sensing simulations in the optical and microwave domains. Remote Sensing of Environment 100, 114–132. https://doi.org/10.1016/j.rse.2005.10.003

Duncanson, L., Armston, J., Disney, M., Avitabile, V., Barbier, N., Calders, K., Carter, S., Chave, J., Herold, M., Crowther, T.W., Falkowski, M., Kellner, J.R., Labrière, N., Lucas, R., MacBean, N., McRoberts, R.E., Meyer, V., Næsset, E., Nickeson, J.E., Paul, K.I., Phillips, O.L., Réjou-Méchain, M., Román, M., Roxburgh, S., Saatchi, S., Schepaschenko, D., Scipal, K., Siqueira, P.R., Whitehurst, A., Williams, M., 2019. The Importance of Consistent Global Forest Aboveground Biomass Product Validation. Surv Geophys 40, 979–999. https://doi.org/10.1007/s10712-019-09538-8

FAO and UNEP, 2020. The State of the World's Forests 2020: Forests, biodiversity and people, The State of the World's Forests (SOFO). FAO and UNEP, Rome, Italy. https://doi.org/10.4060/ca8642en

Hyyppä, E., Kukko, A., Kaijaluoto, R., White, J.C., Wulder, M.A., Pyörälä, J., Liang, X., Yu, X., Wang, Y., Kaartinen, H., Virtanen, J.-P., Hyyppä, J., 2020. Accurate derivation of stem curve and volume using backpack mobile laser scanning. ISPRS Journal of Photogrammetry and Remote Sensing 161, 246–262. https://doi.org/10.1016/j.isprsjprs.2020.01.018

Jaakkola, A., Hyyppä, J., Kukko, A., Yu, X., Kaartinen, H., Lehtomäki, M., Lin, Y., 2010. A low-cost multi-sensoral mobile mapping system and its feasibility for tree measurements. ISPRS Journal of Photogrammetry and Remote Sensing, ISPRS Centenary Celebration Issue 65, 514–522. https://doi.org/10.1016/j.isprsjprs.2010.08.002

Janík, D., Král, K., Adam, D., Hort, L., Samonil, P., Unar, P., Vrska, T., McMahon, S., 2016. Tree spatial patterns of Fagus sylvatica expansion over 37years. Forest Ecology and Management 375, 134–145. https://doi.org/10.1016/j.foreco.2016.05.017

Kellner, J.R., Armston, J., Birrer, M., Cushman, K.C., Duncanson, L., Eck, C., Falleger, C., Imbach, B., Král, K., Krůček, M., 2019. New opportunities for forest remote sensing through ultra-high-density drone lidar. Surveys in Geophysics 40, 959–977.

Korpela, I., Hovi, A., Morsdorf, F., 2012. Understory trees in airborne LiDAR data — Selective mapping due to transmission losses and echo-triggering mechanisms. Remote Sensing of Environment 119, 92–104. https://doi.org/10.1016/j.rse.2011.12.011

Krůček, M., Král, K., Cushman, K.C., Missarov, A., Kellner, J.R., 2020. Supervised Segmentation of Ultra-High-Density Drone Lidar for Large-Area Mapping of Individual Trees. Remote Sensing 12, 3260. https://doi.org/10.3390/rs12193260

Kükenbrink, D., Schneider, F.D., Leiterer, R., Schaepman, M.E., Morsdorf, F., 2017. Quantification of hidden canopy volume of airborne laser scanning data using a voxel traversal algorithm. Remote Sensing of Environment 194, 424–436. https://doi.org/10.1016/j.rse.2016.10.023

LaRue, E.A., Wagner, F.W., Fei, S., Atkins, J.W., Fahey, R.T., Gough, C.M., Hardiman, B.S., 2020. Compatibility of Aerial and Terrestrial LiDAR for Quantifying Forest Structural Diversity. Remote Sensing 12, 1407. https://doi.org/10.3390/rs12091407

Li, W., Guo, Q., Tao, S., Su, Y., 2018. VBRT: A novel voxel-based radiative transfer model for heterogeneous three-dimensional forest scenes. Remote Sensing of Environment 206, 318–335. https://doi.org/10.1016/j.rse.2017.12.043

Li, Y., Guo, Q., Su, Y., Tao, S., Zhao, K., Xu, G., 2017. Retrieving the gap fraction, element clumping index, and leaf area index of individual trees using single-scan data from a terrestrial laser scanner. ISPRS JOURNAL OF PHOTOGRAMMETRY AND REMOTE SENSING 130, 308–316. https://doi.org/10.1016/j.isprsjprs.2017.06.006

Liang, X., Hyyppä, J., Kukko, A., Kaartinen, H., Jaakkola, A., Yu, X., 2014a. The Use of a Mobile Laser Scanning System for Mapping Large Forest Plots. IEEE Geoscience and Remote Sensing Letters 11, 1504–1508. https://doi.org/10.1109/LGRS.2013.2297418

Liang, X., Kankare, V., Hyyppä, J., Wang, Y., Kukko, A., Haggrén, H., Yu, X., Kaartinen, H., Jaakkola, A., Guan, F., Holopainen, M., Vastaranta, M., 2016. Terrestrial laser scanning in forest inventories. ISPRS JOURNAL OF PHOTOGRAMMETRY AND REMOTE SENSING 115, 63–77. https://doi.org/10.1016/j.isprsjprs.2016.01.006

Liang, X., Kukko, A., Kaartinen, H., Hyyppä, J., Yu, X., Jaakkola, A., Wang, Y., 2014b. Possibilities of a Personal Laser Scanning System for Forest Mapping and Ecosystem Services. Sensors 14, 1228–1248. https://doi.org/10.3390/s140101228

Liu, J., Skidmore, A., Wang, T., Zhu, X., Premier, J., Heurich, M., Beudert, B., Jones, S., 2019. Variation of leaf angle distribution quantified by terrestrial LiDAR in natural European beech forest. ISPRS JOURNAL OF PHOTOGRAMMETRY AND REMOTE SENSING 148, 208–220. https://doi.org/10.1016/j.isprsjprs.2019.01.005

Ma, L., Hurtt, G., Tang, H., Lamb, R., Lister, A., Chini, L., Dubayah, R., Armston, J., Campbell, E., Duncanson, L., Healey, S., O'Neil-Dunne, J., Ott, L., Poulter, B., Shen, Q., 2023.

Spatial heterogeneity of global forest aboveground carbon stocks and fluxes constrained by spaceborne lidar data and mechanistic modeling. Global Change Biology 29, 3378–3394. https://doi.org/10.1111/gcb.16682

Magney, T.S., Eitel, J.U.H., Griffin, K.L., Boelman, N.T., Greaves, H.E., Prager, C.M., Logan, B.A., Zheng, G., Ma, L., Fortin, E.A., Oliver, R.Y., Vierling, L.A., 2016. LiDAR canopy radiation model reveals patterns of photosynthetic partitioning in an Arctic shrub. Agricultural and Forest Meteorology 221, 78–93. https://doi.org/10.1016/j.agrformet.2016.02.007

Morsdorf, F., Frey, O., Koetz, B., Meier, E., 2007. Ray tracing for modeling of small footprint airborne laser scanning returns. International Archives of the Photogrammetry, Remote Sensing and Spatial Information Sciences 36, 249–299.

Morsdorf, F., Kötz, B., Meier, E., Itten, K.I., Allgöwer, B., 2006. Estimation of LAI and fractional cover from small footprint airborne laser scanning data based on gap fraction. Remote Sensing of Environment 104, 50–61.

Musselman, K.N., Margulis, S.A., Molotch, N.P., 2013. Estimation of solar direct beam transmittance of conifer canopies from airborne LiDAR. Remote Sensing of Environment 136, 402–415. https://doi.org/10.1016/j.rse.2013.05.021

Olsoy, P., Glenn, N., Clark, P., Derryberry, D., 2014. Aboveground total and green biomass of dryland shrub derived from terrestrial laser scanning. ISPRS JOURNAL OF PHOTOGRAMMETRY AND REMOTE SENSING 88, 166–173. https://doi.org/10.1016/j.isprsjprs.2013.12.006

Pan, Y., Birdsey, R.A., Phillips, O.L., Jackson, R.B., 2013. The Structure, Distribution, and Biomass of the World's Forests. Annual Review of Ecology, Evolution, and Systematics 44, 593–622. https://doi.org/10.1146/annurev-ecolsys-110512-135914

Paynter, I., Genest, D., Saenz, E., Peri, F., Li, Z., Strahler, A., Schaaf, C., 2018. Quality Assessment of Terrestrial Laser Scanner Ecosystem Observations Using Pulse Trajectories. IEEE Transactions on Geoscience and Remote Sensing 56, 6324–6333. https://doi.org/10.1109/TGRS.2018.2836947

Pueschel, P., Newnham, G., Rock, G., Udelhoven, T., Werner, W., Hill, J., 2013. The influence of scan mode and circle fitting on tree stem detection, stem diameter and volume extraction from terrestrial laser scans. ISPRS Journal of Photogrammetry and Remote Sensing 77, 44–56. https://doi.org/10.1016/j.isprsjprs.2012.12.001

Puliti, S., Dash, J.P., Watt, M.S., Breidenbach, J., Pearse, G.D., 2020. A comparison of UAV laser scanning, photogrammetry and airborne laser scanning for precision inventory of small-forest properties. Forestry: An International Journal of Forest Research 93, 150–162. https://doi.org/10.1093/forestry/cpz057

Qi, Y., Coops, N.C., Daniels, L.D., Butson, C.R., 2022. Comparing tree attributes derived from quantitative structure models based on drone and mobile laser scanning point clouds across varying canopy cover conditions. ISPRS Journal of Photogrammetry and Remote Sensing 192, 49–65. https://doi.org/10.1016/j.isprsjprs.2022.07.021

Resop, J.P., Lehmann, L., Hession, W.C., 2019. Drone Laser Scanning for Modeling Riverscape Topography and Vegetation: Comparison with Traditional Aerial Lidar. Drones 3, 35. https://doi.org/10.3390/drones3020035

Roşca, S., Suomalainen, J., Bartholomeus, H., Herold, M., 2018. Comparing terrestrial laser scanning and unmanned aerial vehicle structure from motion to assess top of canopy structure in tropical forests. Interface Focus 8, 20170038. https://doi.org/10.1098/rsfs.2017.0038

Ryding, J., Williams, E., Smith, M.J., Eichhorn, M.P., 2015. Assessing Handheld Mobile Laser Scanners for Forest Surveys. Remote Sensing 7, 1095–1111. https://doi.org/10.3390/rs70101095

Saarela, S., Wästlund, A., Holmström, E., Mensah, A.A., Holm, S., Nilsson, M., Fridman, J., Ståhl, G., 2020. Mapping aboveground biomass and its prediction uncertainty using LiDAR and field data, accounting for tree-level allometric and LiDAR model errors. For. Ecosyst. 7, 43. https://doi.org/10.1186/s40663-020-00245-0

Saatchi, S.S., Harris, N.L., Brown, S., Lefsky, M., Mitchard, E.T.A., Salas, W., Zutta, B.R., Buermann, W., Lewis, S.L., Hagen, S., Petrova, S., White, L., Silman, M., Morel, A., 2011. Benchmark map of forest carbon stocks in tropical regions across three continents. PNAS 108, 9899–9904. https://doi.org/10.1073/pnas.1019576108

Schneider, F.D., Kükenbrink, D., Schaepman, M.E., Schimel, D.S., Morsdorf, F., 2019. Quantifying 3D structure and occlusion in dense tropical and temperate forests using close-range LiDAR. Agricultural and Forest Meteorology 268, 249–257. https://doi.org/10.1016/j.agrformet.2019.01.033

Shui, W., Li, H., Zhang, Y., Jiang, C., Zhu, S., Wang, Q., Liu, Y., Zong, S., Huang, Y., Ma, M., 2022. Is an Unmanned Aerial Vehicle (UAV) Suitable for Extracting the Stand Parameters of Inaccessible Underground Forests of Karst Tiankeng? Remote Sensing 14, 4128. https://doi.org/10.3390/rs14174128

Smith, M.N., Stark, S.C., Taylor, T.C., Ferreira, M.L., de Oliveira, E., Restrepo-Coupe, N., Chen, S., Woodcock, T., dos Santos, D.B., Alves, L.F., Figueira, M., de Camargo, P.B., de Oliveira, R.C., Aragão, L.E.O.C., Falk, D.A., McMahon, S.M., Huxman, T.E., Saleska, S.R., 2019. Seasonal and drought-related changes in leaf area profiles depend on height and light environment in an Amazon forest. New Phytologist 222, 1284–1297. https://doi.org/10.1111/nph.15726

Stovall, A.E.L., Shugart, H.H., 2018. Improved Biomass Calibration and Validation With Terrestrial LiDAR: Implications for Future LiDAR and SAR Missions. IEEE Journal of Selected Topics in Applied Earth Observations and Remote Sensing 11, 3527–3537. https://doi.org/10.1109/JSTARS.2018.2803110

Stovall, A.E.L., Vorster, A.G., Anderson, R.S., Evangelista, P.H., Shugart, H.H., 2017. Non-destructive aboveground biomass estimation of coniferous trees using terrestrial LiDAR. Remote Sensing of Environment 200, 31–42. https://doi.org/10.1016/j.rse.2017.08.013

Strahler, A.H., Jupp, D.L.B., Woodcock, C.E., Schaaf, C.B., Yao, T., Zhao, F., Yang, X., Lovell, J., Culvenor, D., Newnham, G., Ni-Miester, W., Boykin-Morris, W., 2008. Retrieval of forest structural parameters using a ground-based lidar instrument (Echidna®). Canadian Journal of Remote Sensing 34, S426–S440. https://doi.org/10.5589/m08-046

Terryn, L., Calders, K., Bartholomeus, H., Bartolo, R.E., Brede, B., D'hont, B., Disney, M., Herold, M., Lau, A., Shenkin, A., Whiteside, T.G., Wilkes, P., Verbeeck, H., 2022. Quantifying tropical forest structure through terrestrial and UAV laser scanning fusion in Australian rainforests. Remote Sensing of Environment 271, 112912. https://doi.org/10.1016/j.rse.2022.112912

Trochta, J., Krůček, M., Vrška, T., Král, K., 2017. 3D Forest: An application for descriptions of three-dimensional forest structures using terrestrial LiDAR. PLoS One 12, e0176871. https://doi.org/10.1371/journal.pone.0176871

Van der Zande, D., Mereu, S., Nadezhdina, N., Cermak, J., Muys, B., Coppin, P., Manes, F., 2009. 3D upscaling of transpiration from leaf to tree using ground-based LiDAR: Application on a Mediterranean Holm oak (Quercus ilex L.) tree. Agricultural and Forest Meteorology 149, 1573–1583. https://doi.org/10.1016/j.agrformet.2009.04.010

Vincent, G., Antin, C., Laurans, M., Heurtebize, J., Durrieu, S., Lavalley, C., Dauzat, J., 2017. Mapping plant area index of tropical evergreen forest by airborne laser scanning. A cross-validation study using LAI2200 optical sensor. Remote Sensing of Environment 198, 254–266. https://doi.org/10.1016/j.rse.2017.05.034

Wang, Q., Pang, Y., Chen, D., Liang, X., Lu, J., 2021. Lidar biomass index: A novel solution for tree-level biomass estimation using 3D crown information. Forest Ecology and Management 499, 119542. https://doi.org/10.1016/j.foreco.2021.119542

Wilkes, P., Lau, A., Disney, M., Calders, K., Burt, A., Gonzalez de Tanago, J., Bartholomeus, H., Brede, B., Herold, M., 2017. Data acquisition considerations for Terrestrial Laser Scanning of forest plots. Remote Sensing of Environment 196, 140–153. https://doi.org/10.1016/j.rse.2017.04.030

Xie, D., Wang, X., Qi, J., Chen, Y., Mu, X., Zhang, W., Yan, G., 2018. Reconstruction of Single Tree with Leaves Based on Terrestrial LiDAR Point Cloud Data. Remote Sensing 10, 686. https://doi.org/10.3390/rs10050686

Xu, L., Saatchi, S.S., Shapiro, A., Meyer, V., Ferraz, A., Yang, Y., Bastin, J.-F., Banks, N., Boeckx, P., Verbeeck, H., Lewis, S.L., Muanza, E.T., Bongwele, E., Kayembe, F.,

Mbenza, D., Kalau, L., Mukendi, F., Ilunga, F., Ebuta, D., 2017. Spatial Distribution of Carbon Stored in Forests of the Democratic Republic of Congo. Sci Rep 7, 15030. https://doi.org/10.1038/s41598-017-15050-z

Yang, B., Fang, L., Li, J., 2013. Semi-automated extraction and delineation of 3D roads of street scene from mobile laser scanning point clouds. ISPRS Journal of Photogrammetry and Remote Sensing 79, 80–93. https://doi.org/10.1016/j.isprsjprs.2013.01.016

Yang, X., Strahler, A.H., Schaaf, C.B., Jupp, D.L.B., Yao, T., Zhao, F., Wang, Z., Culvenor, D.S., Newnham, G.J., Lovell, J.L., Dubayah, R.O., Woodcock, C.E., Ni-Meister, W., 2013. Three-dimensional forest reconstruction and structural parameter retrievals using a terrestrial full-waveform lidar instrument (Echidna®). Remote Sensing of Environment 135, 36–51. https://doi.org/10.1016/j.rse.2013.03.020

Zhang, K., Chen, S.-C., Whitman, D., Shyu, M.-L., Yan, J., Zhang, C., 2003. A progressive morphological filter for removing nonground measurements from airborne LIDAR data. IEEE Transactions on Geoscience and Remote Sensing 41, 872–882. https://doi.org/10.1109/TGRS.2003.810682

Zhao, K., Popescu, S., Nelson, R., 2009. Lidar remote sensing of forest biomass: A scale-invariant estimation approach using airborne lasers. Remote Sensing of Environment 113, 182–196. https://doi.org/10.1016/j.rse.2008.09.009

Zheng, G., Moskal, L.M., Kim, S.-H., 2013. Retrieval of Effective Leaf Area Index in Heterogeneous Forests With Terrestrial Laser Scanning. IEEE Transactions on Geoscience and Remote Sensing 51, 777–786. https://doi.org/10.1109/TGRS.2012.2205003

Zong, X., Wang, T., Skidmore, A.K., Heurich, M., 2021. The impact of voxel size, forest type, and understory cover on visibility estimation in forests using terrestrial laser scanning. GIScience & Remote Sensing 58, 323–339. https://doi.org/10.1080/15481603.2021.1873588

Supplementary materials

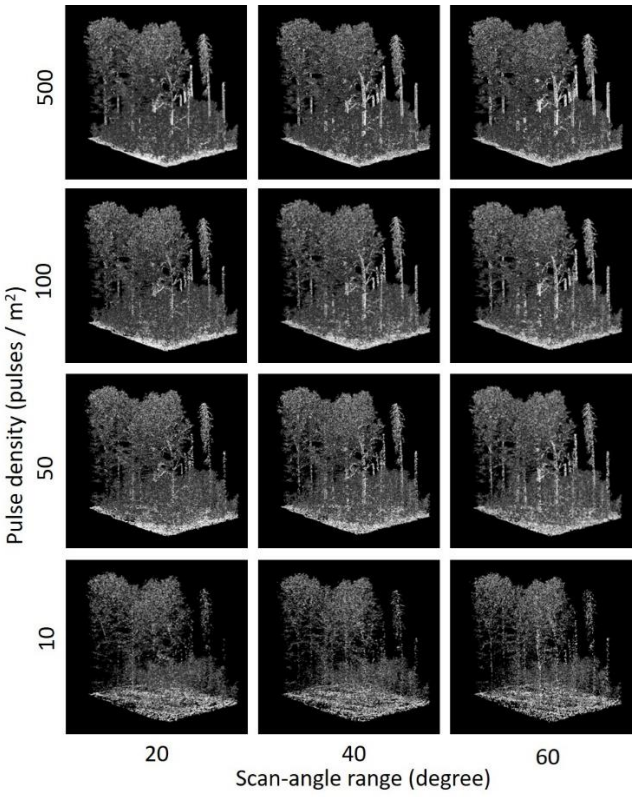

Figure S1. Stem and branch structure as a function of pulse density and scan-angle range. The area is approximately 30 by 30 m in a temperate mountain forest in the southwest Czech Republic. The number of returns is more sensitive to pulse density than to scan-angle range.

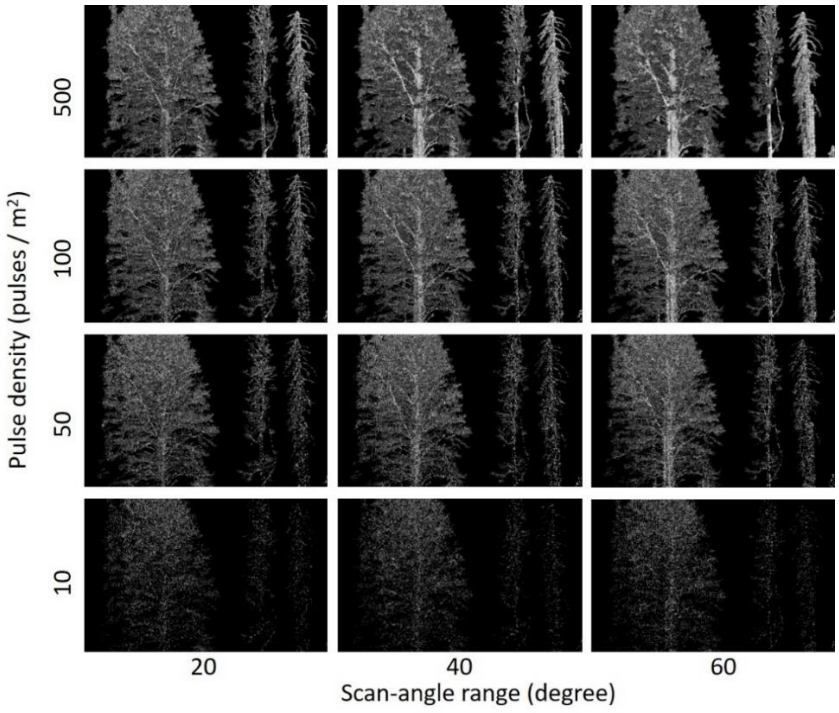

Figure S2. Stem and branch structure as a function of pulse density and scan-angle range, highlighting vegetation structure among prominent stems. Data are from high-density drone lidar in a temperate mountain forest in the southwest Czech Republic. The number of returns is more sensitive to pulse density than to scan-angle range.

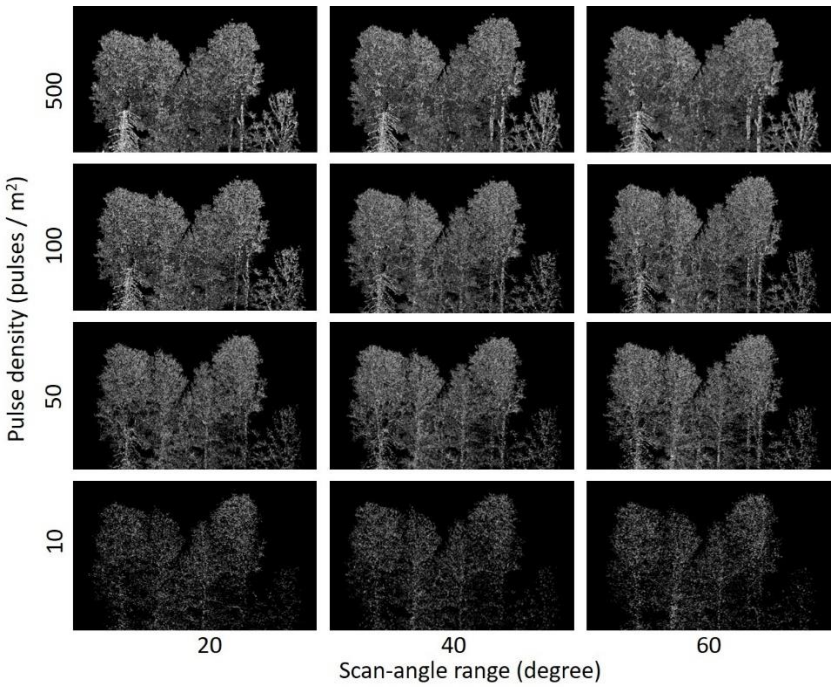

Figure S3. Stem and branch structure as a function of pulse density and scan-angle range, highlighting upper-canopy vegetation. Data are from high-density drone lidar in a temperate mountain forest in the southwest Czech Republic. The number of returns is more sensitive to pulse density than to scan-angle range.

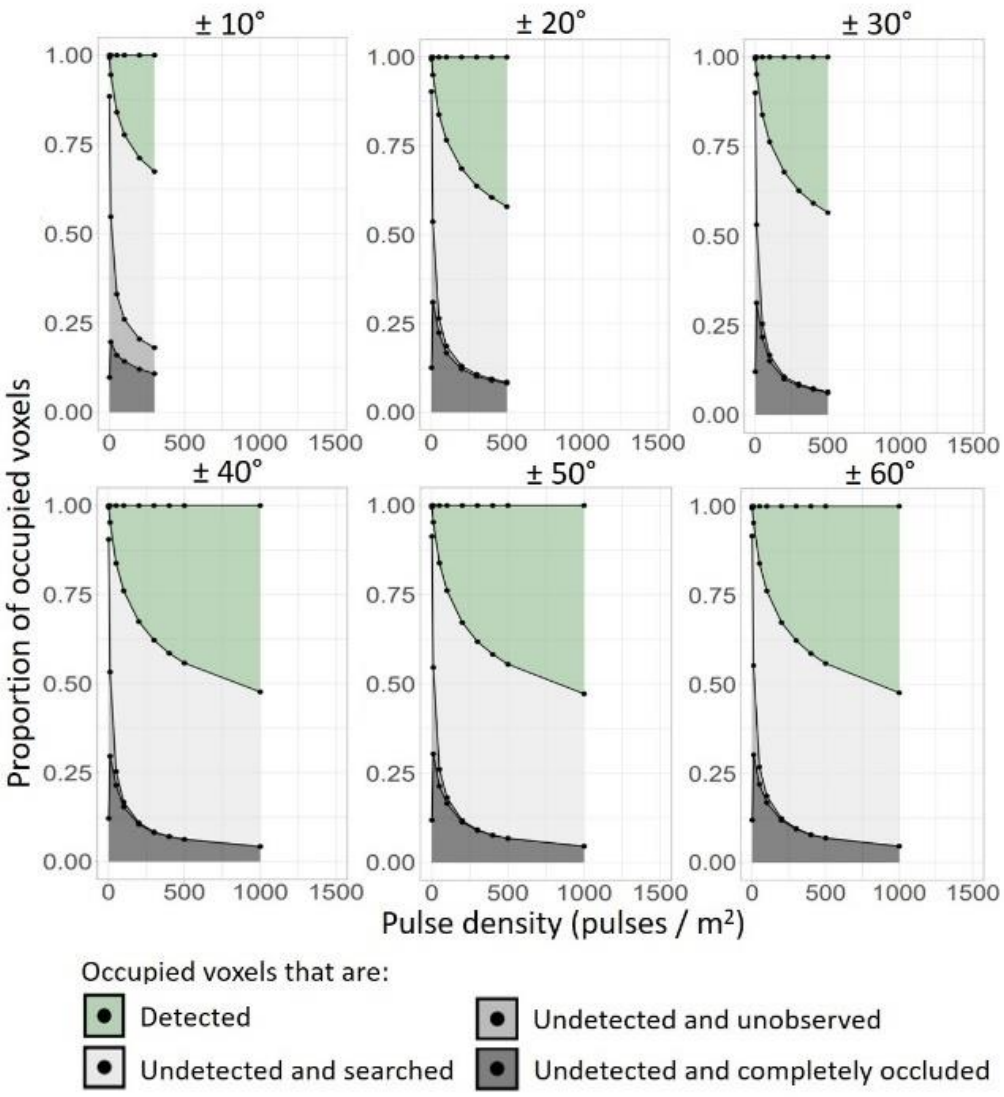

Figure S4. Proportions of occupied voxels that are detected and undetected as a function of pulse density and scan-angle range at plot #2. On each of the six panels, from left to right, the black dots represent pulse densities of 1, 10, 50, 100, 200, 300, 400, 500, 1,000, 1,500 pulses / m^2. Only 6 levels of scan-angle range (± 10 degrees, ± 20 degrees, ± 30 degrees, ± 40 degrees, ± 50 degrees, ± 60 degrees) are shown here because Figure 4 shows limited impact of scan-angle range after decoupling its impact from pulse density. Missing data points are associated with small sample sizes at certain combinations of scan-angle range and pulse density.

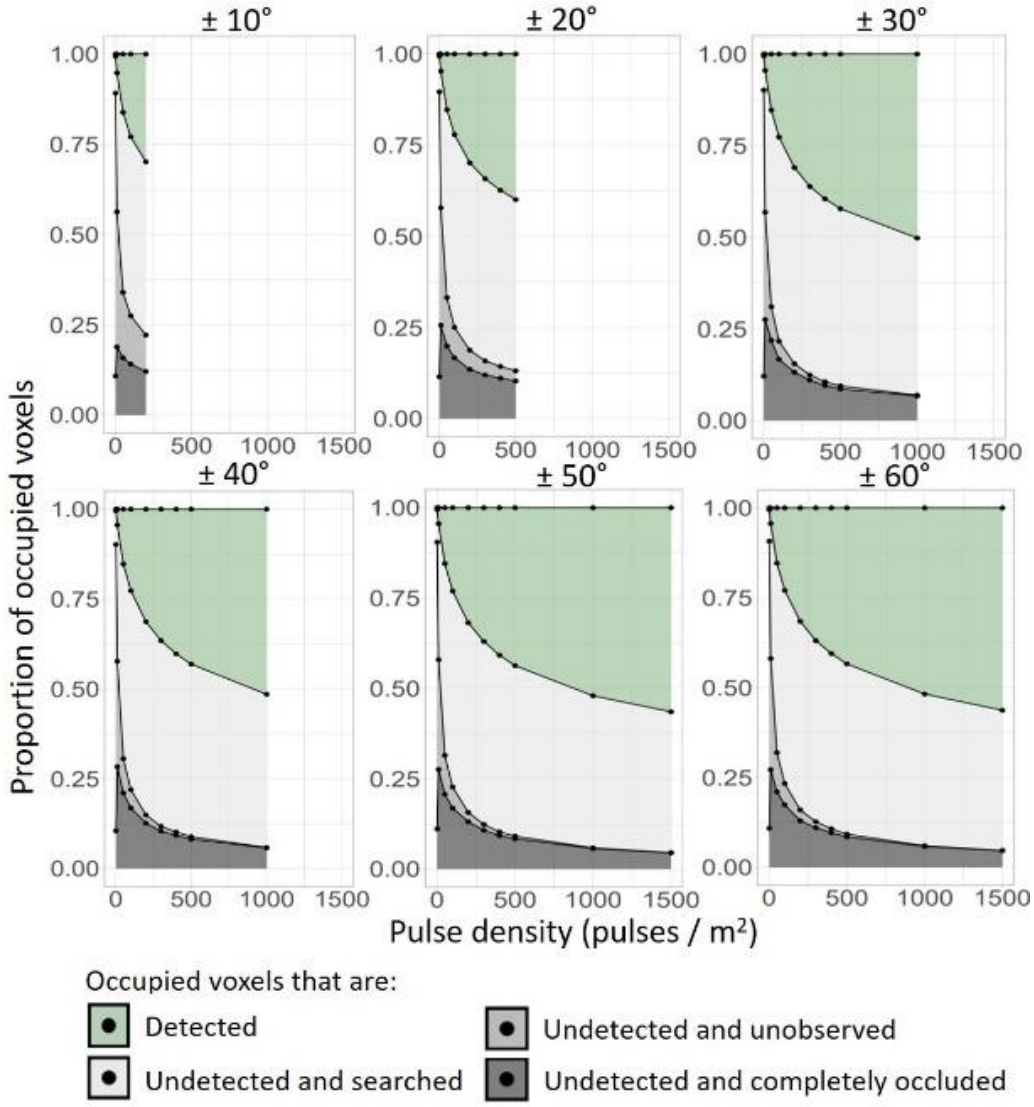

Figure S5. Proportions of occupied voxels that are detected and undetected as a function of pulse density and scan-angle range at plot #3. On each of the six panels, from left to right, the black dots represent pulse densities of 1, 10, 50, 100, 200, 300, 400, 500, 1,000, 1,500 pulses / m^2. Only 6 levels of scan-angle range (± 10 degrees, ± 20 degrees, ± 30 degrees, ± 40 degrees, ± 50 degrees, ± 60 degrees) are shown here because Figure 4 shows limited impact of scan-angle range after

decoupling its impact from pulse density. Missing data points are associated with small sample sizes at certain combinations of scan-angle range and pulse density.

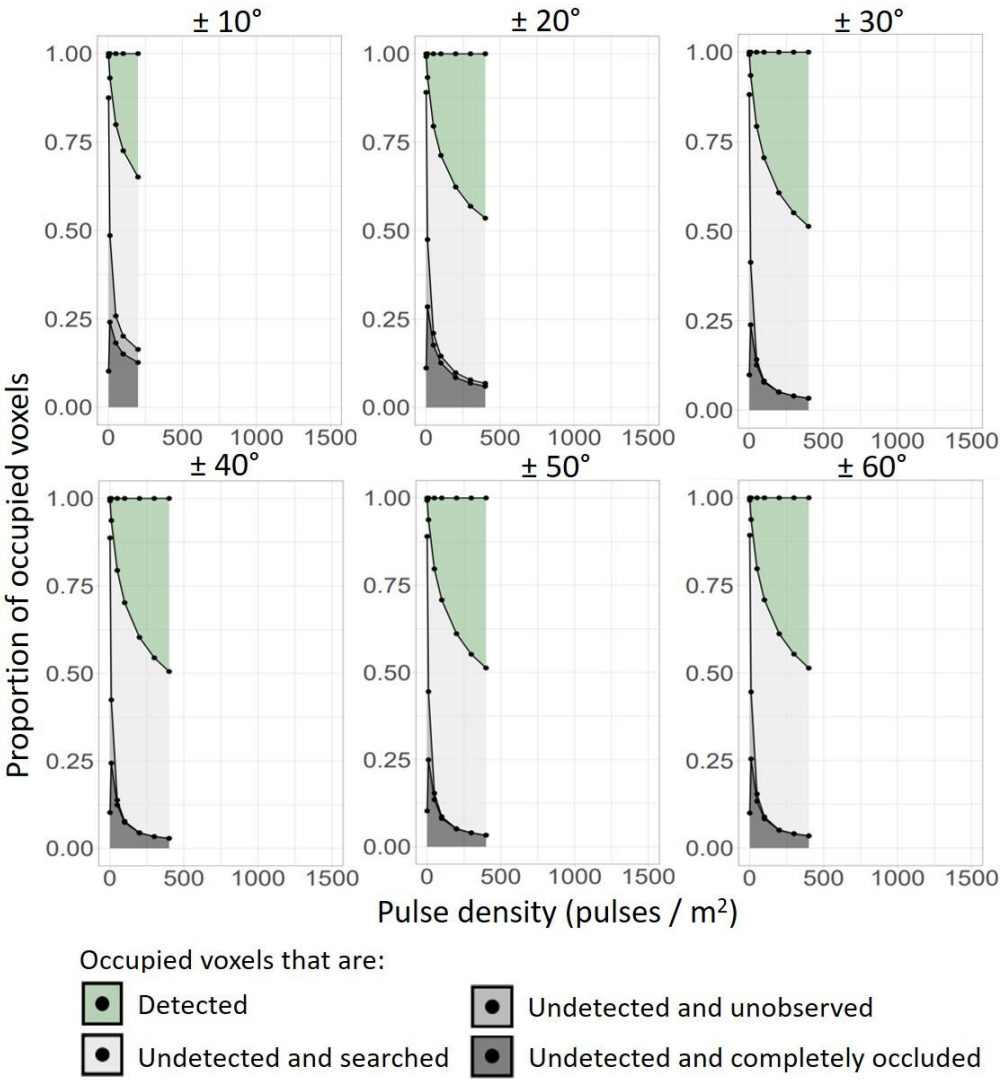

Figure S6. Proportions of occupied voxels that are detected and undetected as a function of pulse density and scan-angle range at plot #4. On each of the six panels, from left to right, the black dots represent pulse densities of 1, 10, 50, 100, 200, 300, 400, 500, 1,000, 1,500 pulses / m^2. Only 6 levels of scan-angle range (± 10 degrees, ± 20 degrees, ± 30 degrees, ± 40 degrees, ± 50 degrees, ± 60 degrees) are shown here because Figure 4 shows limited impact of scan-angle range after

decoupling its impact from pulse density. Missing data points are associated with small sample sizes at certain combinations of scan-angle range and pulse density.

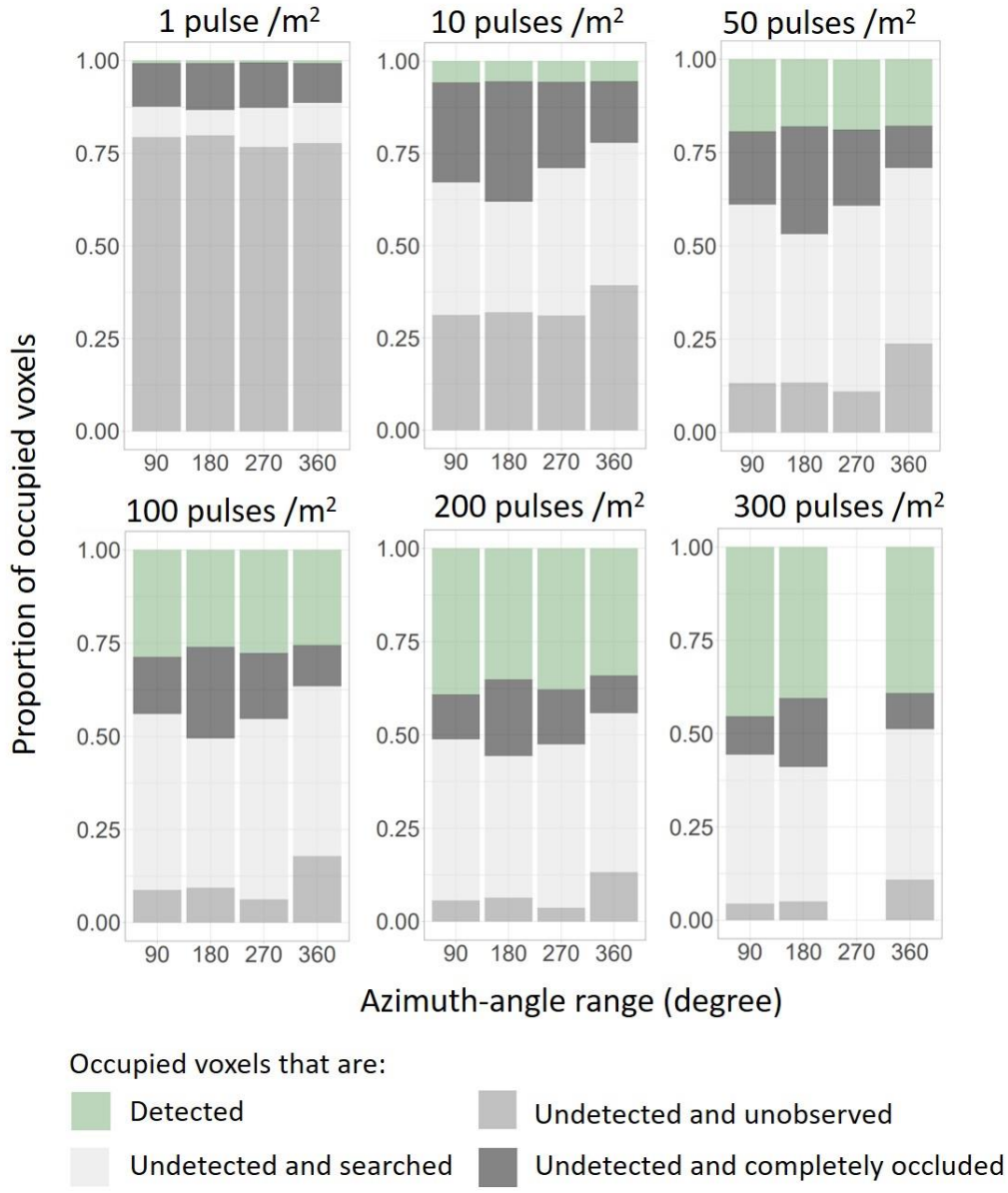

Figure S7. Proportions of occupied voxels that are detected and undetected as a function of pulse density and azimuth-angle range (plot #1). The azimuth-angle ranges are 0 – 90 degrees, 90 – 180 degrees, 180 – 270 degrees, and 270 – 360 degrees; they are labeled on the x-axis by the

right bound (i.e., 90, 180, 270, 360 respectively). Missing data points are associated with small sample sizes at certain combinations of azimuth-angle range and pulse density.

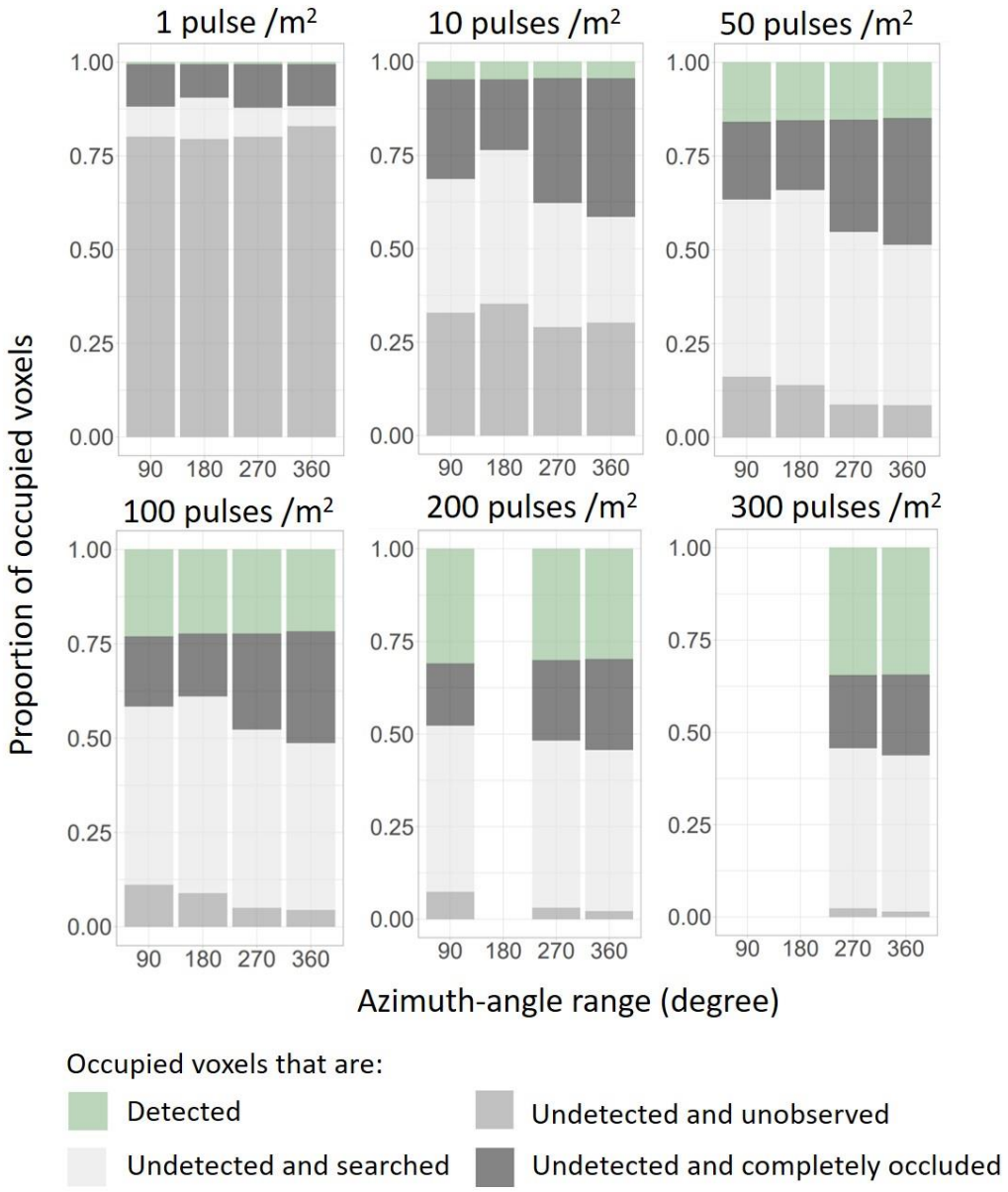

Figure S8. Proportions of occupied voxels that are detected and undetected as a function of pulse density and azimuth-angle range (plot #2). The azimuth-angle ranges are 0 – 90 degrees, 90 – 180

degrees, 180 – 270 degrees, and 270 – 360 degrees; they are labeled on the x-axis by the right bound (i.e., 90, 180, 270, 360 respectively). Missing data points are associated with small sample sizes at certain combinations of azimuth-angle range and pulse density.

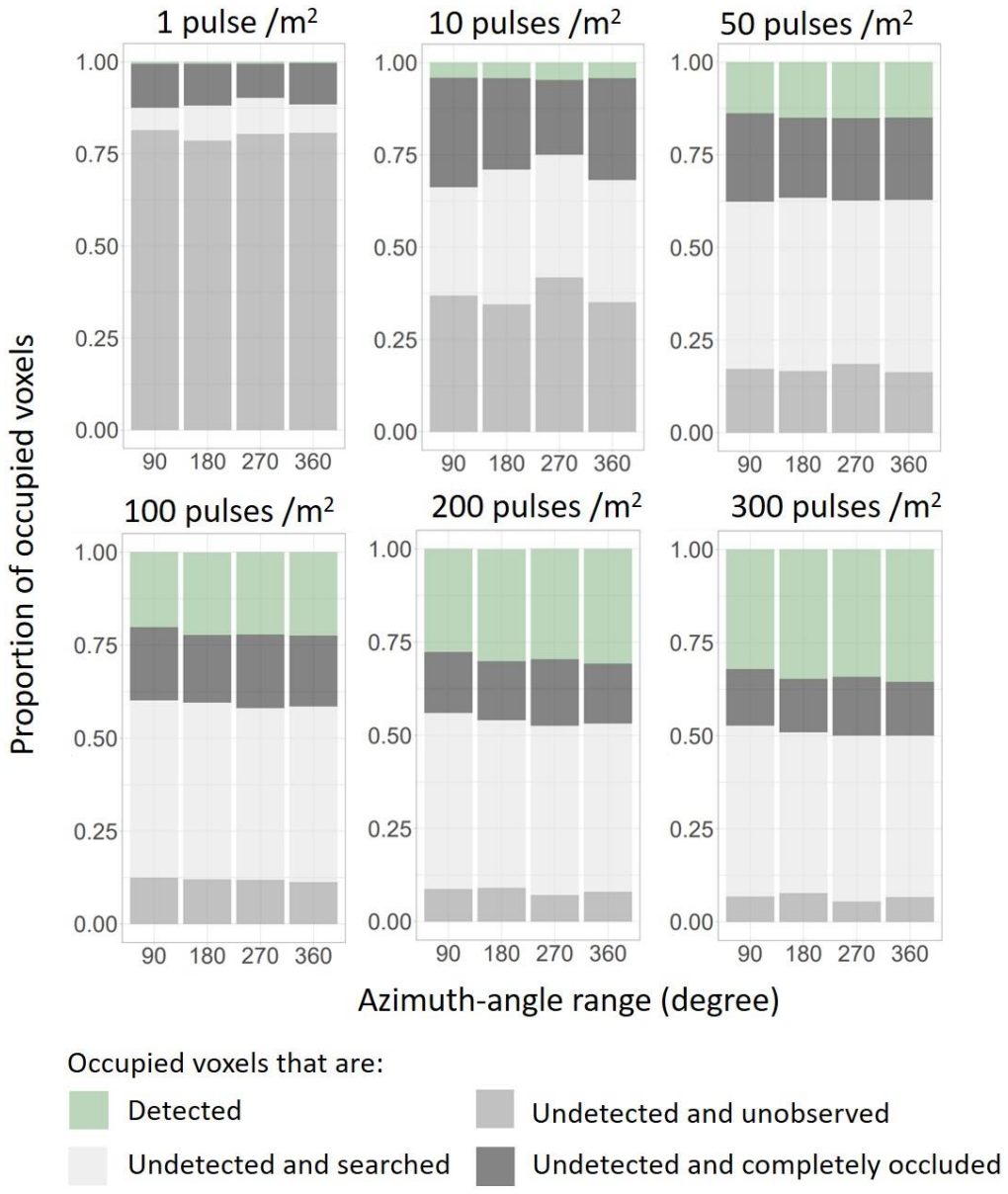

Figure S9. Proportions of occupied voxels that are detected and undetected as a function of pulse density and azimuth-angle range (plot #3). The azimuth-angle ranges are 0 – 90 degrees, 90 – 180

degrees, 180 – 270 degrees, and 270 – 360 degrees; they are labeled on the x-axis by the right bound (i.e., 90, 180, 270, 360 respectively). Missing data points are associated with small sample sizes at certain combinations of azimuth-angle range and pulse density.

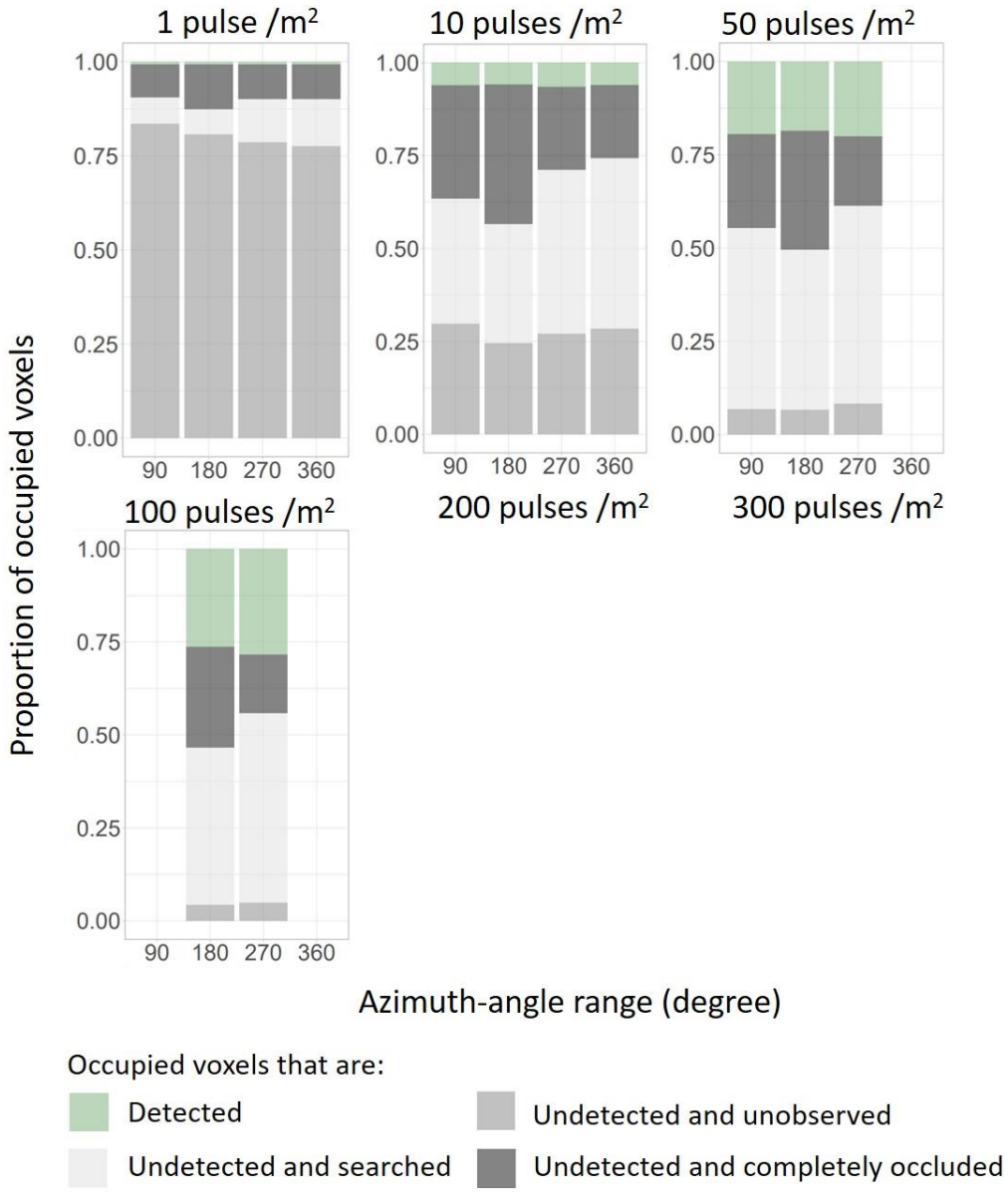

Figure S10. Proportions of occupied voxels that are detected and undetected as a function of pulse density and azimuth-angle range (plot #4). The azimuth-angle ranges are 0 – 90 degrees, 90 – 180 degrees, 180 – 270 degrees, and 270 – 360 degrees; they are labeled on the x-axis by the right

bound (i.e., 90, 180, 270, 360 respectively). Missing data points are associated with small sample sizes at certain combinations of azimuth-angle range and pulse density.

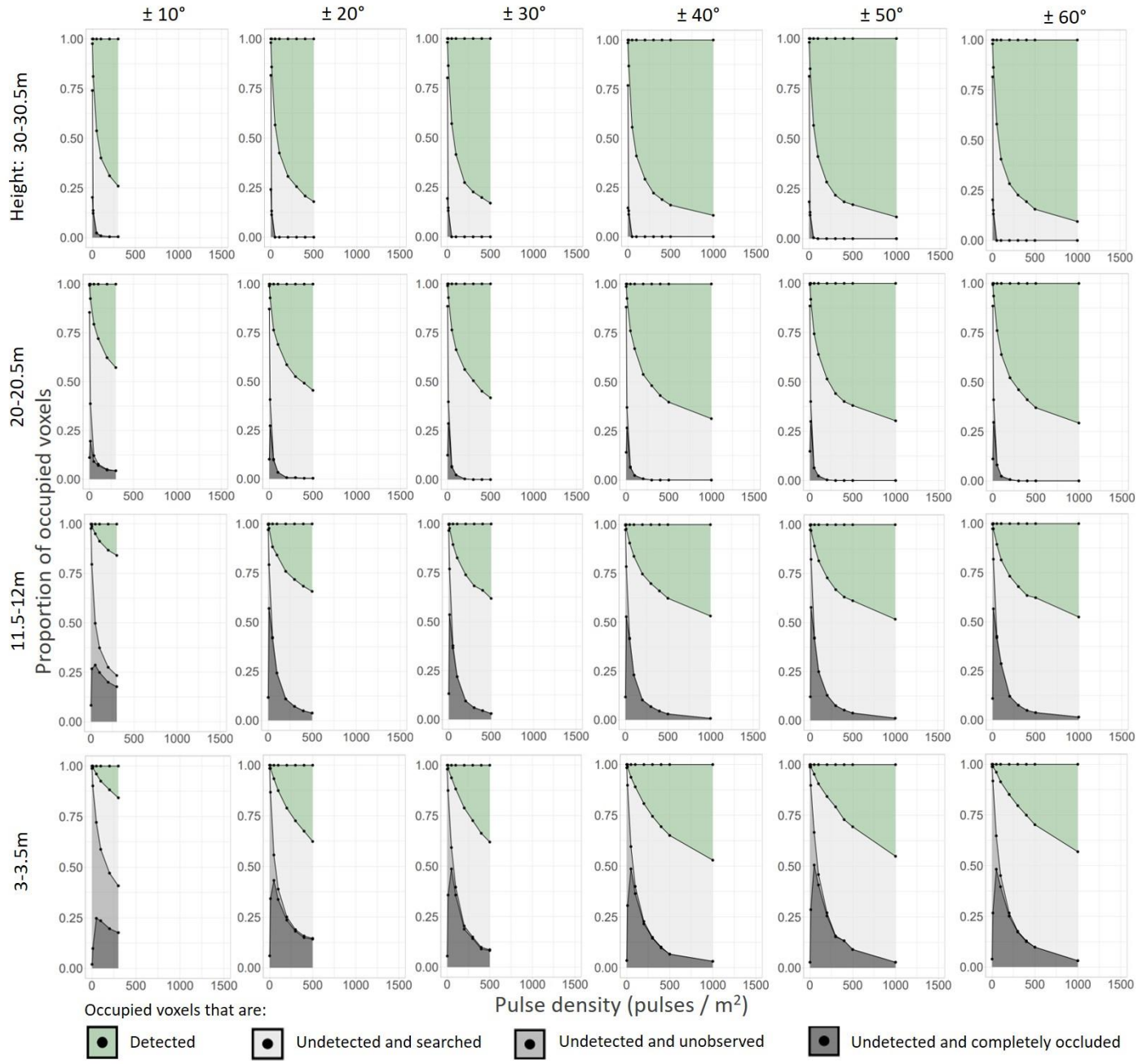

Figure S11. Proportions of occupied voxels that are detected and undetected as a function of pulse density and scan-angle range at multiple heights aboveground in the 100 m^2 plot (plot #2). Missing

data points are associated with small sample sizes at certain combinations of scan-angle range and pulse density.

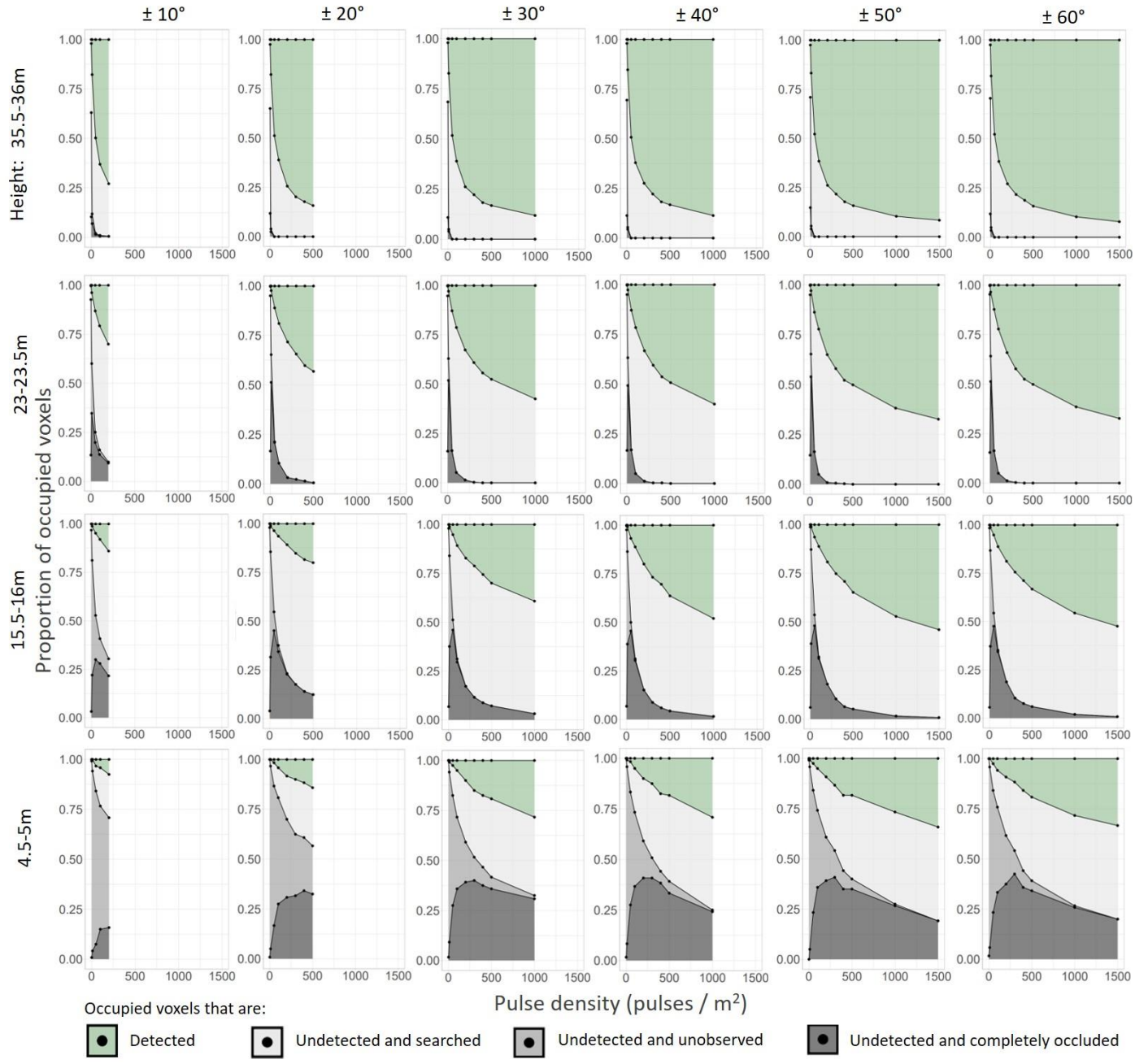

Figure S12. Proportions of occupied voxels that are detected and undetected as a function of pulse density and scan-angle range at multiple heights aboveground in the 100 m^2 plot (plot #3). Missing

data points are associated with small sample sizes at certain combinations of scan-angle range and pulse density.

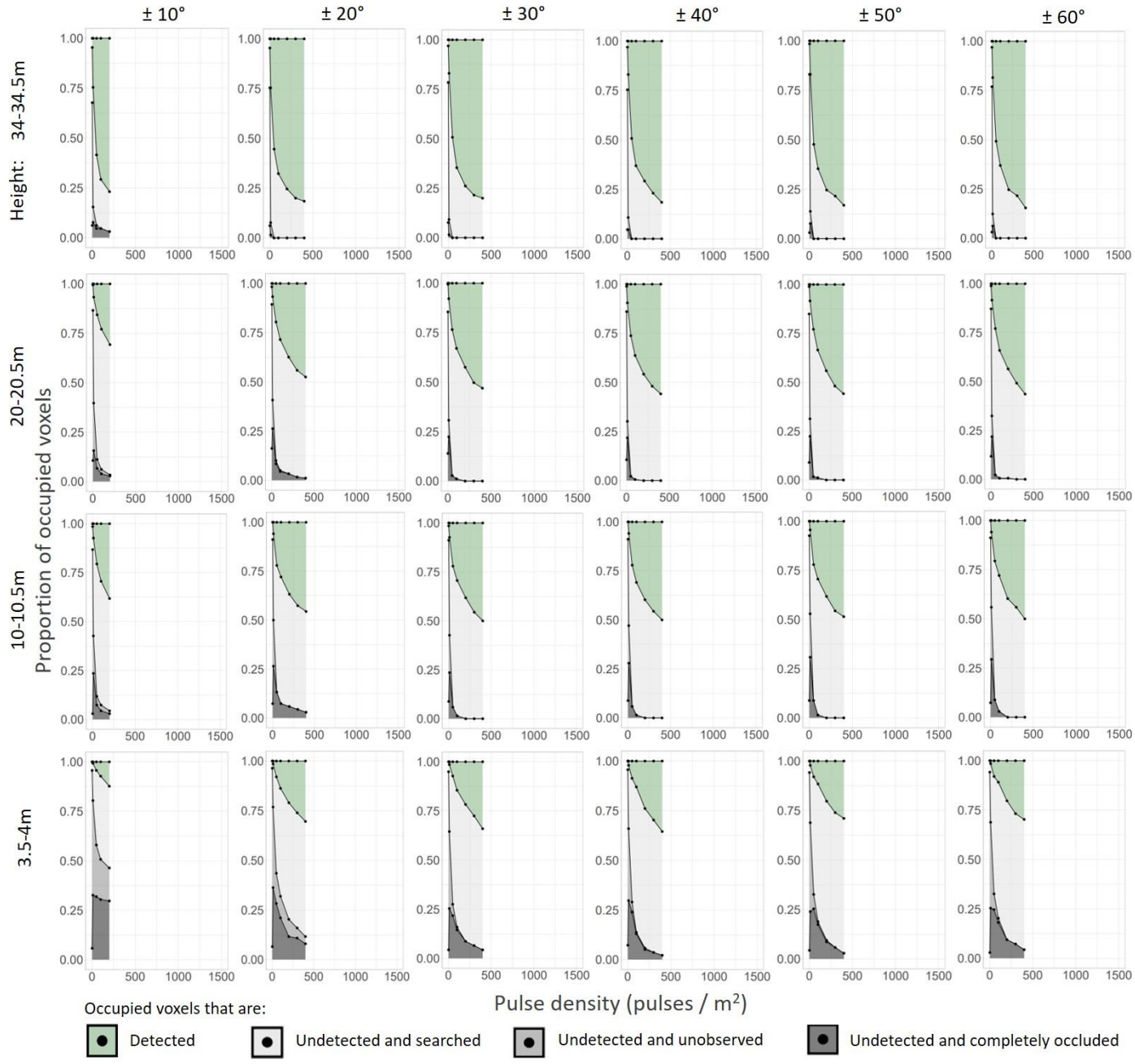

Figure S13. Proportions of occupied voxels that are detected and undetected as a function of pulse density and scan-angle range at multiple heights aboveground in the 100 m^2 plot (plot #4). Missing

data points are associated with small sample sizes at certain combinations of scan-angle range and pulse density.

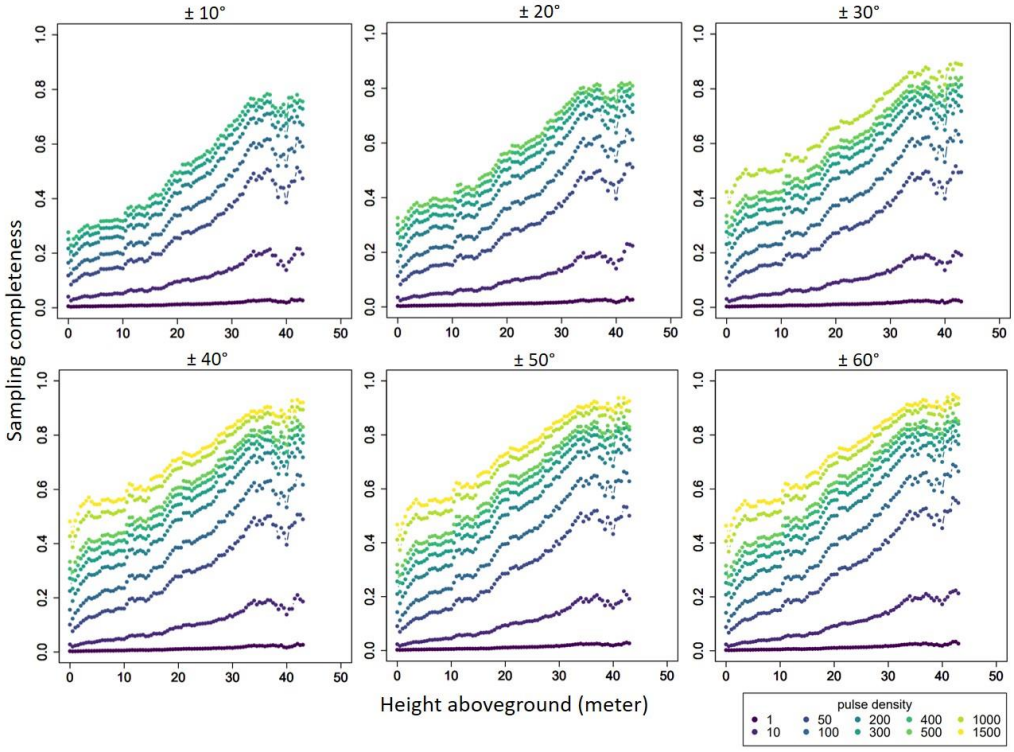

Figure S14. The proportion of detected voxels at different heights as a function of pulse density and scan-angle range in the 1 ha plot. Only 6 levels of scan-angle range (± 10 degrees, ± 20 degrees, ± 30 degrees, ± 40 degrees, ± 50 degrees, ± 60 degrees) are shown here because Figure 4 shows limited impact of scan-angle range after decoupling its impact from pulse density. Missing data points are associated with small sample sizes at some combinations of scan-angle range and pulse density.

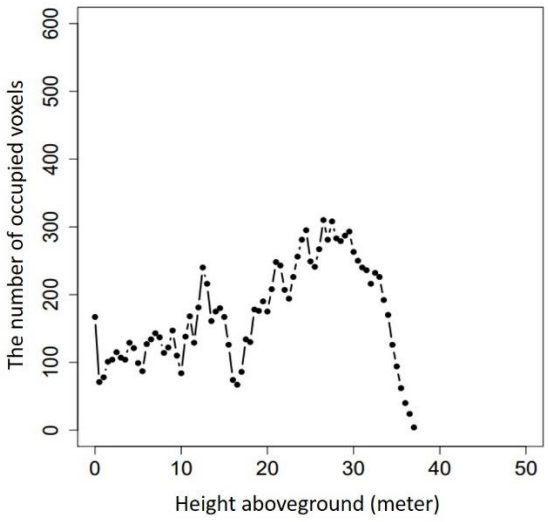

Figure S15. The number of occupied voxels at each height aboveground in the 100 m^2 plot (plot #1).

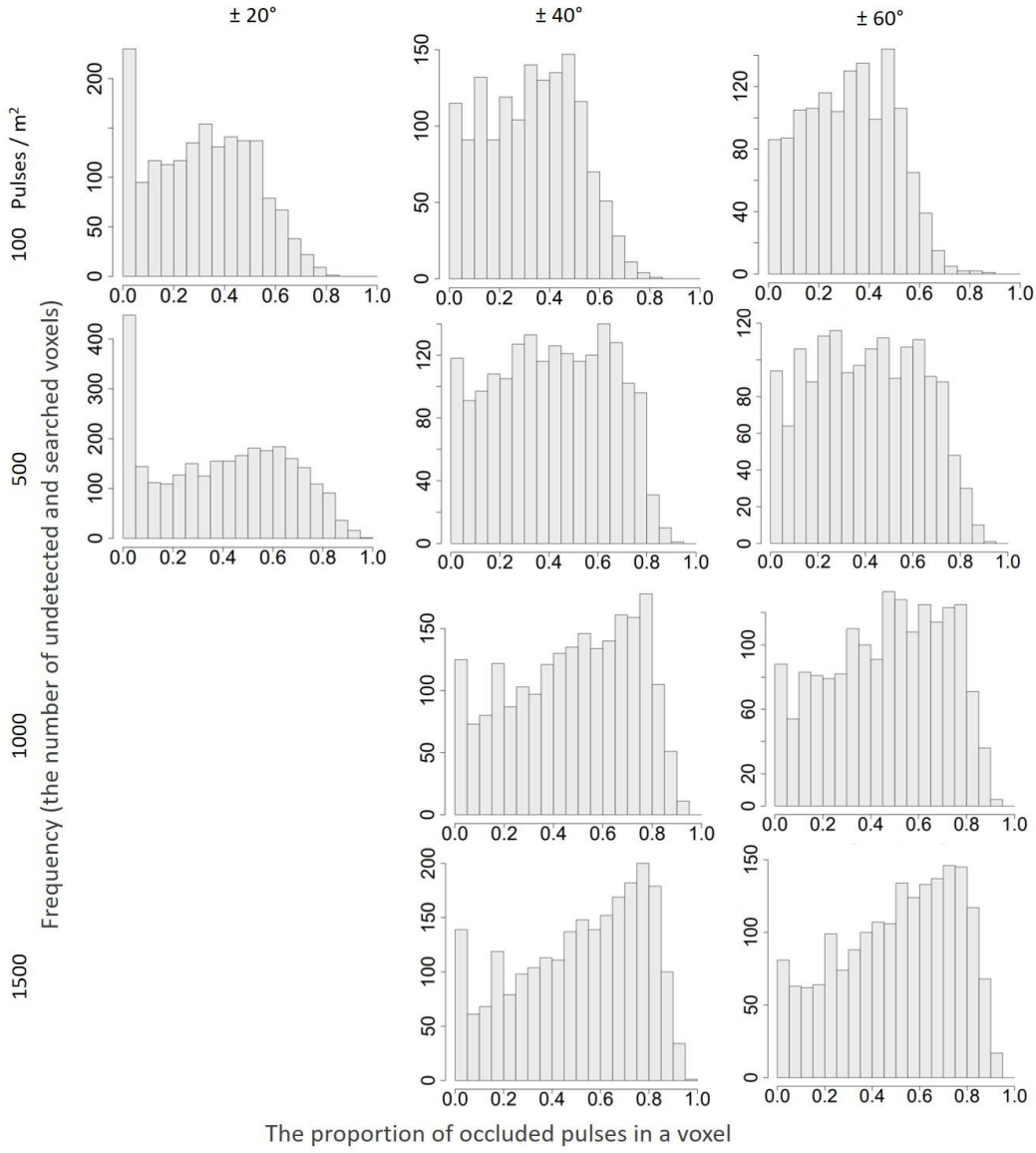

Figure S16. Proportions of occluded pulses in undetected and searched voxels as a function of pulse density and azimuth-angle range (plot #1). Missing data points are associated with small sample sizes at certain combinations of scan-angle range and pulse density.

Table S1. Percentages of detected voxels as a function of pulse density and scan-angle range for plot #1 (standard deviation provided). Data are from high-density drone lidar in a temperate

mountain forest in the southwest Czech Republic. Missing data points are associated with small sample sizes at some combinations of scan-angle range and pulse density.

	± 10°	± 20°	± 30°	± 40°	± 50°	± 60°
1	(0.9 ± 0.02)%	(0.9 ± 0.02)%	(0.8 ± 0.02)%	(0.8 ± 0.02)%	(0.8 ± 0.01)%	(0.8 ± 0.01)%
10	(7.3 ± 0.11)%	(7.0 ± 0.05)%	(7.0 ± 0.11)%	(6.9 ± 0.05)%	(6.9 ± 0.07)%	(6.9 ± 0.06)%
50	(20.8 ± 0.16)%	(20.7 ± 0.17)%	(21.8 ± 0.16)%	(21.9 ± 0.15)%	(22.0 ± 0.20)%	(22.2 ± 0.25)%
100	(28.6 ± 0.16)%	(29.1 ± 0.25)%	(31.0 ± 0.18)%	(31.5 ± 0.16)%	(31.9 ± 0.12)%	(32.0 ± 0.32)%
200	(36.8 ± 0.17)%	(37.9 ± 0.20)%	(41.2 ± 0.24)%	(42.0 ± 0.32)%	(42.6 ± 0.19)%	(42.8 ± 0.25)%
300	(41.7 ± 0.19)%	(42.9 ± 0.18)%	(47.1 ± 0.19)%	(48.3 ± 0.24)%	(48.9 ± 0.21)%	(49.2 ± 0.18)%
400	-	(46.5 ± 0.25)%	(51.4 ± 0.20)%	(52.6 ± 0.22)%	(53.5 ± 0.22)%	(53.7 ± 0.15)%
500	-	(49.5± 0.09)%	(54.7 ± 0.15)%	(55.9 ± 0.20)%	(56.8 ± 0.26)%	(57.1 ± 0.34)%
1000	-	-	(64.2 ± 0.18)%	(65.8 ± 0.22)%	(67.0 ± 0.15)%	(67.1 ± 0.19)%
1500	-	-	-	(71.0 ± 0.20)%	(72.2 ± 0.21)%	(72.4 ± 0.12)%

Table S2. Percentages of undetected and searched voxels as a function of pulse density and scan-angle range for plot #1 (standard deviation provided). Data are from high-density drone lidar in a temperate mountain forest in the southwest Czech Republic. Missing data points are associated with small sample sizes at some combinations of scan-angle range and pulse density.

	± 10°	± 20°	± 30°	± 40°	± 50°	± 60°
1	(8.7 ± 0.73)%	(9.3 ± 1.03)%	(10.9 ± 0.85)%	(9.2 ± 0.65)%	(10.1 ± 0.77)%	(9.4 ± 0.82)%
10	(32.2 ± 0.82)%	(36.7 ± 1.13)%	(41.0 ± 1.25)%	(39.0 ± 0.89)%	(39.2 ± 1.00)%	(38.8 ± 0.77)%

50	(39.7 ± 0.39)%	(45.4 ± 0.34)%	(49.2 ± 0.72)%	(49.6 ± 0.21)%	(50.4 ± 0.66)%	(50.4 ± 0.70)%
100	(38.7 ± 0.34)%	(44.5 ± 0.63)%	(47.7 ± 0.73)%	(48.9 ± 0.70)%	(49.4 ± 0.42)%	(49.1 ± 0.62)%
200	(36.0 ± 0.28)%	(41.5 ± 0.27)%	(43.9 ± 0.44)%	(44.4 ± 0.27)%	(44.9 ± 0.36)%	(44.3 ± 0.54)%
300	(33.6 ± 0.29)%	(39.2 ± 0.46)%	(40.6 ± 0.59)%	(40.8 ± 0.33)%	(41.4 ± 0.23)%	(40.9 ± 0.38)%
400	-	(37.3 ± 0.28)%	(38.1 ± 0.33)%	(38.4 ± 0.31)%	(38.3 ± 0.26)%	(38.2 ± 0.36)%
500	-	(35.4 ± 0.32)%	(36.1 ± 0.25)%	(36.3 ± 0.33)%	(36.2 ± 0.36)%	(35.7 ± 0.38)%
1000	-	-	(29.3 ± 0.16)%	(28.9 ± 0.25)%	(28.5 ± 0.11)%	(28.1 ± 0.21)%
1500	-	-	-	(24.8 ± 0.23)%	(24.2 ± 0.23)%	(23.9 ± 0.20)%

Table S3. Percentages of undetected and unobserved voxels as a function of pulse density and scan-angle range for plot #1 (standard deviation provided). Data are from high-density drone lidar in a temperate mountain forest in the southwest Czech Republic. Missing data points are associated with small sample sizes at some combinations of scan-angle range and pulse density.

	± 10°	± 20°	± 30°	± 40°	± 50°	± 60°
1	(76.7 ± 1.11)%	(77.3 ± 1.30)%	(76.0 ± 0.74)%	(76.6 ± 0.51)%	(77.4 ± 1.03)%	(77.3 ± 1.10)%
10	(28.9 ± 0.92)%	(29.0 ± 0.78)%	(27.7 ± 1.16)%	(27.7 ± 1.04)%	(27.3 ± 0.88)%	(27.5 ± 0.71)%
50	(12.3 ± 0.30)%	(10.9 ± 0.29)%	(9.7 ± 0.63)%	(7.9 ± 0.34)%	(8.1 ± 0.37)%	(8.3 ± 0.41)%
100	(8.4 ± 0.27)%	(7.2 ± 0.23)%	(5.6 ± 0.31)%	(3.8 ± 0.20)%	(3.8 ± 0.29)%	(3.8 ± 0.32)%
200	(5.8 ± 0.16)%	(4.4 ± 0.22)%	(2.8 ± 0.16)%	(1.6 ± 0.15)%	(1.5 ± 0.09)%	(1.6 ± 0.12)%
300	(4.4 ± 0.13)%	(3.4 ± 0.16)%	(1.9 ± 0.08)%	(1.0 ± 0.08)%	(0.9 ± 0.09)%	(0.9 ± 0.06)%
400	-	(2.7 ± 0.15)%	(1.4 ± 0.07)%	(0.6 ± 0.04)%	(0.5 ± 0.06)%	(0.6 ± 0.08)%
500	-	(2.2 ± 0.10)%	(1.1 ± 0.07)%	(0.5 ± 0.04)%	(0.4 ± 0.04)%	(0.4 ± 0.06)%

1000	-	-	(0.5 ± 0.04)%	(0.1 ± 0.03)%	(0.1 ± 0.02)%	(0.1 ± 0.03)%
1500	-	-	-	(0.1 ± 0.02)%	(0.1 ± 0.01)%	(0.1 ± 0.01)%

Table S4. Percentages of undetected and completely occluded voxels as a function of pulse density and scan-angle range for plot #1 (standard deviation provided). Data are from high-density drone lidar in a temperate mountain forest in the southwest Czech Republic. Missing data points are associated with small sampled sizes at some combinations of scan-angle range and pulse density.

	± 10°	± 20°	± 30°	± 40°	± 50°	± 60°
1	(13.7 ± 1.60)%	(12.5 ± 1.71)%	(12.3 ± 1.39)%	(13.4 ± 1.02)%	(11.7 ± 1.47)%	(12.5 ± 1.19)%
10	(31.6 ± 1.22)%	(27.3 ± 1.46)%	(24.3 ± 1.90)%	(26.4 ± 1.41)%	(26.6 ± 1.10)%	(26.8 ± 1.06)%
50	(27.2 ± 0.54)%	(23.0 ± 0.50)%	(19.3 ± 0.81)%	(20.6 ± 0.51)%	(19.5 ± 0.67)%	(19.1 ± 0.62)%
100	(24.3 ± 0.55)%	(19.2 ± 0.61)%	(15.7 ± 0.72)%	(15.8 ± 0.70)%	(14.9 ± 0.53)%	(15.1 ± 0.69)%
200	(21.4 ± 0.27)%	(16.2 ± 0.32)%	(12.1 ± 0.39)%	(12.0 ± 0.39)%	(11.0 ± 0.36)%	(11.3 ± 0.47)%
300	(20.3 ± 0.22)%	(14.5 ± 0.43)%	(10.4 ± 0.47)%	(9.9 ± 0.15)%	(8.8 ± 0.23)%	(9.0 ± 0.34)%
400	-	(13.5 ± 0.28)%	(9.1 ± 0.23)%	(8.4 ± 0.23)%	(7.7 ± 0.19)%	(7.5 ± 0.23)%
500	-	(12.9 ± 0.23)%	(8.1 ± 0.17)%	(7.3 ± 0.25)%	(6.6 ± 0.21)%	(6.8 ± 0.33)%
1000	-	-	(6.0 ± 0.15)%	(5.2 ± 0.10)%	(4.4 ± 0.12)%	(4.7 ± 0.21)%
1500	-	-	-	(4.1± 0.08)%	(3.5 ± 0.09)%	(3.6 ± 0.11)%

CHAPTER 2

Is the variability in ecosystem structure primarily predicted by the physical environment given widespread human modification?

Dafeng Zhang[1,2], James R. Kellner[1,2]

1. Department of Ecology, Evolution and Organismal Biology, Brown University, Providence RI, 02912, United States of America

2. Institute at Brown for Environment and Society, Brown University, Providence RI, 02912, United States of America

Abstract

Terrestrial ecosystem structure, as a fundamental property of terrestrial ecosystems, is linked to the flow and cycling of energy and nutrients, as well as to the habitat diversity and species richness of both plants and animals. Numerous remote sensing studies have quantified the spatial variation in ecosystem structure, but the reason for the variability is poorly understood, especially across the world's different biomes. Widespread human activities have modified the land surface and the ecosystem structure significantly. However, it is still unclear if the variability of ecosystem structure is still primarily predicted by the physical environment. Here we use data from a spaceborne waveform lidar, the Global Ecosystem Dynamics Investigation (GEDI), and coincident environmental and socio-economic datasets that represent human impacts and the physical environment, to investigate if human impacts add explanatory power to the variability in ecosystem structure that is known to be predicted by the physical environment. We used a machine learning model and permutation to investigate the explanatory power of variables that represent human impacts and the physical environment. We did not find evidence that human impacts add explanatory power to the model with physical variables. This does not necessarily mean that human impacts were not important for two reasons: (1) human impacts could be predicted by the physical environment, (2) there were too few anthropogenic variables than physical variables. This study demonstrates the importance of checking if the predictor variables are correlated when using permutation to evaluate the relative influence of predictor variables, a way to quantify variable importance that is widely adopted by machine learning models. In the context of explaining the variability in ecosystem structure, the current anthropogenic datasets may be insufficient to quantify the human impacts in comparison to the

physical environment due to the correlation between anthropogenic and physical variables and the small number of human datasets we have.

Keywords: Ecosystem structure, Global Ecosystem Dynamics Investigation, human impacts, permutation

1. Introduction

Ecosystem structure is the arrangement and distribution of vegetation material in the three-dimensional space (Gils and Wijngaarden, 1984; Graetz, 1990). It is closely related to ecosystem functioning, and will be a dominant factor in shaping the future of terrestrial ecosystems (Graetz, 1990; Spies, 1998; Migliavacca et al., 2021). For example, it modulates incoming light that can be used for photosynthesis (Béland and Baldocchi, 2021; Matsuo et al., 2021), and thus it influences the flow of energy and the cycling of nutrients (e.g., C, N). The heterogeneity in vertical structure provides diversified habitats for organisms (e.g., birds, bats, lianas), which increases species richness (MacArthur and MacArthur, 1961; Díaz et al., 2005; Carrasco et al., 2019; Meyer et al., 2020); and it is shown that the role of structure is sometimes more important than climate (Novella-Fernandez et al., 2022).

A conventional way to describe ecosystem structure in forest ecology is stratification, which represents the heterogeneity in vertical structure (Smith, 1973). Tropical rainforests are known for having multiple layers: the emergent layer, the canopy, the understory, and the forest floor. Terrestrial vegetated ecosystems tend to have fewer strata as latitude increases. However, synthesizing the ecosystem structure with at most four strata is a very coarse representation.

Lidar has enabled ecosystem structure to be synthesized from different dimensions (e.g., vertical, horizontal) and perspectives (e.g., leaf area, aboveground biomass) (Dubayah et al., 2020) at fine horizontal and vertical resolutions. Various structural metrics can be derived from lidar data: height that represents vertical structure (Lang et al., 2022), cover that represents the horizontal distribution of vegetation (Tang et al., 2019; Akturk et al., 2023), plant area index (PAI) or aboveground biomass density (AGBD) that depict ecosystem structure from a more synthesized dimension (Dubayah et al., 2022; Ma et al., 2024), and foliage height diversity (FHD) that represents the heterogeneity of vertical structure (Dubayah et al., 2021). Such structure metrics are widely used to understand past and current, and predict future of terrestrial ecosystems under changing climate and intensified human land use (Chen et al., 2019; Le Toan et al., 2011; Li et al., 2023; Ma et al., 2023). Although various data products of ecosystem structure have become available, we do not understand what explains the variation in ecosystem structure, especially on larger scales across different biomes given the widespread human activities all over the world (e.g., deforestation, agriculture expansion, urbanization).

It is demonstrated that the spatial variability of ecosystem structure is governed by physical gradients (e.g., climate and soils) (Holdridge, 1947; Clark and Clark, 2000; Asner et al., 2009; Higgins et al., 2015). On the other hand, as we enter the Anthropocene (Steffen et al., 2007; Ellis, 2011; Lewis and Maslin, 2015), ecosystem structure has been significantly modified by humans (Brandt et al., 2017; Song et al., 2018; Chen et al., 2019; Qin et al., 2021), and human activities have tended to be more intense (Foley et al., 2005; Gaffney and Steffen, 2017). However, it is unclear if the variability of ecosystem structure is still primarily predicted by the physical environment, given the human modification over the land surface. A recent study argued that human impacts are less important than climate (Li et al., 2023), but some

assumptions were not tested in the study. For example, one of the most important assumptions is that whether it is possible to disentangle the influence of human impacts and climate. In addition, they did not consider vegetation outside forests which was demonstrated to have substantial contribution to the land carbon sink (Brandt et al., 2020; Liu et al., 2023) (Brandt et al., 2020; Liu et al., 2023).

To update our understanding of the variation in ecosystem structure and the human impacts on the variation in comparison to the role of the physical environment, we ask three questions: (1) Can human impacts explain the variability of ecosystem structure? (2) Are human impacts redundant to the physical environment in explaining the variability of ecosystem structure? (3) Does the imbalanced number of physical and anthropogenic variables have an impact on our conclusion about the role of human impacts?

2. Data and Methods

2.1 Study sites

We selected 10 regions spanning 6 continents as our study sites (Figure 1, Table 1). The regions covered different terrestrial vegetated ecosystems (e.g., evergreen broadleaf forests in the southern Peruvian Amazon, grasslands in southeastern Australia) and involved different human activities (e.g., agriculture in Iowa in midwestern United States, deforestation in the Brazilian Amazon).

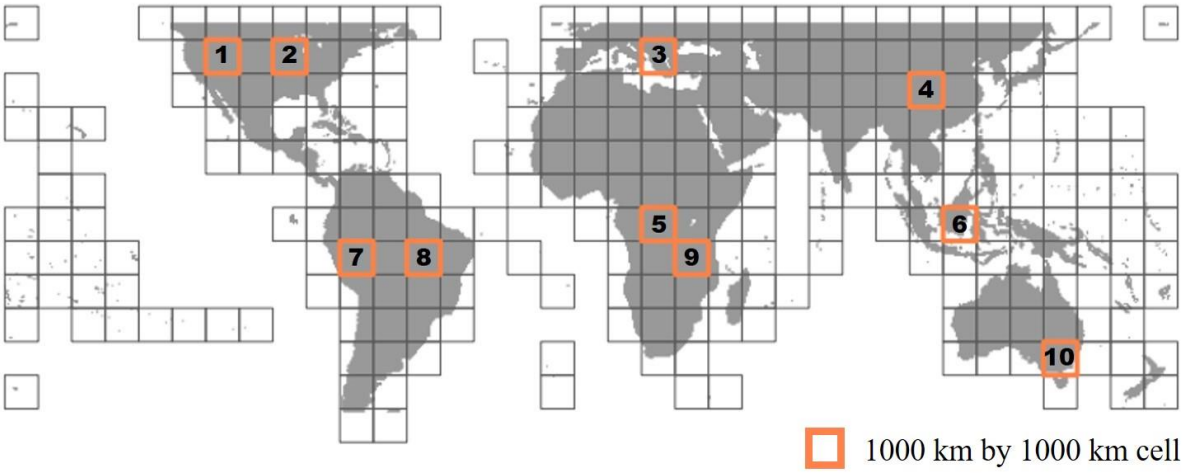

Figure 1. 10 selected sites in the world.

Table 1. Information about the selected sites across the world's continents

#	Site	Biome	Human activities or other information
1	US Rocky Mountains	Tropical and subtropical moist broadleaf forests	Predominantly conifers
2	Midwestern US	Temperate broadleaf and mixed forests	Agriculture
3	Eastern Europe	Temperate broadleaf and mixed forests	Mediterranean and mixed forests
4	Southwestern China	Temperate broadleaf and mixed forests	Higher elevation in the west; bamboo forests in Sichuan

5	DRC Congo basin	Tropical and subtropical moist broadleaf forests	Intact forests
6	Borneo	Tropical and subtropical moist broadleaf forests	Deforestation and degradation due to oil palm plantations
7	Southwest Amazon	Tropical and subtropical moist broadleaf forests	Intact forests
8	Brazilian Amazon	Tropical and subtropical moist broadleaf forests	Deforestation in northeastern Mato Grosso
9	African grasslands	Tropical and subtropical grasslands, savannas, and shrublands	Tanzania and Zambia
10	Southeastern Australia	Temperate grasslands, savannas, and shrublands	Savanna

2.2 Data preparation and preprocessing

2.2.1 Gridded structural metrics from GEDI

Global Ecosystem Dynamics Investigation (GEDI) is a spaceborne lidar onboard the International Space Station (ISS), whose coverage is from 51.6°S to 51.6°N (Dubayah et al., 2020). GEDI measures the reflected laser energy at heights from the canopy top to the ground (i.e., waveforms) at a footprint size of 25 m in diameter (Figure 2). In other words, GEDI samples the world by footprint and each footprint can be understood as a pixel containing three-

dimensional information in a map, while the original (or footprint-level) map from GEDI is not gridded or wall-to-wall (i.e., some pixels are left blank due to no footprint coverage).

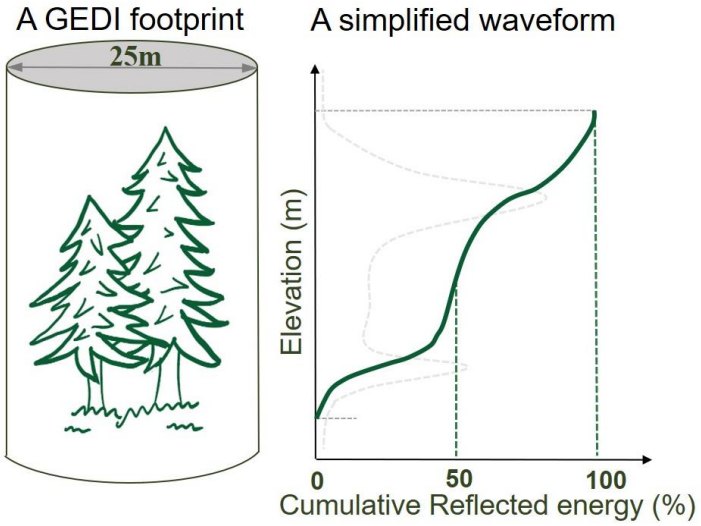

Figure 2. Illustration of a GEDI footprint and a waveform

We used five gridded structure metrics to represent ecosystem structure from different perspectives: canopy height (RH98), canopy cover, foliage height diversity (FHD), plant area index (PAI), and aboveground biomass density (AGBD). The structural metrics were produced with GEDI footprints from 2019 to 2022 (Burns et al., 2024). The footprints used to produce the gridded metrics were with an urban proportion of < 50% and water persistence of < 10% to ensure the coverage of vegetation. Due to quality issues, the density of footprints from only one year was not sufficient for producing global gridded maps. These gridded metrics (all are at 1 km spatial resolution) represented ecosystem structure from vertical (canopy height), horizontal (canopy cover) and synthesized (AGBD, PAI, FHD) dimensions.

2.2.2 Physical variables

Physical variables represent environmental variation in climate and substrate (Table S1). Climate variables are 19 bioclimatic variables from WorldClim2 (Fick and Hijmans, 2017). There were 11 temperature-relevant variables (bio1 to bio11) and 8 precipitation-relevant variables (bio12-bio19). The substrate variables include elevation, slope and aspect from Shuttle Radar Topography Mission (Farr and Kobrick, 2000), and 9 edaphic variables from SoilGrids 2.0 (Hengl et al., 2017). For each edaphic variable, we calculated the weighted mean from 0 – 2 m soil depth. We then resampled the 31 physical variables to 1 km spatial resolution, which is consistent with the resolution of gridded GEDI structure metrics.

2.2.3 Anthropogenic variables

We used 5 socioeconomic datasets to inform human activities: the global Human Modification (gHM) index (Kennedy et al., 2019), population density (Center for International Earth Science Information Network - CIESIN - Columbia University, 2018), nighttime light data (Elvidge et al., 2021), road density (Meijer et al., 2018) and world settlement footprint (Marconcini et al., 2021).

Human Modification index (gHM) is a complex and highly synthesized index ranging from 0 to 1 calculated based on 13 anthropogenic stressors (e.g., human settlement, agriculture) (Kennedy et al., 2019). Greater values represent greater degrees of human modification of terrestrial lands. Despite the comprehensiveness of the data, the year of it is around 2016, while the gridded GEDI data are around 2020. In order to capture the more up-to-date anthropogenic influence, we employed four more anthropogenic variables that were around 2020. Nighttime light data in 2020 is the radiation at night and reflects where there are intense human activities (Zhao et al., 2019). The population density we used for later analyses was also in the year of 2020.

Road density in 2018 is the total road lengths per unit area and studies show places with higher road density tend to be more influenced by humans (Cai et al., 2013). We generated a 1 km road density map using the GRIP global road database in the way the GRIP team generated their 5 arcmin (approximately 9.28 km) road density map.

World settlement footprint in 2019 is originally a binary dataset informing the locations of human built-ups and the spatial resolution is 10 m. We converted the spatial resolution to 1 km by aggregating the pixels and calculating the proportion of human built-ups within each 1 km pixel.

2.3 Permutation analyses

To quantify the explanatory power of the physical and anthropogenic variables to the variation in ecosystem structure, we ran the random forest model in the 10 sites. The predictor variables are the physical and anthropogenic variables, and the response variables for the model are the structural metrics from GEDI.

We permutated physical or anthropogenic variables and used the permutated variables to train the random forest model. Permutation removes information by disrupting the inherent structure in the predictor variables. Unlike simply removing variables, which modifies model structure, permutation retains all predictors but shuffles their values, thereby breaking any underlying correlations between the predictors and response variables.

2.3.1 Three main scenarios

In each site, we employed three permutation scenarios to run the random forest model: (1) full model with no permutation, (2) model with physical variables (and permuted anthropogenic variables), (3) model with anthropogenic variables (and permuted physical variables). And we compared the R-squared and root mean squared error (RMSE) to quantify the

explanatory power of different groups of predictors from the three permutation scenarios. Within each site under each scenario, we randomly sampled 100,000 pixels to run the random forest model. Each time when we ran the model, we calculated the mean R-squared or mean RMSE from the test set in the five-fold cross-validation. We used the arithmetic mean of the mean R-squared or mean RMSE from 10 repetitions as the final model performance for comparison.

2.3.2 A random selection of five variables

We used 31 physical variables and 5 anthropogenic variables. To investigate if the unbalanced number of anthropogenic and physical variables has an influence on the results, we randomly selected five variables to permute and repeated the process 1000 times to generate the distribution of R-squared. We then compared the R-squared from the scenario when anthropogenic variables were permuted to investigate if permutating anthropogenic variables had a greater impact on the model performance than permuting a random selection of five variables. We calculated the p-value using the proportion of the R-squared values from the distribution that were smaller than the R-squared from permuting anthropogenic variables. We used a significant level of 0.05. Note that here we only used the canopy height (RH98) as the response variable because results based on different structure metrics did not vary much.

2.3.3 Other permutation scenarios

We also performed two more versions of the permutation analysis. The first version employed two copies of each predictor variable. Five permutation scenarios were used: (1) no permutation, (2) permuting one copy of physical variables, (3) permuting two copies of physical variables, (4) permuting one copy of anthropogenic variables, (5) permuting two copies of anthropogenic variables. The other version used principle components (PCs) from PCA analyses of the anthropogenic and physical variables respectively. We used 4 PCs of anthropogenic

variables and 4 PCs of physical variables for the random forest model, such that the number of anthropogenic variables and the number of physical variables were equal.

2.4 Principle component analysis (PCA)

We did three versions of PCA in each site: (1) PCA using all anthropogenic and physical variables, (2) PCA using anthropogenic variables, (3) PCA using physical variables.

3. Results

3.1 Can human impacts explain the variability of ecosystem structure?

Anthropogenic variables explained 5.51% – 43.54% of the variations in the structural metrics across the 10 sites used in this study (Figure 3, Anthr). However, we found no evidence that human impacts add noticeable explanatory power to the variability in ecosystem structure in most of the sites, except site #2, site #5, site #7, and site #9 (Figure 3, 4). In other words, when adding anthropogenic variables to the model with physical variables, the R-squared or RMSE in most sites did not vary much (Figure 3, 4, from Phy to All). Among all the structure metrics, the predictor variables explained less or a similar amount of variation in AGBD compared to other structure metrics.

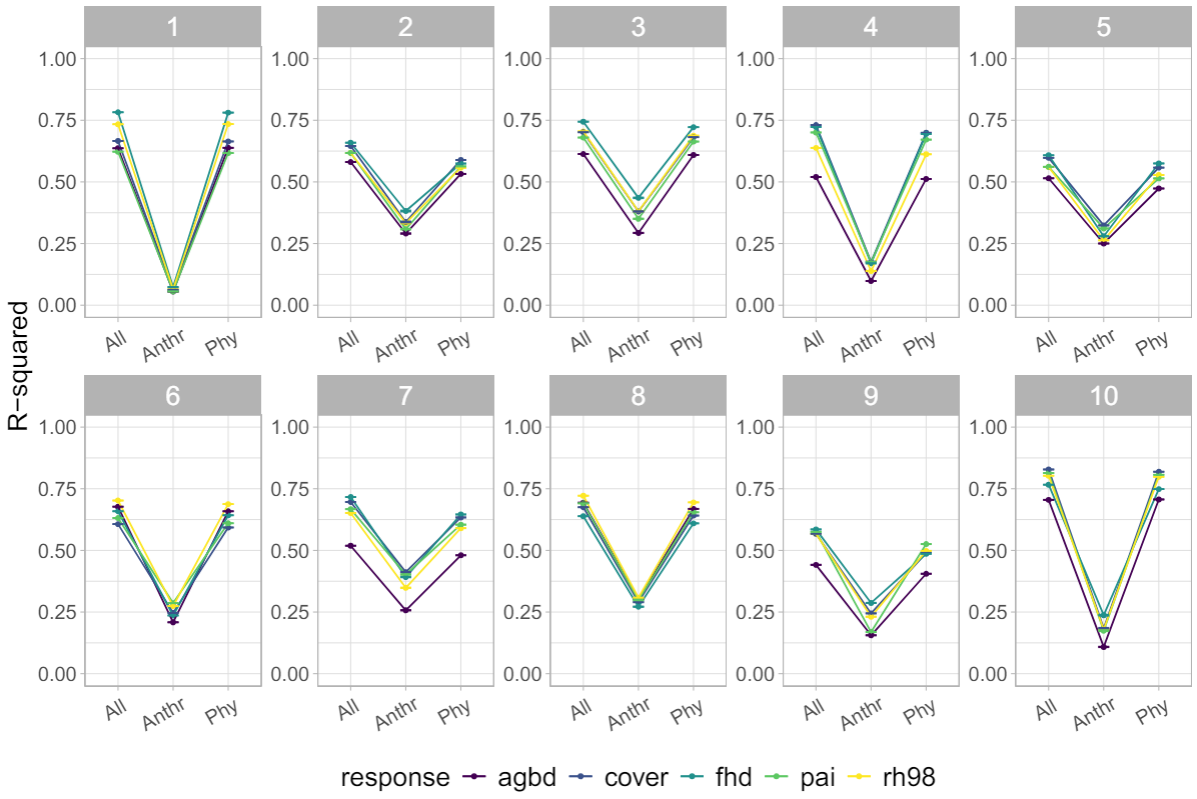

Figure 3. R-squared from the three main permutation scenarios in 10 sites. All means no permutation. Anthr means only anthropogenic variables were in the model and physical variables were permuted. Phy means only physical variables were in the model and anthropogenic variables were permuted.

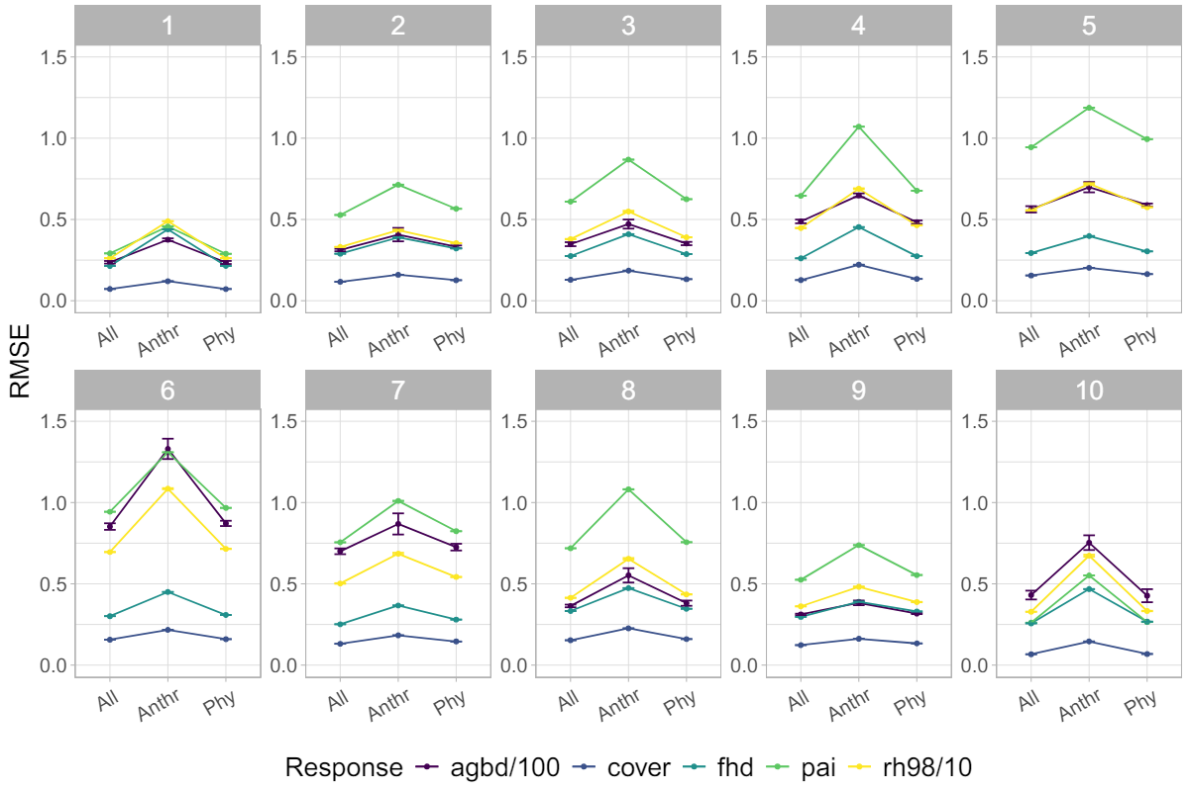

Figure 4. RMSE from the three main permutation scenarios in 10 sites. All means no permutation. Anthr means only anthropogenic variables were in the model and physical variables were permuted. Phy means only physical variables were in the model and anthropogenic variables were permuted.

3.2 The correlation between anthropogenic and physical variables

We found anthropogenic variables were redundant to the physical variables (e.g., Figure 5). In 4 of the 10 sites (site #3, site #4, site #6, site #7), at least one anthropogenic variable and one physical variable had an absolute value of the correlation coefficient that was greater than 0.5 (Figure 5, S3 – S11). For example, in site #3, the human modification index (Figure 5, the variable named "ghm") was correlated with many physical variables, such as elevation (Figure 5, the variable named "elev").

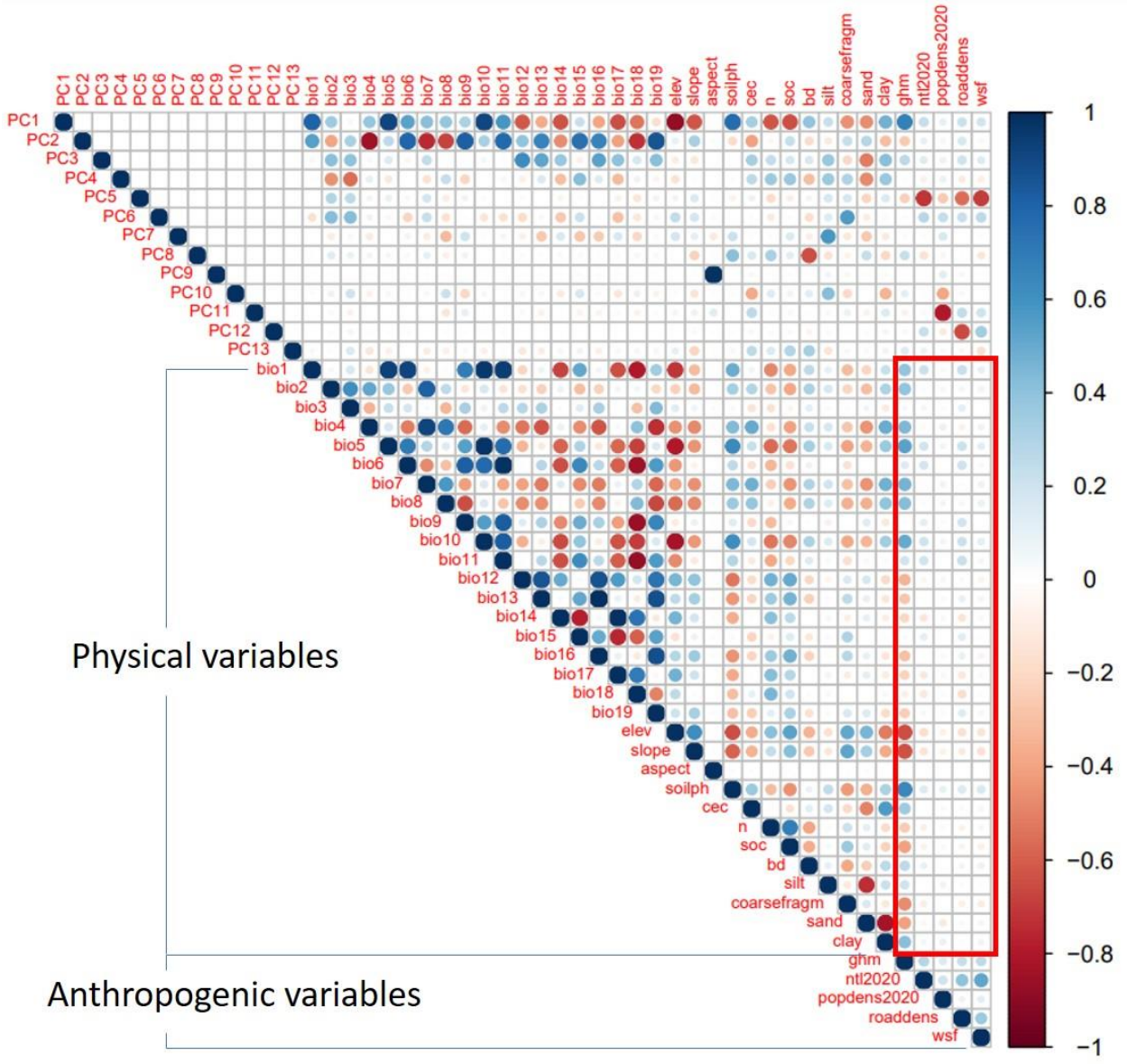

Figure 5. Correlation matrix of predictor variables in site #3 (Eastern Europe). The PCs are PCs that represent more than 90% of the variation in all predictor variables in the site.

3.3 The impact of the unbalanced number of anthropogenic and physical predictors

We found that the unbalanced number of anthropogenic variables and physical variables had an impact on the results because the information provided by the anthropogenic variables was not always informative for the model. The p-value was insignificant in 6 of the 10 sites

(Figure 6, site #1, site #2, site #3, site #6, site #8, site #10) with a significance level of 0.05. For example, in site #8 in the Brazilian Amazon, permutating anthropogenic variables had less impact to the model performance than permuting a random selection of five variables; while in site #7 in the southwestern Amazon, permuting anthropogenic variables led to a smaller R-squared value than those from permuting a random selection of five variables.

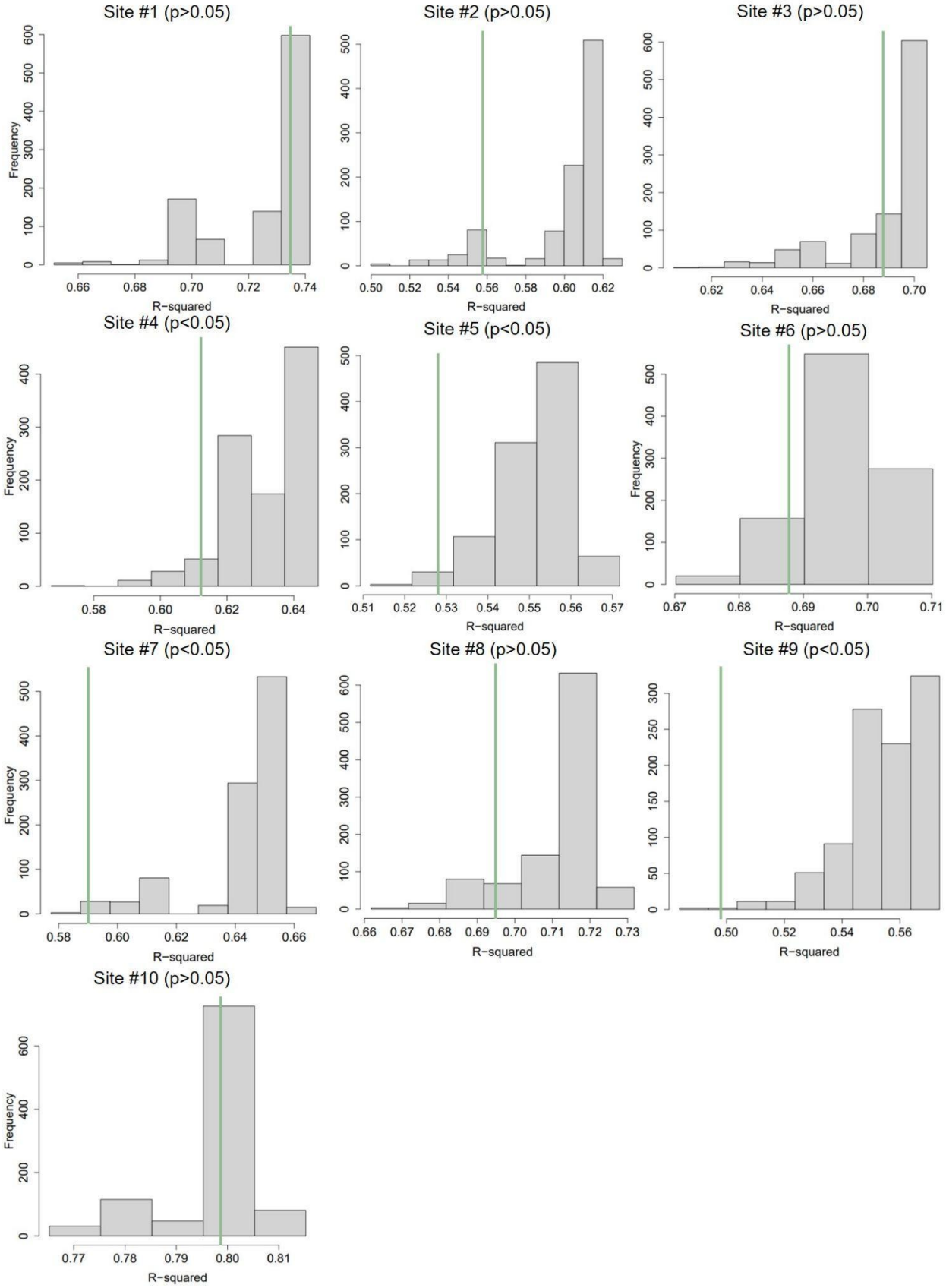
Site #1 (p>0.05)
Site #2 (p>0.05)
Site #3 (p>0.05)
Site #4 (p<0.05)
Site #5 (p<0.05)
Site #6 (p>0.05)
Site #7 (p<0.05)
Site #8 (p>0.05)
Site #9 (p<0.05)
Site #10 (p>0.05)
Frequency
R-squared

Figure 6. R-squared distribution from 1000 repetitions of permuting a random selection of five variables. The bin width was 0.01. The green vertical line is the R-squared when we permuted anthropogenic variables. The response variable was canopy height (RH98).

4. Discussion

Anthropogenic variables explained a certain amount of variability in the ecosystem structure, but they did not provide additional explanatory power to the model with physical variables (Figure 3, 4). However, this does not mean human impacts were less important than the physical environment due to two reasons examined in this study.

First, we found that in 4 of the 10 sites, anthropogenic variables were redundant to the physical variables (Figure 5, S3 – S11). The correlation between anthropogenic variables and physical variables made the anthropogenic information redundant to physical variables. This is why adding anthropogenic variables to the model with physical variables did not increase the R-squared in some sites (e.g., site #3 in Figure 3). Previous studies that used machine learning models or R-squared explained by the predictors to rank the importance of the predictors seldom check multicollinearity in the predictor variables (Zellweger et al., 2016; Wang et al., 2018; Luo et al., 2024), which may have an influence on the rank of the predictor variables.

Second, we found that the unbalanced number of anthropogenic and physical variables had an influence on the permutation analysis (Figure 6). Permuting a random selection of five variables could result in more decrease in R-squared than permuting anthropogenic variables. The redundancy in the predictor variables is probably the reason why there was not much variation in the R-squared when adding anthropogenic variables to the model with physical variables. Comparing site #7 to site #8, we found that human impacts had more explanatory power to the variability in ecosystem structure in site #7, which is supposed to be an intact forest,

than in site #8, which is known to have deforestation due to reasons like cattle ranching or soybean cultivation (Nepstad et al., 2009; Carrero et al., 2020). This makes sense because in site #8 (the Brazilian Amazon) the p-value was greater than 0.5, while in site #7 (southwest Amazon), the p-value was smaller than 0.5. In other words, permutating anthropogenic variables had more impact on the model than permuting a random selection of five variables in site #7, while in site #8 the impact was less. This is why anthropogenic variables explained around 25% of the variation in ecosystem structure, but when adding anthropogenic variables to the model, the R-squared was similar to the R-squared of the model with only physical variables (Figure 3, 4, from Phy to All, site #8).

The impact of the unbalanced number of predictor variables was also reflected in the permutation analyses with PCs (Figure S2). When using the same number of anthropogenic variables and physical variables, most of the sites (except site #1, site #10) exhibited more difference in R-squared when adding anthropogenic variables to the model with physical variables (Figure S2, from Anthr to None).

Permutation analyses with copies of predictor variables show that the model was using the information in the predictor variables in a more complicated way than we thought (Figure S1) because when permuting one copy of the anthropogenic variables or physical variables, the R-squared also decreased.

5. Conclusions

Although human impacts explain a certain amount of the variability of ecosystem structure depending on which structure metric was used as the response variable, we found no evidence of human impacts adding notably more explanatory power to the spatial variability of ecosystem structure. This is not necessarily due to the real importance of human activities to

ecosystem structure for two reasons: (1) the datasets that represent human impacts could be predicted by the physical environment; (2) there were more datasets about the physical environment than those that represent human impacts, which made the human impacts comparatively less informative for the variability in ecosystem structure.

Our study tested an assumption that was not tested by a recent study that stated human impacts were less important than climate (Li et al., 2023). Results from our study show that more examinations are needed before disentangling human impacts and the influence of the physical environment due to the two above-mentioned reasons, and more considerations are needed when using machine learning models for advancing understanding compared to only using those models for prediction.

Acknowledgment

Gridded GEDI data was produced by Patrick Burns, Chris Hakkenberg, and Scott Goetz. This research was conducted using computational resources and services at the Center for Computation and Visualization at Brown University. We thank Matthew Harrison, Stephen Porder, David Laidlaw, James Tompkin, and Ziang Liu for their advice on the analysis.

References

Akturk, E., Popescu, S.C., Malambo, L., 2023. ICESat-2 for Canopy Cover Estimation at Large-Scale on a Cloud-Based Platform. Sensors 23, 3394. https://doi.org/10.3390/s23073394

Asner, G.P., Flint Hughes, R., Varga, T.A., Knapp, D.E., Kennedy-Bowdoin, T., 2009. Environmental and Biotic Controls over Aboveground Biomass Throughout a Tropical Rain Forest. Ecosystems 12, 261–278. https://doi.org/10.1007/s10021-008-9221-5

Béland, M., Baldocchi, D.D., 2021. Vertical structure heterogeneity in broadleaf forests: Effects

on light interception and canopy photosynthesis. Agric. For. Meteorol. 307, 108525. https://doi.org/10.1016/j.agrformet.2021.108525

Brandt, M., Rasmussen, K., Peñuelas, J., Tian, F., Schurgers, G., Verger, A., Mertz, O., Palmer, J.R.B., Fensholt, R., 2017. Human population growth offsets climate-driven increase in woody vegetation in sub-Saharan Africa. Nat. Ecol. Evol. 1, 1–6. https://doi.org/10.1038/s41559-017-0081

Brandt, M., Tucker, C.J., Kariryaa, A., Rasmussen, K., Abel, C., Small, J., Chave, J., Rasmussen, L.V., Hiernaux, P., Diouf, A.A., Kergoat, L., Mertz, O., Igel, C., Gieseke, F., Schöning, J., Li, S., Melocik, K., Meyer, J., Sinno, S., Romero, E., Glennie, E., Montagu, A., Dendoncker, M., Fensholt, R., 2020. An unexpectedly large count of trees in the West African Sahara and Sahel. Nature 587, 78–82. https://doi.org/10.1038/s41586-020-2824-5

Burns, P., Hakkenberg, C., Goetz, SJ., 2024. Gridded GEDI Vegetation Structure Metrics and Biomass Density at Multiple Resolutions. ORNL DAAC, Oak Ridge, Tennessee, USA

Cai, X., Wu, Z., Cheng, J., 2013. Using kernel density estimation to assess the spatial pattern of road density and its impact on landscape fragmentation. Int. J. Geogr. Inf. Sci. 27, 222–230. https://doi.org/10.1080/13658816.2012.663918

Carrasco, L., Giam, X., Papeş, M., Sheldon, K.S., 2019. Metrics of Lidar-Derived 3D Vegetation Structure Reveal Contrasting Effects of Horizontal and Vertical Forest Heterogeneity on Bird Species Richness. Remote Sens. 11, 743. https://doi.org/10.3390/rs11070743

Carrero, G.C., Fearnside, P.M., do Valle, D.R., de Souza Alves, C., 2020. Deforestation Trajectories on a Development Frontier in the Brazilian Amazon: 35 Years of Settlement Colonization, Policy and Economic Shifts, and Land Accumulation. Environ. Manage. 66, 966–984. https://doi.org/10.1007/s00267-020-01354-w

Center for International Earth Science Information Network - CIESIN - Columbia University, 2018. UN WPP-Adjusted Population Density, v4.11: Gridded Population of the World (GPW), v4 | SEDAC.

Chen, C., Park, T., Wang, X., Piao, S., Xu, B., Chaturvedi, R.K., Fuchs, R., Brovkin, V., Ciais, P., Fensholt, R., Tømmervik, H., Bala, G., Zhu, Z., Nemani, R.R., Myneni, R.B., 2019. China and India lead in greening of the world through land-use management. Nat. Sustain. 2, 122–129. https://doi.org/10.1038/s41893-019-0220-7

Clark, D.B., Clark, D.A., 2000. Landscape-scale variation in forest structure and biomass in a tropical rain forest. For. Ecol. Manag. 137, 185–198. https://doi.org/10.1016/S0378-1127(99)00327-8

Díaz, I.A., Armesto, J.J., Reid, S., Sieving, K.E., Willson, M.F., 2005. Linking forest structure and composition: avian diversity in successional forests of Chiloé Island, Chile. Biol. Conserv. 123, 91–101. https://doi.org/10.1016/j.biocon.2004.10.011

Dubayah, R., Armston, J., Healey, S.P., Bruening, J.M., Patterson, P.L., Kellner, J.R., Duncanson, L., Saarela, S., Ståhl, G., Yang, Z., Tang, H., Blair, J.B., Fatoyinbo, L., Goetz, S., Hancock, S., Hansen, M., Hofton, M., Hurtt, G., Luthcke, S., 2022. GEDI launches a new era of biomass inference from space. Environ. Res. Lett. 17, 095001. https://doi.org/10.1088/1748-9326/ac8694

Dubayah, R., Blair, J.B., Goetz, S., Fatoyinbo, L., Hansen, M., Healey, S., Hofton, M., Hurtt, G., Kellner, J., Luthcke, S., Armston, J., Tang, H., Duncanson, L., Hancock, S., Jantz, P., Marselis, S., Patterson, P.L., Qi, W., Silva, C., 2020. The Global Ecosystem Dynamics Investigation: High-resolution laser ranging of the Earth's forests and topography. Sci. Remote Sens. 1, 100002. https://doi.org/10.1016/j.srs.2020.100002

Dubayah, R., Tang, H., Armston, J., Luthcke, S., Hofton, M., Blair, J., 2021. GEDI L2B Canopy Cover and Vertical Profile Metrics Data Global Footprint Level V002. https://doi.org/10.5067/GEDI/GEDI02_B.002

Ellis, E.C., 2011. Anthropogenic transformation of the terrestrial biosphere. Philos. Trans. R. Soc. Math. Phys. Eng. Sci. 369, 1010–1035. https://doi.org/10.1098/rsta.2010.0331

Elvidge, C.D., Zhizhin, M., Ghosh, T., Hsu, F.-C., Taneja, J., 2021. Annual Time Series of Global VIIRS Nighttime Lights Derived from Monthly Averages: 2012 to 2019. Remote Sens. 13. https://doi.org/10.3390/rs13050922

Farr, T.G., Kobrick, M., 2000. Shuttle radar topography mission produces a wealth of data. Eos Trans. Am. Geophys. Union 81, 583–585. https://doi.org/10.1029/EO081i048p00583

Fick, S.E., Hijmans, R.J., 2017. WorldClim 2: new 1-km spatial resolution climate surfaces for global land areas. Int. J. Climatol. 37, 4302–4315. https://doi.org/10.1002/joc.5086

Foley, J.A., DeFries, R., Asner, G.P., Barford, C., Bonan, G., Carpenter, S.R., Chapin, F.S., Coe, M.T., Daily, G.C., Gibbs, H.K., Helkowski, J.H., Holloway, T., Howard, E.A., Kucharik, C.J., Monfreda, C., Patz, J.A., Prentice, I.C., Ramankutty, N., Snyder, P.K., 2005. Global Consequences of Land Use. Science 309, 570–574. https://doi.org/10.1126/science.1111772

Gaffney, O., Steffen, W., 2017. The Anthropocene equation. Anthr. Rev. 4, 53–61. https://doi.org/10.1177/2053019616688022

Gils, H.V., Wijngaarden, W.V., 1984. Vegetation structure in reconnaissance and semi-detailed vegetation surveys. ITC J. 213–218.

Graetz, R.D., 1990. Remote Sensing of Terrestrial Ecosystem Structure: An Ecologist's Pragmatic View, in: Hobbs, R.J., Mooney, H.A. (Eds.), Remote Sensing of Biosphere

Functioning, Ecological Studies. Springer, New York, NY, pp. 5–30. https://doi.org/10.1007/978-1-4612-3302-2_2

Hengl, T., Jesus, J.M. de, Heuvelink, G.B.M., Gonzalez, M.R., Kilibarda, M., Blagotić, A., Shangguan, W., Wright, M.N., Geng, X., Bauer-Marschallinger, B., Guevara, M.A., Vargas, R., MacMillan, R.A., Batjes, N.H., Leenaars, J.G.B., Ribeiro, E., Wheeler, I., Mantel, S., Kempen, B., 2017. SoilGrids250m: Global gridded soil information based on machine learning. PLOS ONE 12, e0169748. https://doi.org/10.1371/journal.pone.0169748

Higgins, M.A., Asner, G.P., Anderson, C.B., Martin, R.E., Knapp, D.E., Tupayachi, R., Perez, E., Elespuru, N., Alonso, A., 2015. Regional-Scale Drivers of Forest Structure and Function in Northwestern Amazonia. PLOS ONE 10, e0119887. https://doi.org/10.1371/journal.pone.0119887

Holdridge, L.R., 1947. Determination of World Plant Formations From Simple Climatic Data. Science. https://doi.org/10.1126/science.105.2727.367

Kennedy, C.M., Oakleaf, J.R., Theobald, D.M., Baruch-Mordo, S., Kiesecker, J., 2019. Managing the middle: A shift in conservation priorities based on the global human modification gradient. Glob. Change Biol. 25, 811–826. https://doi.org/10.1111/gcb.14549

Lang, N., Kalischek, N., Armston, J., Schindler, K., Dubayah, R., Wegner, J.D., 2022. Global canopy height regression and uncertainty estimation from GEDI LIDAR waveforms with deep ensembles. Remote Sens. Environ. 268, 112760. https://doi.org/10.1016/j.rse.2021.112760

Le Toan, T., Quegan, S., Davidson, M.W.J., Balzter, H., Paillou, P., Papathanassiou, K.,

Plummer, S., Rocca, F., Saatchi, S., Shugart, H., Ulander, L., 2011. The BIOMASS mission: Mapping global forest biomass to better understand the terrestrial carbon cycle. Remote Sens. Environ., DESDynI VEG-3D Special Issue 115, 2850–2860. https://doi.org/10.1016/j.rse.2011.03.020

Lewis, S.L., Maslin, M.A., 2015. Defining the Anthropocene. Nature 519, 171–180. https://doi.org/10.1038/nature14258

Li, W., Guo, W.-Y., Pasgaard, M., Niu, Z., Wang, L., Chen, F., Qin, Y., Svenning, J.-C., 2023. Human fingerprint on structural density of forests globally. Nat. Sustain. 6, 368–379. https://doi.org/10.1038/s41893-022-01020-5

Liu, S., Brandt, M., Nord-Larsen, T., Chave, J., Reiner, F., Lang, N., Tong, X., Ciais, P., Igel, C., Pascual, A., Guerra-Hernandez, J., Li, S., Mugabowindekwe, M., Saatchi, S., Yue, Y., Chen, Z., Fensholt, R., 2023. The overlooked contribution of trees outside forests to tree cover and woody biomass across Europe. Sci. Adv. 9, eadh4097. https://doi.org/10.1126/sciadv.adh4097

Luo, K., Wang, X., de Jong, M., Flannigan, M., 2024. Drought triggers and sustains overnight fires in North America. Nature 627, 321–327. https://doi.org/10.1038/s41586-024-07028-5

Ma, L., Hurtt, G., Tang, H., Lamb, R., Lister, A., Chini, L., Dubayah, R., Armston, J., Campbell, E., Duncanson, L., Healey, S., O'Neil-Dunne, J., Ott, L., Poulter, B., Shen, Q., 2023. Spatial heterogeneity of global forest aboveground carbon stocks and fluxes constrained by spaceborne lidar data and mechanistic modeling. Glob. Change Biol. 29, 3378–3394. https://doi.org/10.1111/gcb.16682

Ma, L., Yu, D., Chen, Y., Feng, K., Tang, H., Sumnall, M.J., Zheng, G., 2024. Quantifying the

Plant Area Index of Overstory and Understory Vegetation on Sloped Terrain Using Single-Station Terrestrial Laser Scanner. IEEE Trans. Geosci. Remote Sens. 62, 1–19. https://doi.org/10.1109/TGRS.2024.3395584

MacArthur, R.H., MacArthur, J.W., 1961. On Bird Species Diversity. Ecology 42, 594–598. https://doi.org/10.2307/1932254

Marconcini, M., Marconcini, A.M.-, Esch, T., Gorelick, N., 2021. Understanding Current Trends in Global Urbanisation - The World Settlement Footprint Suite.

Matsuo, T., Martínez-Ramos, M., Bongers, F., van der Sande, M.T., Poorter, L., 2021. Forest structure drives changes in light heterogeneity during tropical secondary forest succession. J. Ecol. 109, 2871–2884. https://doi.org/10.1111/1365-2745.13680

Meijer, J.R., Huijbregts, M.A.J., Schotten, K., Schipper, A.M., 2018. Global patterns of current and future road infrastructure. Environ. Res. Lett. 13.

Meyer, L., Diniz-Filho, J.A.F., Lohmann, L.G., Hortal, J., Barreto, E., Rangel, T., Kissling, W.D., 2020. Canopy height explains species richness in the largest clade of Neotropical lianas. Glob. Ecol. Biogeogr. 29, 26–37. https://doi.org/10.1111/geb.13004

Migliavacca, M., Musavi, T., Mahecha, M.D., Nelson, J.A., Knauer, J., Baldocchi, D.D., Perez-Priego, O., Christiansen, R., Peters, J., Anderson, K., Bahn, M., Black, T.A., Blanken, P.D., Bonal, D., Buchmann, N., Caldararu, S., Carrara, A., Carvalhais, N., Cescatti, A., Chen, J., Cleverly, J., Cremonese, E., Desai, A.R., El-Madany, T.S., Farella, M.M., Fernández-Martínez, M., Filippa, G., Forkel, M., Galvagno, M., Gomarasca, U., Gough, C.M., Göckede, M., Ibrom, A., Ikawa, H., Janssens, I.A., Jung, M., Kattge, J., Keenan, T.F., Knohl, A., Kobayashi, H., Kraemer, G., Law, B.E., Liddell, M.J., Ma, X., Mammarella, I., Martini, D., Macfarlane, C., Matteucci, G., Montagnani, L., Pabon-

Moreno, D.E., Panigada, C., Papale, D., Pendall, E., Penuelas, J., Phillips, R.P., Reich, P.B., Rossini, M., Rotenberg, E., Scott, R.L., Stahl, C., Weber, U., Wohlfahrt, G., Wolf, S., Wright, I.J., Yakir, D., Zaehle, S., Reichstein, M., 2021. The three major axes of terrestrial ecosystem function. Nature 598, 468–472. https://doi.org/10.1038/s41586-021-03939-9

Nepstad, D., Soares-Filho, B.S., Merry, F., Lima, A., Moutinho, P., Carter, J., Bowman, M., Cattaneo, A., Rodrigues, H., Schwartzman, S., McGrath, D.G., Stickler, C.M., Lubowski, R., Piris-Cabezas, P., Rivero, S., Alencar, A., Almeida, O., Stella, O., 2009. The End of Deforestation in the Brazilian Amazon. Science 326, 1350–1351. https://doi.org/10.1126/science.1182108

Novella-Fernandez, R., Juste, J., Ibañez, C., Nogueras, J., Osborne, P.E., Razgour, O., 2022. The role of forest structure and composition in driving the distribution of bats in Mediterranean regions. Sci. Rep. 12, 3224. https://doi.org/10.1038/s41598-022-07229-w

Qin, Y., Xiao, X., Wigneron, J.-P., Ciais, P., Brandt, M., Fan, L., Li, X., Crowell, S., Wu, X., Doughty, R., Zhang, Y., Liu, F., Sitch, S., Moore, B., 2021. Carbon loss from forest degradation exceeds that from deforestation in the Brazilian Amazon. Nat. Clim. Change 11, 442–448. https://doi.org/10.1038/s41558-021-01026-5

Smith, A.P., 1973. Stratification of Temperature and Tropical Forests. Am. Nat. 107, 671–683. https://doi.org/10.1086/282866

Song, X.-P., Hansen, M.C., Stehman, S.V., Potapov, P.V., Tyukavina, A., Vermote, E.F., Townshend, J.R., 2018. Global land change 1982-2016. Nature 560, 639–643. https://doi.org/10.1038/s41586-018-0411-9

Spies, T.A., 1998. Forest structure: a key to the ecosystem. Northwest Sci. 72, 34–36.

Steffen, W., Crutzen, J., McNeill, J.R., 2007. The Anthropocene: are humans now overwhelming the great forces of Nature? Ambio 36, 614–621. https://doi.org/10.1579/0044-7447(2007)36[614:taahno]2.0.co;2

Tang, H., Armston, J., Hancock, S., Marselis, S., Goetz, S., Dubayah, R., 2019. Characterizing global forest canopy cover distribution using spaceborne lidar. Remote Sens. Environ. 231, 111262. https://doi.org/10.1016/j.rse.2019.111262

Wang, W., Ma, X., Moazzam Nizami, S., Tian, C., Guo, F., 2018. Anthropogenic and Biophysical Factors Associated with Vegetation Restoration in Changting, China. Forests 9, 306. https://doi.org/10.3390/f9060306

Zellweger, F., Baltensweiler, A., Ginzler, C., Roth, T., Braunisch, V., Bugmann, H., Bollmann, K., 2016. Environmental predictors of species richness in forest landscapes: abiotic factors versus vegetation structure. J. Biogeogr. 43, 1080–1090. https://doi.org/10.1111/jbi.12696

Zhao, M., Zhou, Y., Li, Xuecao, Cao, W., He, C., Yu, B., Li, Xi, Elvidge, C.D., Cheng, W., Zhou, C., 2019. Applications of Satellite Remote Sensing of Nighttime Light Observations: Advances, Challenges, and Perspectives. Remote Sens. 11, 1971. https://doi.org/10.3390/rs11171971

Supplementary materials

Table S1. Predictor and response variables

	Variable	Name in Figures 3 – 5, S1 – S11
Predictor variable	Annual mean temperature	bio1
	Mean diurnal range (mean of monthly max temp minus monthly min temp)	bio2
	Isothermality (bio2/bio7) (×100)	bio3
	Temperature seasonality (standard deviation ×100)	bio4
	Max temperature of warmest month	bio5
	Min temperature of coldest month	bio6
	Temperature annual range (bio5-bio6)	bio7
	Mean temperature of wettest quarter	bio8
	Mean temperature of driest quarter	bio9
	Mean temperature of warmest quarter	bio10
	Mean temperature of coldest quarter	bio11
	Annual precipitation	bio12

Precipitation of wettest month	bio13
Precipitation of driest month	bio14
Precipitation seasonality (coefficient of Variation)	bio15
Precipitation of wettest quarter	bio16
Precipitation of driest quarter	bio17
Precipitation of warmest quarter	bio18
Precipitation of coldest quarter	bio19
Elevation	elev
Slope	slope
Aspect	aspect
Soil pH	soilph
Cation exchange capacity	cec
Soil nitrogen content	n
Soil organic carbon	soc
Bulk density	bd
Silt content	silt
Coarse fragment content	coarsefragm

	Sand content	sand
	Clay content	clay
	Human modification index	ghm
	Nighttime light in 2020	ntl2020
	Population density in 2020	popdens2020
	Road density	roaddens
	Proportion of human built-ups	wsf
Response variable	Aboveground biomass density	agbd
	Fractional cover	cover
	Foliage height diversity	fhd
	Plant area index	pai
	Canopy height (RH98)	rh98

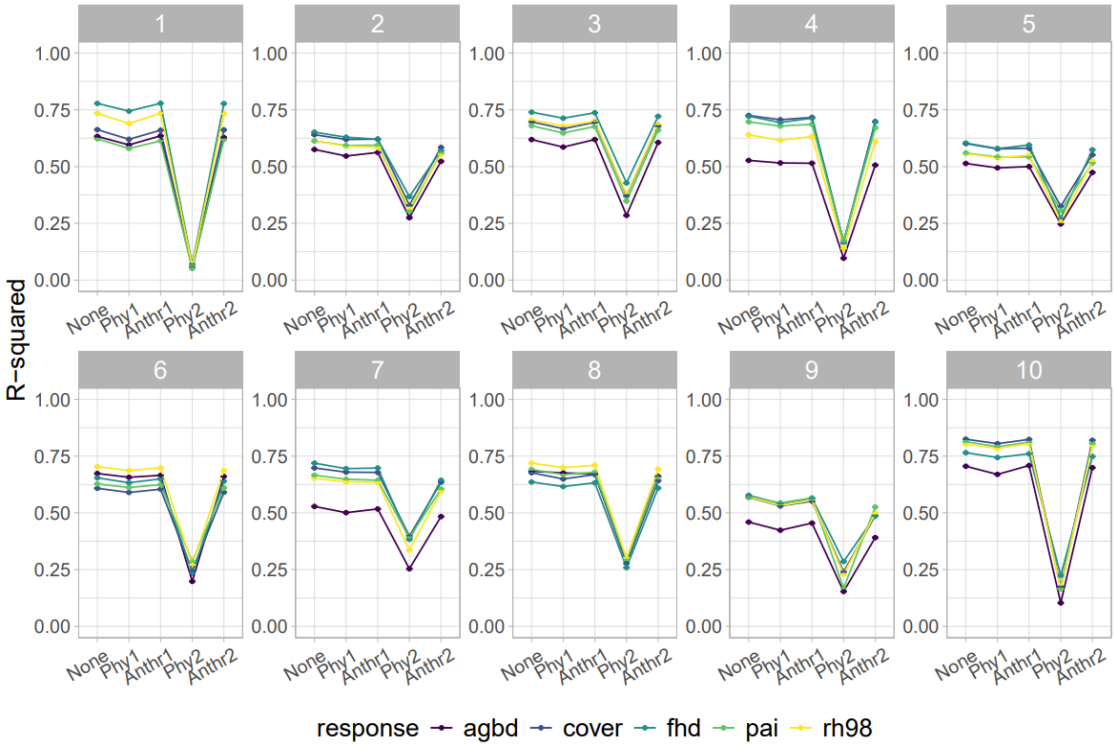

Figure S1. Permutation with two copies of each predictor variable. None: no permutation. Phy1: permute one copy of physical variables. Anthr1: permute one copy of anthropogenic variables. Phy2: permute two copies of physical variables. Anthr2: permute 2 copies of anthropogenic variables. Note that the Anthr and Phy here are different from those in Figure 3 and Figure 4.

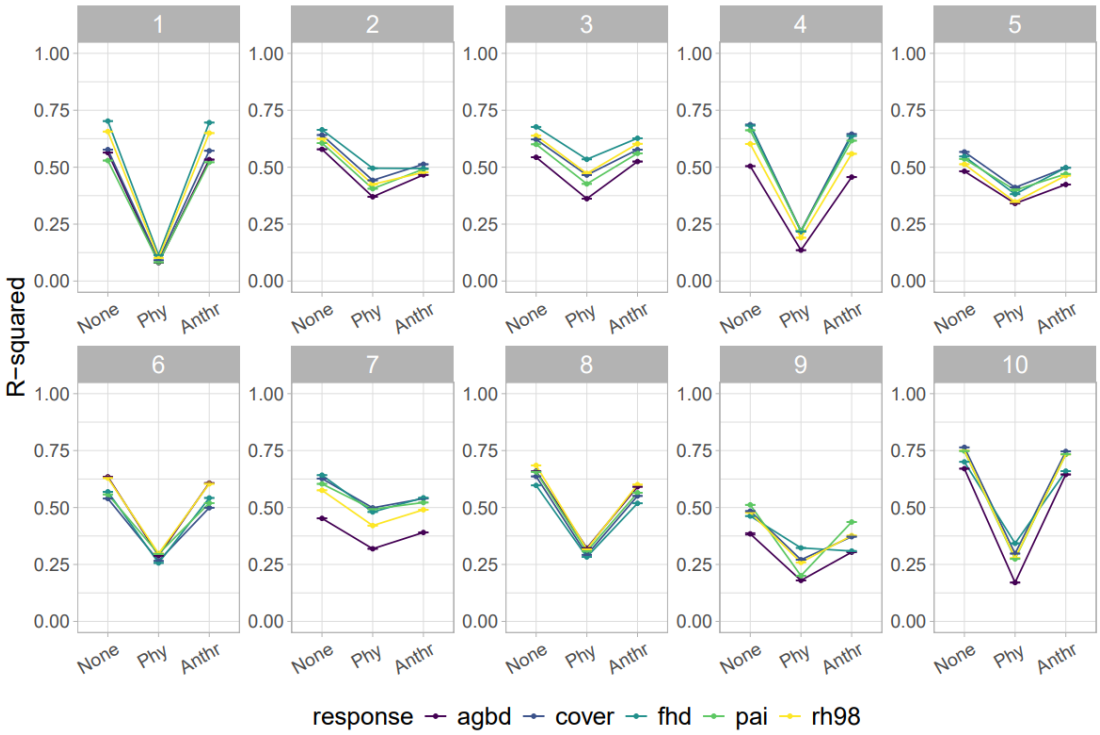

Figure S2. Permutation with PCs of anthropogenic variables and with PCs of physical variables. None: no permutation. Phy: permute the first four PCs of physical variables. Anthr: permute the first four PCs of anthropogenic variables. Note that the Anthr and Phy here are different from those in Figure 3 and Figure 4.

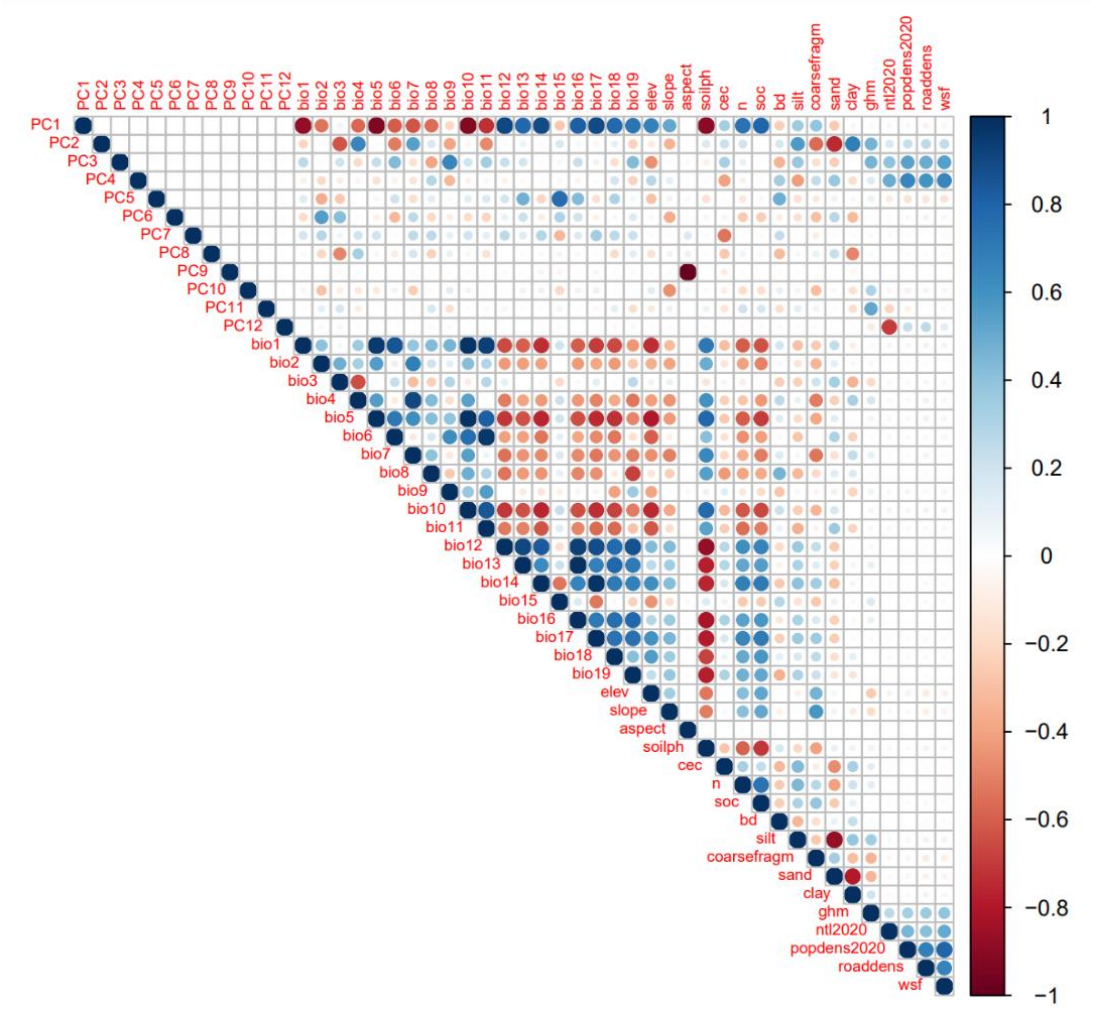

Figure S3. Correlation matrix of predictor variables in site #1 (US Rocky mountains). The PCs are PCs that represent more than 90% of the variation in all predictor variables.

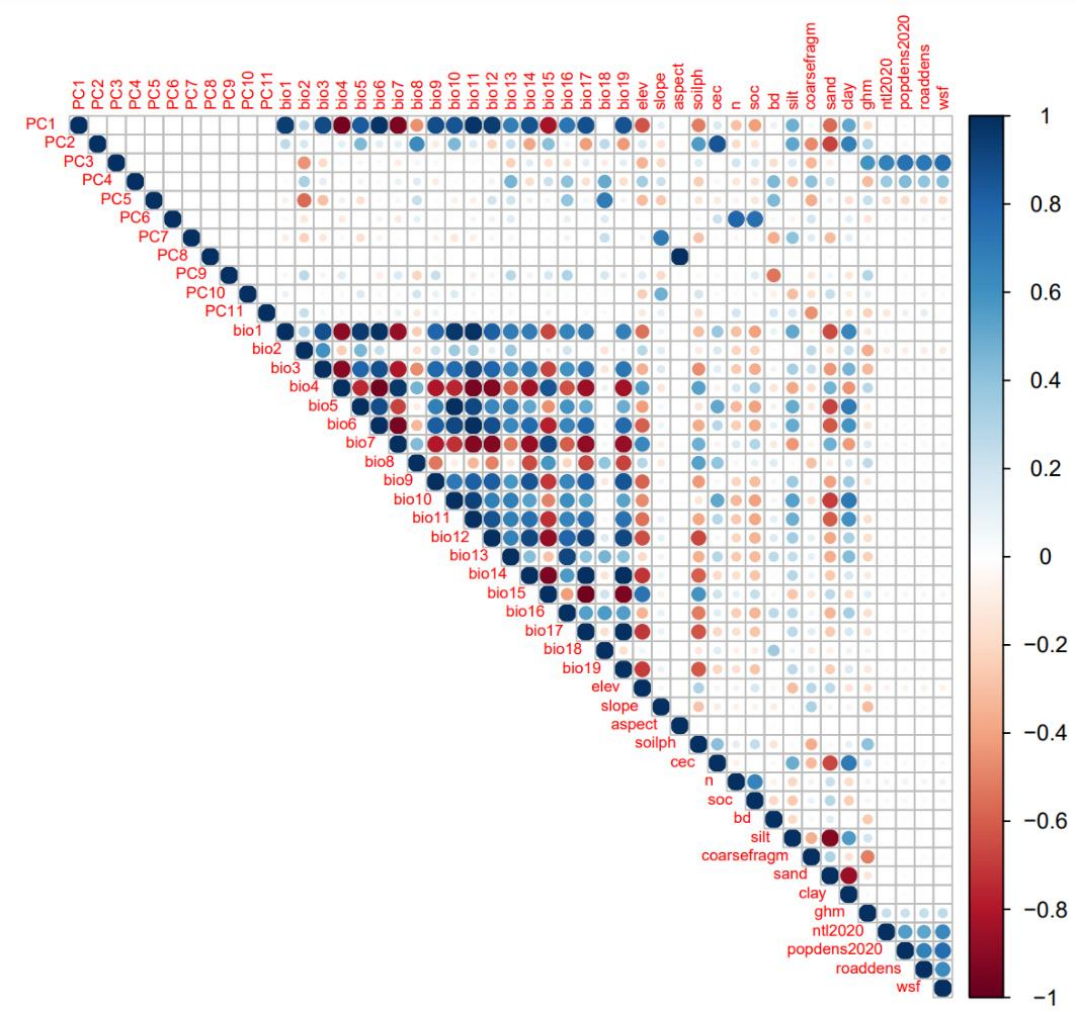

Figure S4. Correlation matrix of predictor variables in site #2 (Midwestern US). The PCs are PCs that represent more than 90% of the variation in all predictor variables.

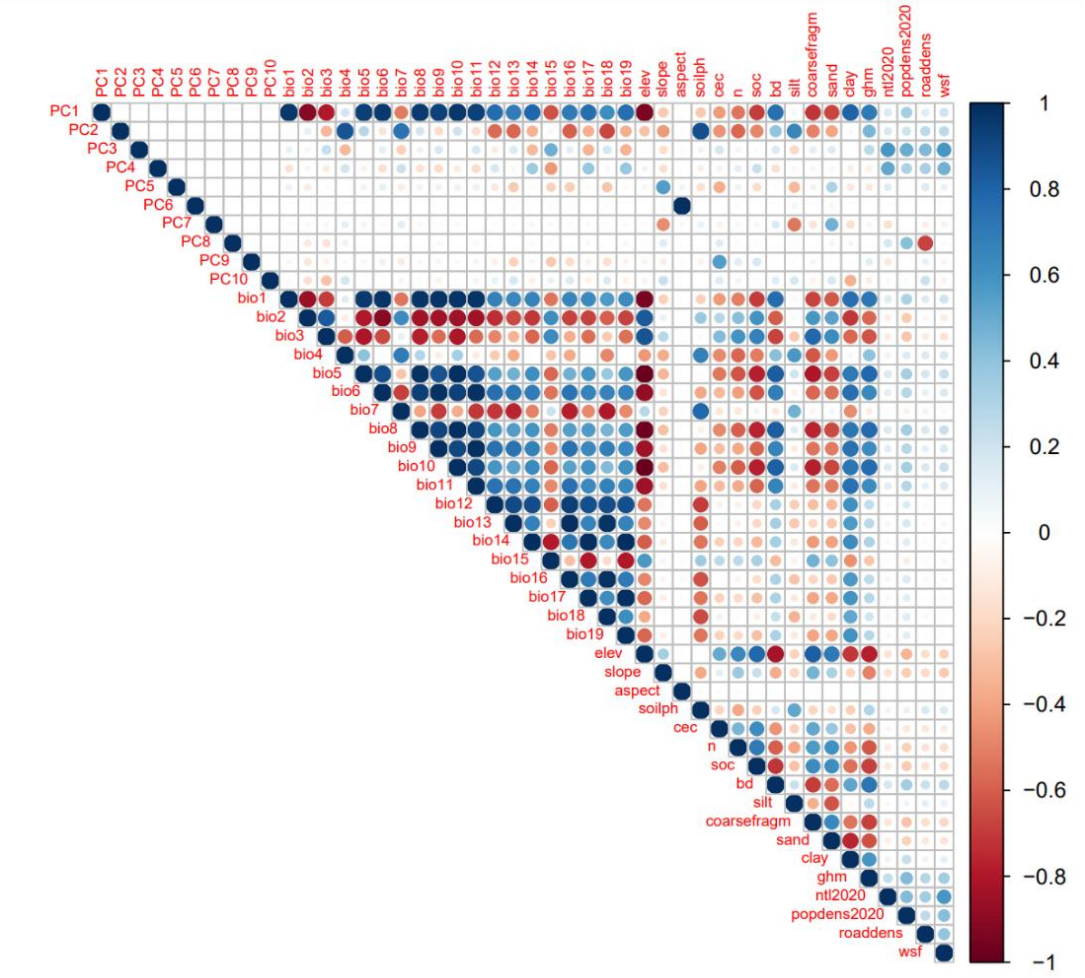

Figure S5. Correlation matrix of predictor variables in site #4 (Southwestern China). The PCs are PCs that represent more than 90% of the variation in all predictor variables.

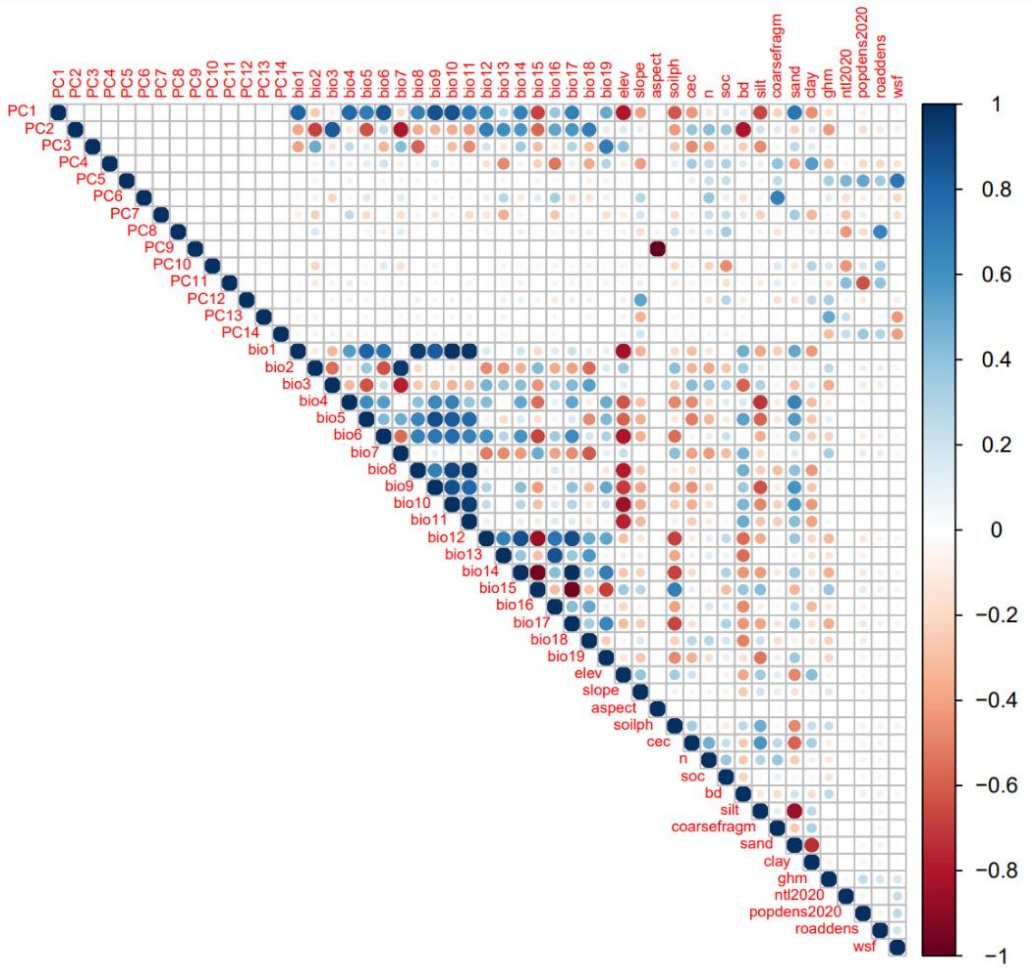

Figure S6. Correlation matrix of predictor variables in site #5 (DRC Congo basin). The PCs are PCs that represent more than 90% of the variation in all predictor variables.

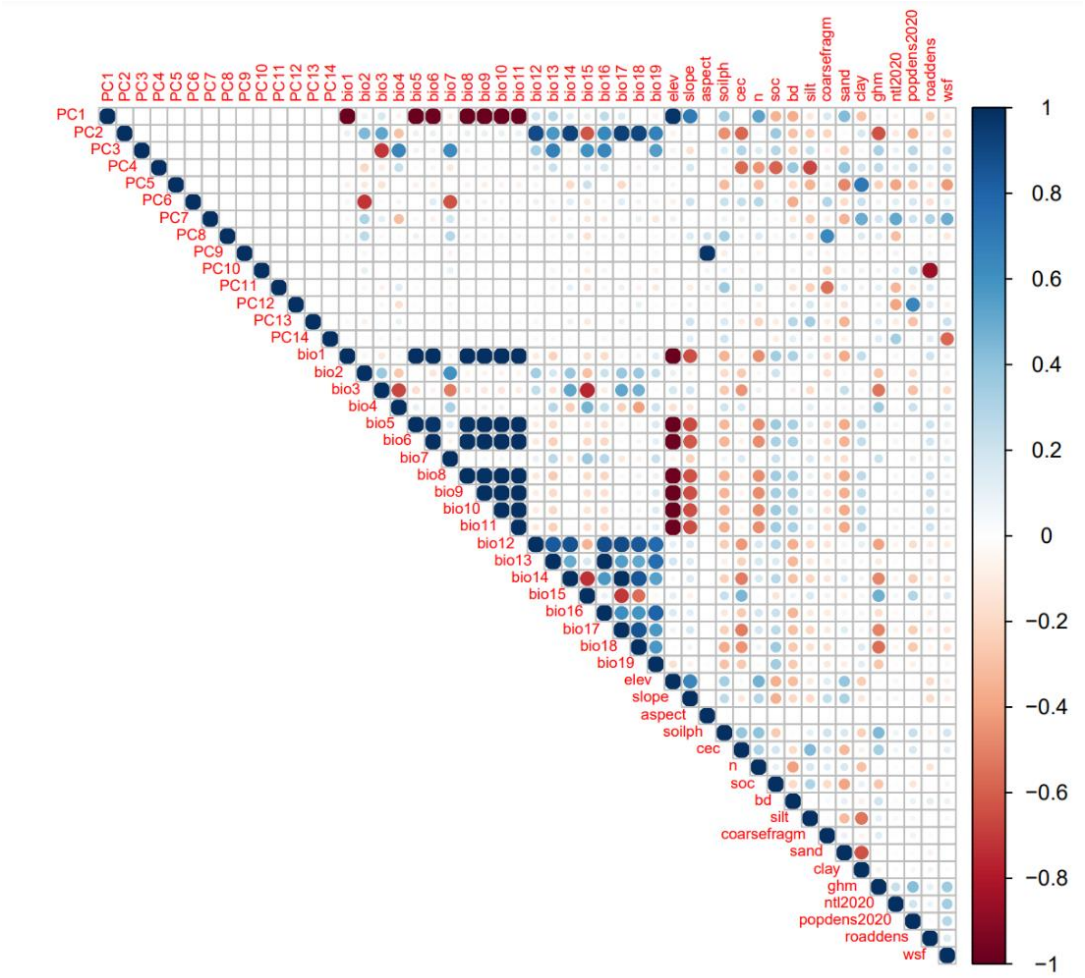

Figure S7. Correlation matrix of predictor variables in site #6 (Borneo). The PCs are PCs that represent more than 90% of the variation in all predictor variables.

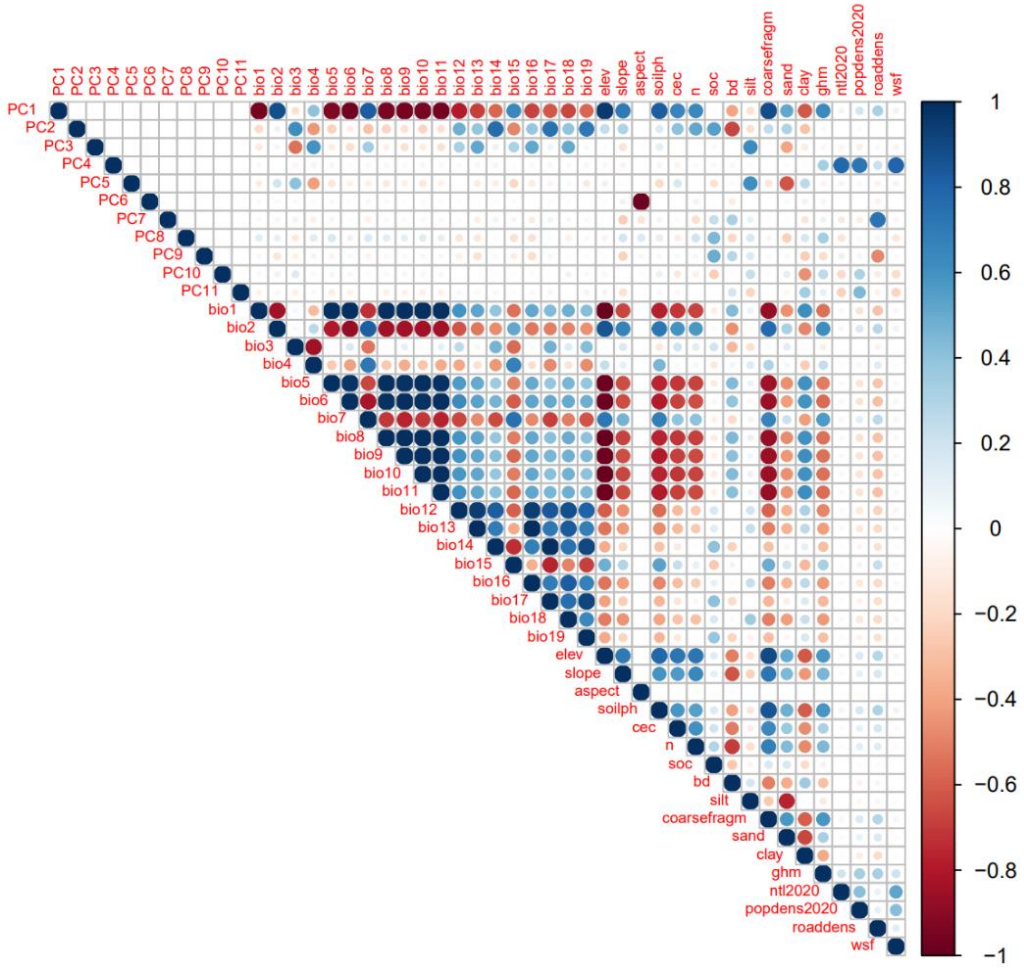

Figure S8. Correlation matrix of predictor variables in site #7 (Southwest Amazon). The PCs are PCs that represent more than 90% of the variation in all predictor variables.

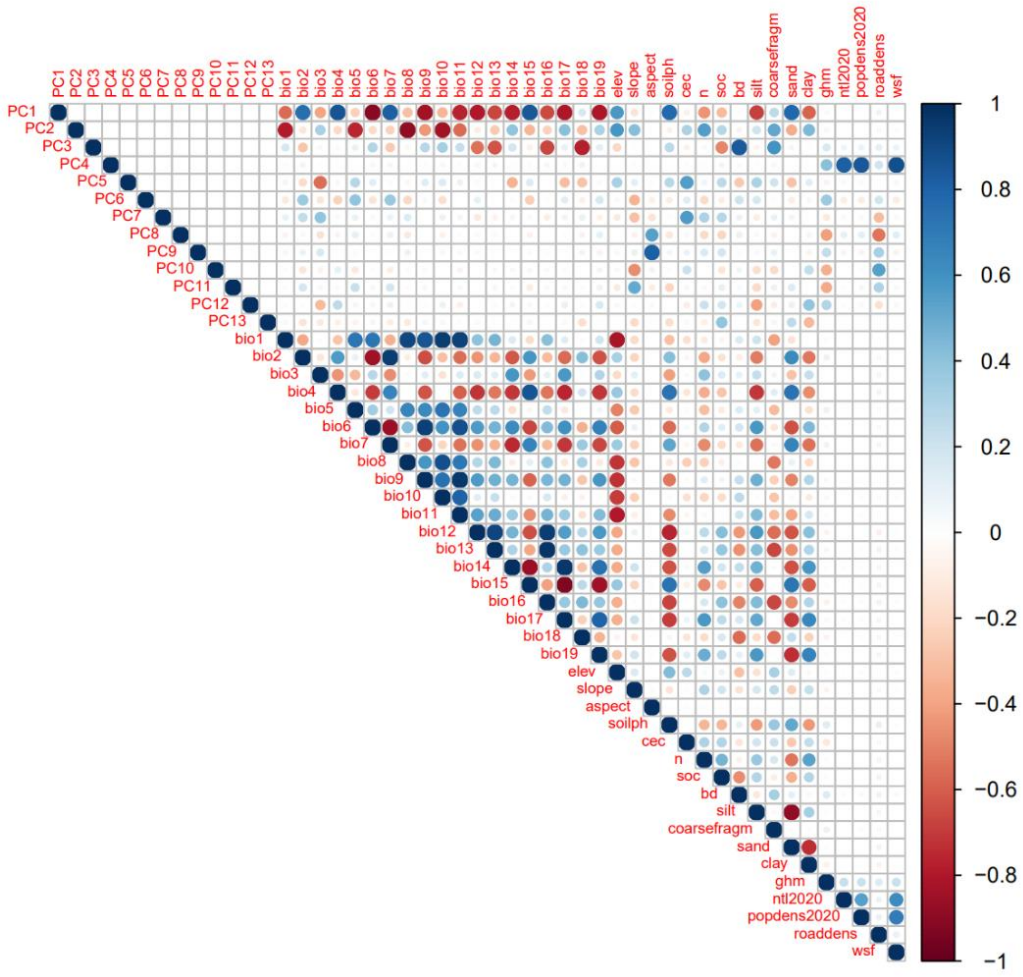

Figure S9. Correlation matrix of predictor variables in site #8 (Brazilian Amazon). The PCs are PCs that represent more than 90% of the variation in all predictor variables.

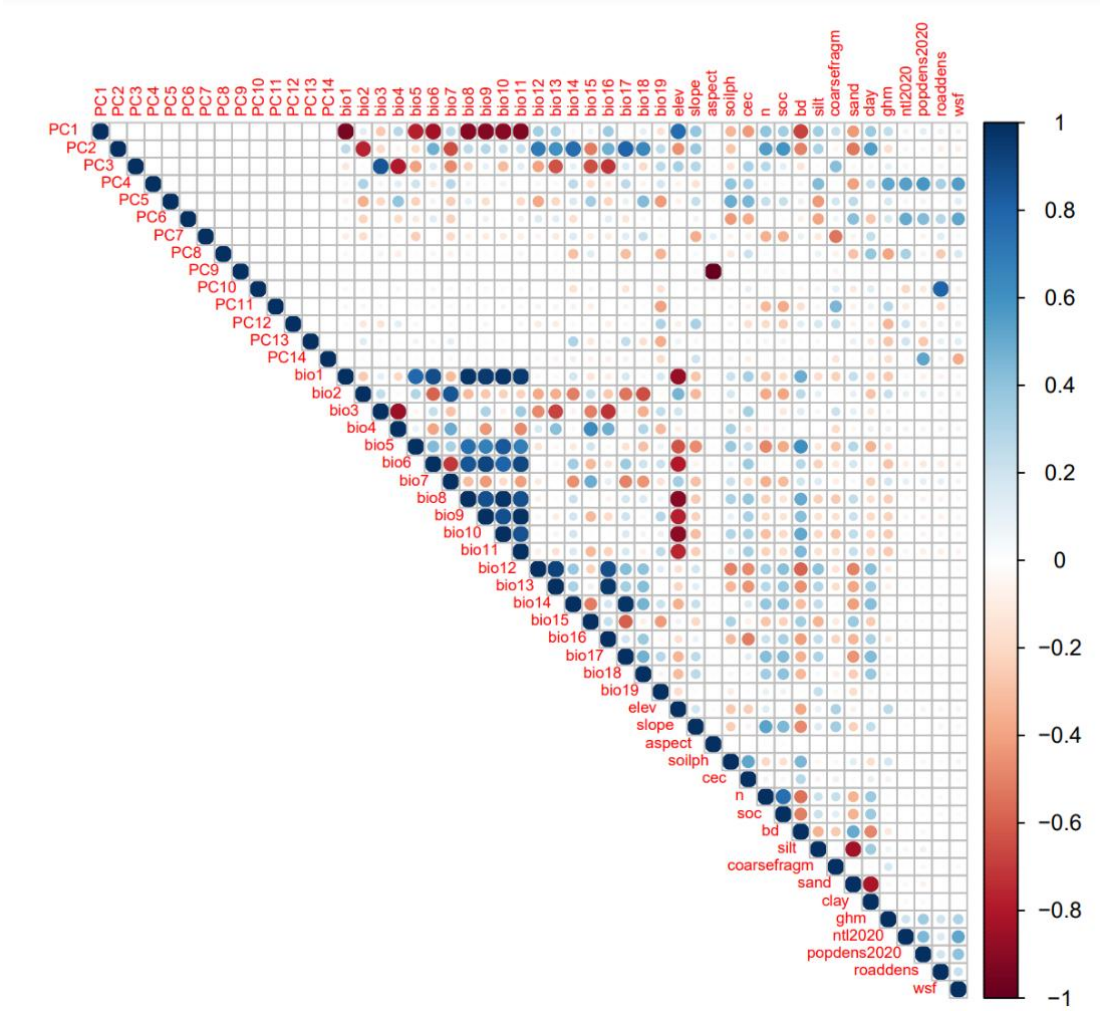

Figure S10. Correlation matrix of predictor variables in site #9 (African grasslands). The PCs are PCs that represent more than 90% of the variation in all predictor variables.

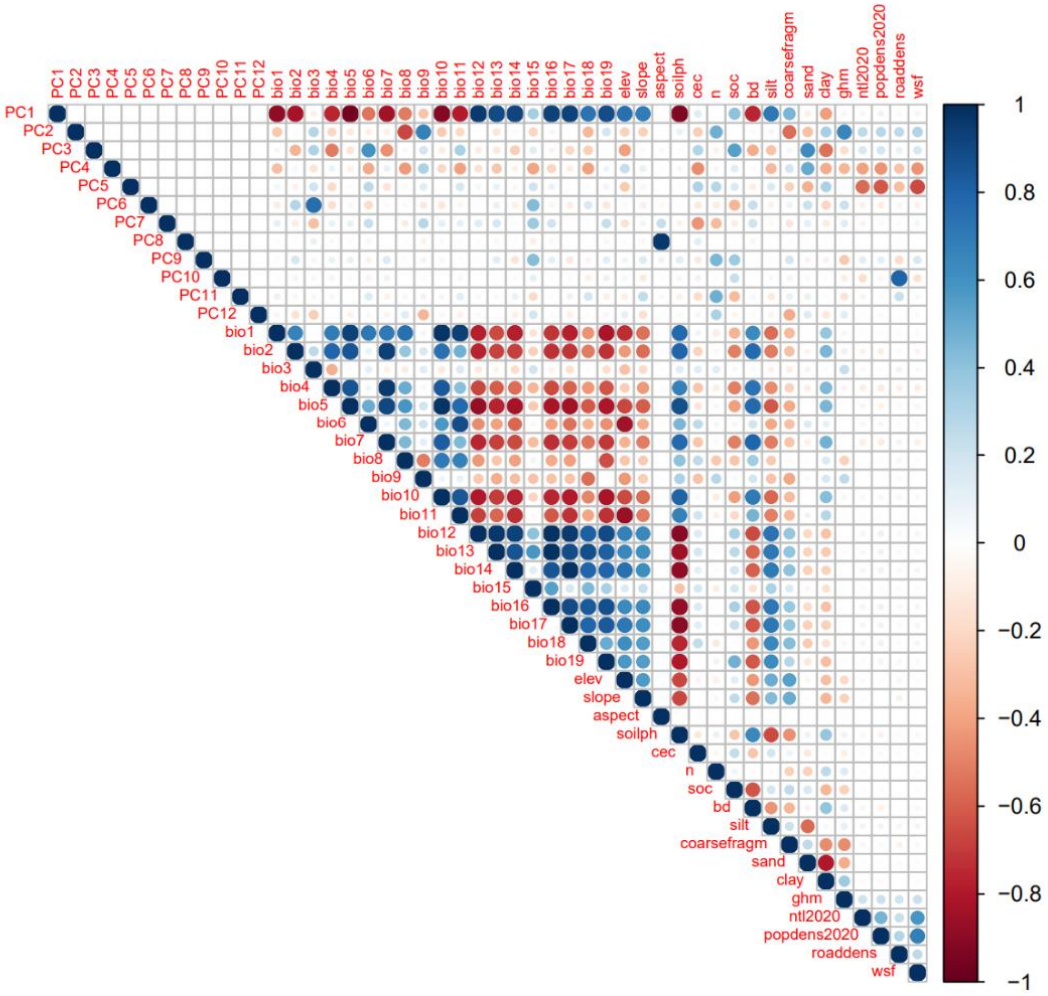

Figure S11. Correlation matrix of predictor variables in site #10 (Southeastern Australia). The PCs are PCs that represent more than 90% of the variation in all predictor variables.

CHAPTER 3

Evaluation of prediction strata in the GEDI04_A aboveground biomass density data product

Dafeng Zhang[1,2], Mona Khoshnevis[3], Matthew Harrison[3], Eugene Seo[1,2,3], Laura Duncanson[4], John Armston[4], James R. Kellner[1,2]

1. Department of Ecology, Evolution and Organismal Biology, Brown University, Providence, RI

2. Institute at Brown for Environment and Society, Brown University, Providence, RI

3. Applied Mathematics, Brown University, Providence, RI

4. Department of Geographical Sciences, University of Maryland, College Park, MD

Abstract

The Global Ecosystem Dynamics Investigation (GEDI) is generating predictions of aboveground biomass density (AGBD) in temperate and tropical regions at high spatial resolution. Models used to generate GEDI footprint-level AGBD for the release 1 and release 2 data products are stratified by Plant Functional Type (PFT) and geographic world region. Previous research has demonstrated that stratified AGBD models outperform a global model lacking stratification. However, the impact of current strata on AGBD prediction is unknown, and it is unclear whether the current stratification can be improved by breaking current strata into smaller ones, or combining existing strata into larger areas. If current strata represent variation in the relationship between AGBD and GEDI relative height (RH) metrics, the stratum-level relationship should predict AGBD as well as locally developed models within subsets of the same stratum. Here we test this assumption by developing AGBD models within 5-degree grid cells worldwide for 10 PFT-by-region prediction strata within the GEDI domain. We used statistical hypothesis testing to determine whether coefficients of local AGBD models are varying within currently-defined prediction strata and quantified the pairwise difference in AGBD predictions from the locally developed models using a worldwide sample of GEDI footprints. We found statistically different AGBD models trained on geographic subsets in the same prediction stratum and some of them generated divergent AGBD predictions, exceeding 50 Mg / ha. The results in most strata were not sensitive to regularization and model structure. Our study revealed significant geographic variation in relationships between AGBD and RH metrics and indicated that the heterogeneity of the relationships could be more complex than current PFT-by-Region stratification. The geographic subsets with limited training data and high heterogeneity need further investigation, demonstrating where to prioritize training data collection. Overall, this research will benefit

future versions of the AGBD data product from GEDI through stratification and training data collection.

Keywords: Global Ecosystem Dynamics Investigation, aboveground biomass density, stratification, regularization, transferability

1. Introduction

Terrestrial ecosystems act as both sources and sinks of carbon and are essential components of the global carbon cycle (Schimel, 1995; Houghton, 1996; Ruehr et al., 2023). Current estimates of carbon emissions from land use and land-cover change in terrestrial ecosystems exhibit high variability due to uncertainties in aboveground biomass density (Saatchi et al., 2011; Baccini et al., 2012; Houghton et al., 2012; Friedlingstein et al., 2019; Duncanson et al., 2022).

The Global Ecosystem Dynamics Investigation (GEDI) is the first spaceborne lidar designed for terrestrial ecosystems in temperate and tropical regions (Dubayah et al., 2020). GEDI seeks to improve our knowledge of aboveground carbon balance in terrestrial ecosystems by generating predictions of aboveground biomass density (AGBD) at a footprint size of 25 m. Models used to generate GEDI footprint-level AGBD for the release 1 and release 2 data products are based on simulated waveforms and stratified by Plant Functional Type (PFT) and geographic world region (Kellner et al., 2022). The predictors for the AGBD models are relative height (RH) metrics derived from GEDI waveforms (Kellner et al., 2022; Duncanson et al., 2022).

Previous research has demonstrated that stratified AGBD models outperform a global model lacking stratification (Duncanson et al., 2022). However, the current stratification is pragmatic: it is unclear whether the current stratification can be improved by breaking current

strata into smaller ones, or combining existing strata into larger areas. In other words, it is unclear if there is heterogeneity in the relationship between RH metrics and AGBD within each current prediction stratum used by GEDI AGBD models. If the relationship between AGBD and GEDI RH metrics (e.g., allometry) is homogeneous within the current strata, the stratum-level relationship should predict AGBD as well as locally developed models that are trained using geographic subsets of the training data from the same stratum. Or in other words, the locally developed models should be similar or predicting AGBD in similar ways.

To test if there is heterogeneity in the relationship between RH metrics and AGBD within each current prediction stratum used by GEDI AGBD models, we ask three questions: (1) Are AGBD models trained on geographic subsets in the same prediction stratum similar? (2) If not, what does the within-stratum variation mean for AGBD predictions? (3) What is the implication of the variation on future stratification and training data collection?

2. Methods

The training data we used in this study are 8,587 observations of field-estimated AGBD based on allometric models and RH metrics from simulated waveforms, the same training dataset used by the GEDI science team for developing GEDI04_A AGBD models (Kellner et al., 2022). We divided training data in 10 current prediction strata by geographic subset (i.e., 5° by 5° grid cell) to examine the similarity of the models trained on the geographic subsets (i.e., local models). We used 5° cells because this is the size of grid cells used by GEDI science team to test the geographic transferability of GEDI04_A models (Kellner et al., 2022). We only used subsets with at least 20 observations (Figure 1).

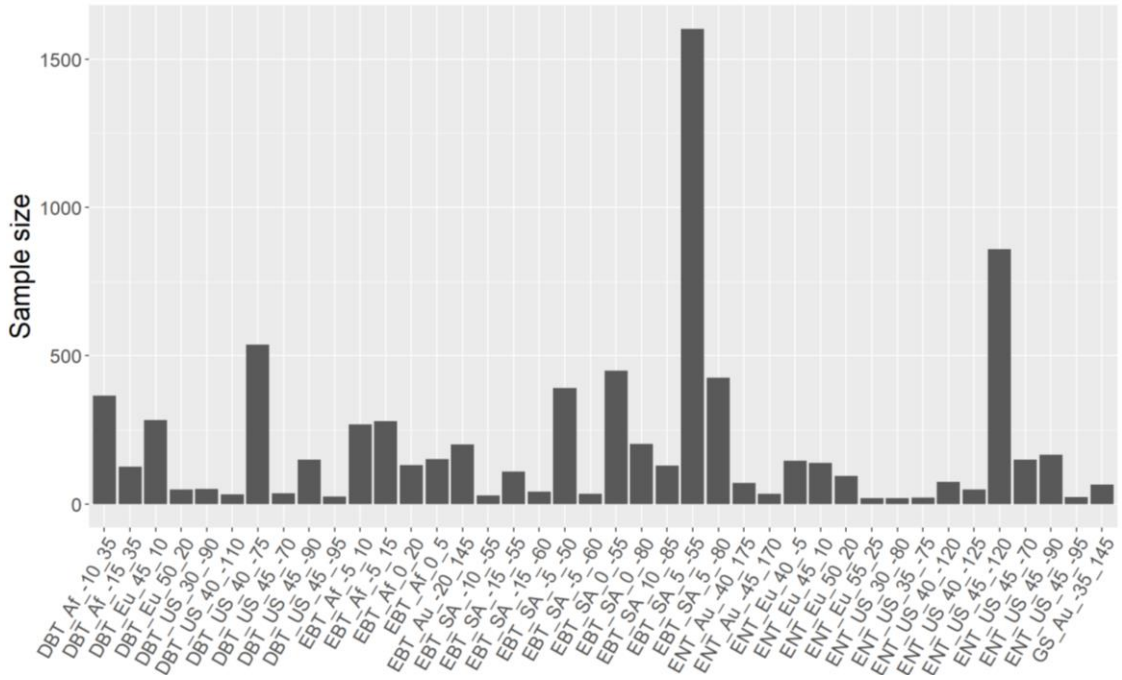

Figure 1. Sample size in each geographic subset of the studied strata. DBT: deciduous broadleaf tree; EBT: evergreen broadleaf tree; ENT: evergreen needleleaf tree; GS: grassland, shrubland, and woodland; US: North America; Eu: Europe; Au: Australia; Af: Africa; SA: South America.

To determine the similarity of local models, we tested the pairwise statistical difference of the model coefficients (i.e., section 2.1) and examined pairwise differences in AGBD predictions from the models using on-orbit GEDI footprints (i.e., section 2.2). Two versions of model predictors (i.e., RH metrics) were used (Table 1). In Version 1, RH metrics used for a local model were those employed in the GEDI04_A model of the corresponding prediction stratum. In Version 2, all local models were using the same RH metrics that came from the GEDI04_A PFT × Region models, and they are RH40, RH50, RH70, RH80, and RH98. This version was to keep the model structure the same, so that variation found from model comparisons would not be due to different model structures.

Table 1. Two versions of predictors used for local models in current prediction strata

Prediction stratum	Version 1	Version 2
DBT × Af	RH50, RH98	
DBT × Eu	RH70, RH98	
DBT × US	RH50, RH98	
EBT× Af	RH50, RH98	
EBT × Au	*	RH40, RH50, RH70,
EBT × SA	RH50, RH98	RH80, RH98
ENT × Au	RH40, RH98	
ENT × Eu	RH70, RH98	
ENT × US	RH70, RH98	
GS × Au	*	

* EBT × Au and GS × Au were not considered in Version 1 because they only had one geographic subset after excluding subsets with less than 20 observations. These two strata were considered in Version 2 because we did across-strata pairwise comparison.

2.1 Statistical difference of local models

We tested a null hypothesis to determine the pairwise statistical difference of the model coefficients (Weerahandi, 1987). A pair of local models whose coefficients to be compared were represented by Equations (1 – 2). Training data for Equation (1) were from one geographic subset, and training data for Equation (2) were from the other geographic subset:

$$y_1 = X_1\beta_1 + \varepsilon_1\,, \qquad \varepsilon_1 \sim N_{n_1}\left(0, \sigma_1^2 I_{n_1}\right), \tag{1}$$

$$y_2 = X_2\beta_2 + \varepsilon_2\,, \qquad \varepsilon_2 \sim N_{n_2}\left(0, \sigma_2^2 I_{n_2}\right), \tag{2}$$

where y_1 was the $n_1 \times 1$ vector of field-measured AGBD observations, y_2 was the $n_2 \times 1$ vector of field-measured AGBD observations, and X_1 and X_2 were matrices of RH metrics from simulated waveforms (the first column was 1) of sizes $n_1 \times k$ and $n_2 \times k$ respectively. β_1 or β_2 was the $k \times 1$ vector of model coefficients. $k = 3$ when two RH metrics were used in each local

model and each pair of local models was from the same stratum (i.e., Version 1 in Table 1). $k = 6$ when five RH metrics were used and a pair of local models could come from the same or different strata (i.e., Version 2 in Table 1). ε_1 or ε_2 was the error term. ε_1 was a $n_1 \times 1$ vector and ε_2 was a $n_2 \times 1$ vector. The covariate matrix of the error term distribution was a multiple of the identity matrix I_{n_1} or I_{n_2}. σ_1^2 or σ_2^2 was the variance of the error term.

The null hypothesis H_0 was

$$\beta_1 = \beta_2 \ . \tag{3}$$

We used a significance level of 0.05 to decide if accepting or rejecting the null hypothesis based on the approximate p-value below (Weerahandi, 1987):

$$p = 1 - E\left[F_{k,r}\left(\frac{r}{k}(\hat{\beta}_1 - \hat{\beta}_2)^T\left(\frac{v_1}{R}(X^T{}_1X_1)^{-1} + \frac{v_2}{1-R}(X^T{}_2X_2)^{-1}\right)^{-1}(\hat{\beta}_1 - \hat{\beta}_2)\right)\right] \tag{4}$$

where $r = n_1 + n_2 - 2k$, $F_{k,r}$ was the cumulative distribution function of F distribution with k and r degrees of freedom. The expectation was taken with respect to the random variable $R \sim Beta(\frac{n_1-k}{2}, \frac{n_2-k}{2})$. And

$$\hat{\beta}_i = (X^T{}_iX_i)^{-1}X^T{}_iy_i \ . \ i = 1,2. \tag{5}$$

$$v_i = (y_i - \hat{y}_i)^T(y_i - \hat{y}_i) \ . \ i = 1,2. \tag{6}$$

where $\hat{y}_i = X_i\hat{\beta}_i$.

We did the hypothesis testing to compare the statistical difference of model coefficients for both versions of predictors. For Version 2 predictors, we also used training data in current prediction strata (instead of geographic subsets of the strata) to do the hypothesis testing.

2.2 Prediction difference of local models

2.2.1 Model training

We trained linear models with the two versions of predictors in Table 1. We used linear models because GEDI04_A models are linear models. In each version of predictor variables, we trained both regularized and unregularized models. We used regularized models to avoid overfitting and extreme predictions considering the number of observations in a geographic subset was much smaller than that of a prediction stratum. Overfitting happens when a model fits training data so closely that it captures noise and it causes the model to be less likely to generalize well on unseen data (Vapnik and Chervonenkis, 1991). Regularization is a technique to improve model generalizability on unseen data by reducing the possibility of overfitting (Hastie et al., 2009).

We used L2 regularization to regularize linear models in the model training process. L2 regularization employs the L2 norm (i.e., the Euclidean norm) as the penalty term (Equation 7). We used L2 regularization because it permits analytic solutions through matrix inversion, while the other common way of regularization, L1 regularization, does not. L2 regularization encourages smaller model coefficients as the penalty will be greater when the coefficients are greater.

We used the mean squared error (MSE) as the loss for the unregularized model. The regularized loss function based on L2 regularization was:

$$Loss = \sum_{j=1}^{n}(y_j - r(X_j))^2 + \lambda \times \sum_{m=2}^{k}\beta_m^2 \quad (7)$$

where n represents the number of samples in the training data within a geographic subset, X_j represents the RH metrics of the jth sample from the training data, y_j represents the AGBD of the jth sample from the training data, $r(X_j) = \sum_{m=1}^{k}\beta_m X_m$ represents the predicted AGBD from the model based on RH metrics from the training data. $\sum_{m=2}^{k}\beta_m^2$ was the penalty term. β_m represents the mth coefficient in the model. m started from 2 because the first column in the

coefficient matrix was the intercept and the model did not penalize the intercept. $k = 3$ when two RH metrics were used (i.e., Version 1 in Table 1). $k = 6$ when five RH metrics were used (i.e., Version 2 in Table 1).

To determine λ in the loss function of each regularized local model, we conducted leave-one-out cross-validation (LOOCV), where we used each sample as the test data to calculate the loss and the rest of the samples as training data. The λ value we used for LOOCV was from 0 to 1 at a step of 0.0001, and then from 2 to 10 at a step of 1. We selected the λ that minimized regularized loss of each local model. We then determined model coefficients of each local model using all training data in the corresponding geographic subset by minimizing the regularized loss based on the selected λ.

2.2.2 Prediction difference using on-orbit GEDI data

We used RH metrics from 10,000 on-orbit GEDI footprints to predict AGBD based on the local models trained before and calculated the pairwise AGBD difference from the models. In Version 1 predictors, local models from the same stratum were compared and the on-orbit GEDI footprints came from the corresponding prediction stratum.

In Version 2 predictors, where local models from different prediction strata were also compared, we treated each local model as the focal model and calculated the pairwise difference in AGBD prediction from the focal model and each of the other local models (Figure 2). When a local model was the focal model, the on-orbit GEDI footprints used by all local models were the same and came from the stratum of the focal model. A pairwise AGBD difference could come from a pair of local models from the same stratum or from different strata.

To investigate if current strata were helpful in maintaining smaller variation within the stratum than outside the strata, for each focal model, we also calculated the mean difference

based on pairs of local models that came from the same stratum, and calculated the mean difference based on pairs of local models that came from different strata (Figure 2). If there is no within-stratum variation in the relationship between RH metrics and AGBD, the expectation is that the former mean difference should be smaller the latter mean difference.

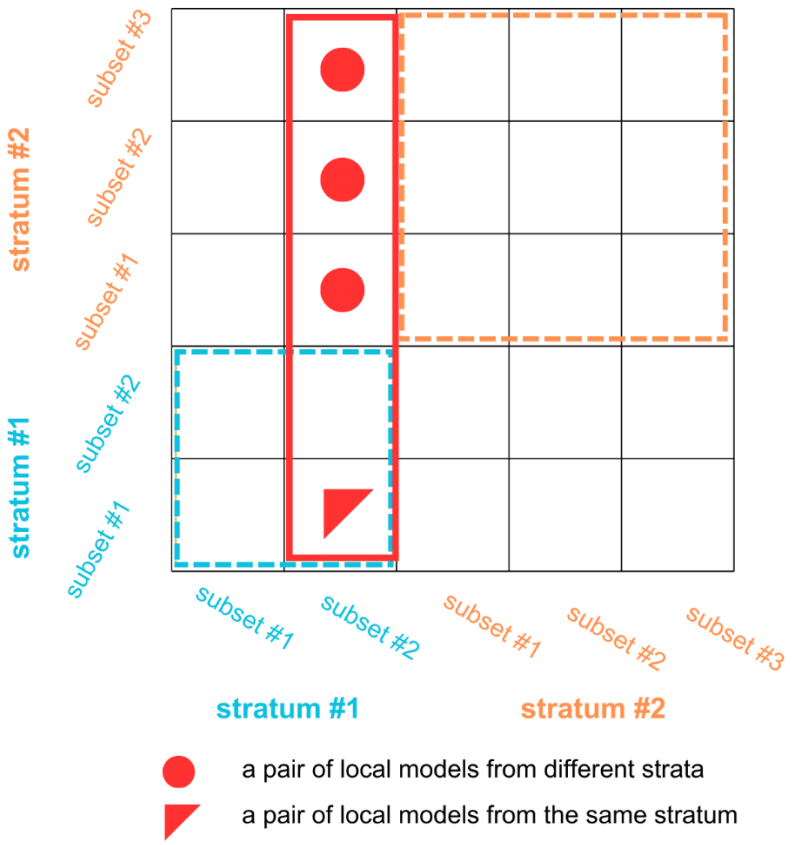

Figure 2. Illustration of the calculation of mean difference for each focal model. Each grid cell on the figure represents a pairwise AGBD difference from two local models trained on two geographic subsets. Each local model could be the focal model, and here the example focal model is the local model trained on data in geographic subset #2. The mean AGBD difference was calculated in two ways: (1) using AGBD difference from pairs of local models that came from the same stratum; (2) using AGBD difference from pairs of local models that came from different strata.

3. Results

3.1 Statistical difference of local models

We found statistically different local models within current prediction strata using both versions of predictors. When 2 RH metrics were used, we found statistical difference in local models within 7 of the 8 studied prediction strata; except that local models in DBT × Af did not have statistically different coefficients (Figure 3). When 5 RH metrics were used, we found statistical difference in local models within 6 of the 8 studied strata that had more than one geographic subset (Figure 4). Within each of the 6 strata, at least one pair of local models had statistically different model coefficients (Figure 4). Local models in DBT × Af or ENT × Au did not have statistically different coefficients (Figure 4).

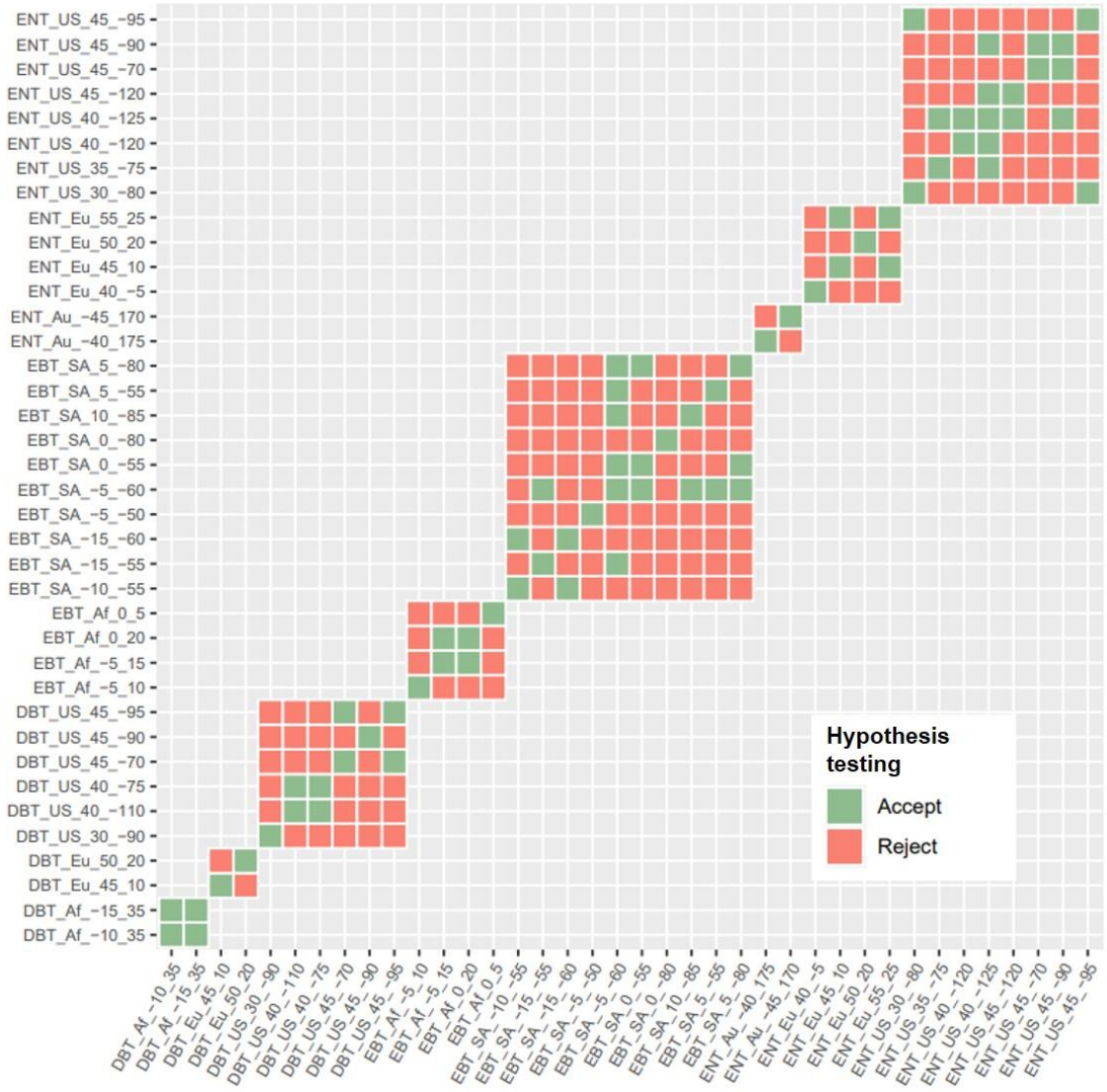

Figure 3. Hypothesis testing results based on Version 1 predictors (i.e., 2 RH metrics). A red cell represents a pair of local models with statistically different model coefficients. A green cell represents a pair of local models with the same model coefficients statistically.

Local models from different strata could also be statistically the same, even though most pairwise comparisons from different strata were connected to statistically different local models (Figure 4). A local model in EBT × SA had statistically the same model coefficients with all local models from EBT × Af (Figure 4: EBT_SA_-5_-60). The only local model in EBT × Au

had the same model coefficients statistically as two local models in EBT × SA (Figure 4: EBT_SA_-10_-55 and EBT_SA_-15_-60).

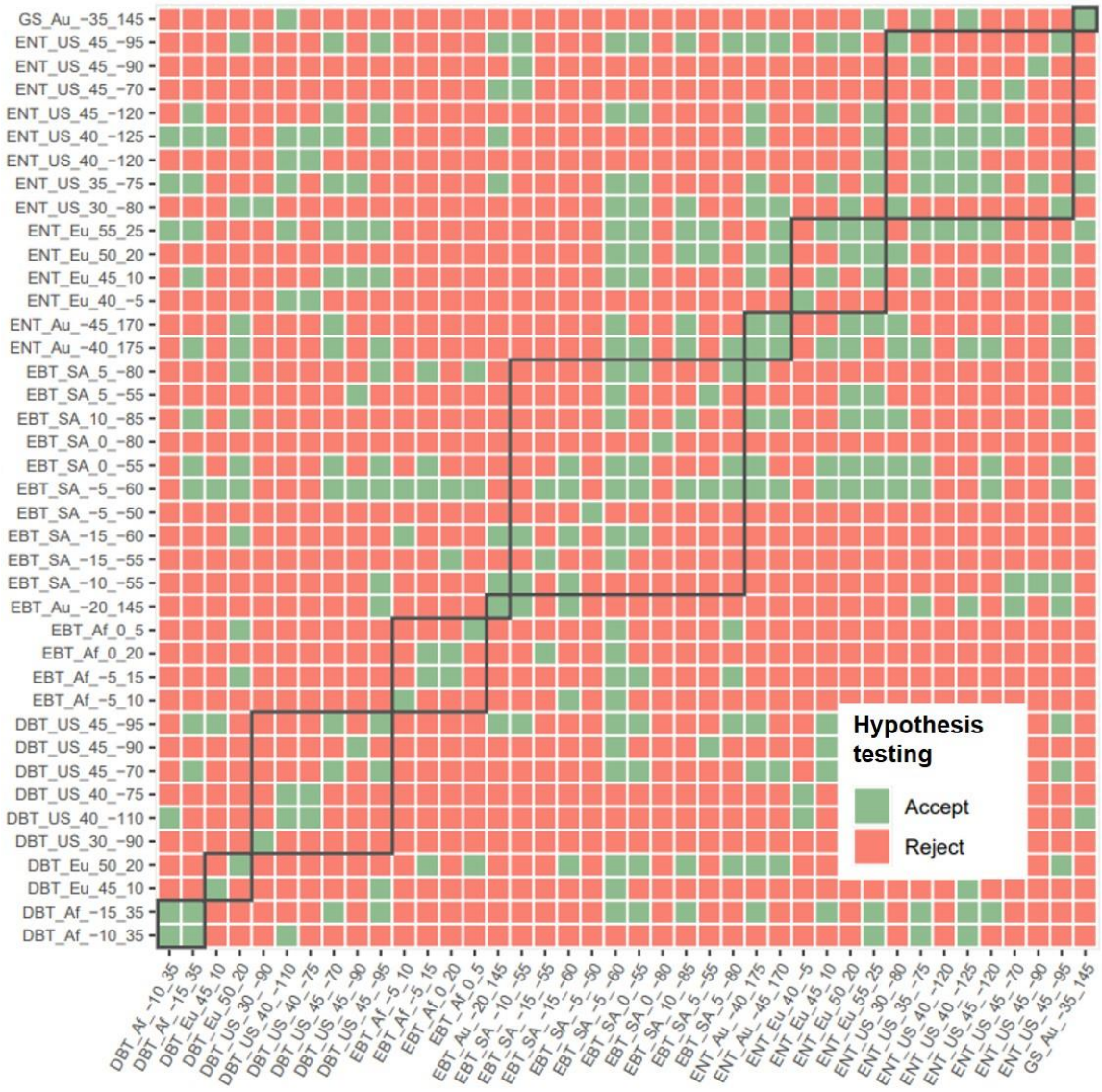

Figure 4. Hypothesis testing results based on Version 1 predictors (i.e., 5 RH metrics). A red cell represents a pair of local models with statistically different model coefficients. A green cell represents a pair of local models with the same model coefficients statistically. If a cell is inside a black bounding box, this means that the two relevant local models were from the same stratum; otherwise, the two local models were from different strata.

3.2 Prediction difference based on on-orbit GEDI footprints

This section only shows results without regularization because results based on regularization had little difference with results based on unregularized models. Results from regularized models can be found in Supplemental materials.

3.2.1 Prediction difference based on 2 RH metrics

We found notable pairwise AGBD differences from local models within the same prediction stratum (Figure 5). The pairwise AGBD difference were as great as 600 Mg / ha (Figure S7, EBT_SA_-15_-60), although the greatest difference decreased to 300 Mg / ha after regularization (Figure S8, EBT_SA_-15_-60). In the three prediction strata with most local models, most of the pairwise AGBD differences were around 50 Mg / ha (Figure 5A, DBT × US, EBT × SA, ENT × US). Local models in DBT × Af or DBT × Eu had little pairwise AGBD differences (Figure 5A). Note that local models in DBT × Eu were statistically different, but they had little AGBD difference.

Most of the normalized AGBD differences were around or above half of the mean AGBD from GEDI, both without and with regularization (Figure 5B, Figure S4B). Some local models had greater AGBD differences with the other local models in the same prediction stratum, such as ENT_US_30_-80, ENT_Eu_40_-5, EBT_SA_-10_-55, and DBT_US_30_-90 (Figure 5B).

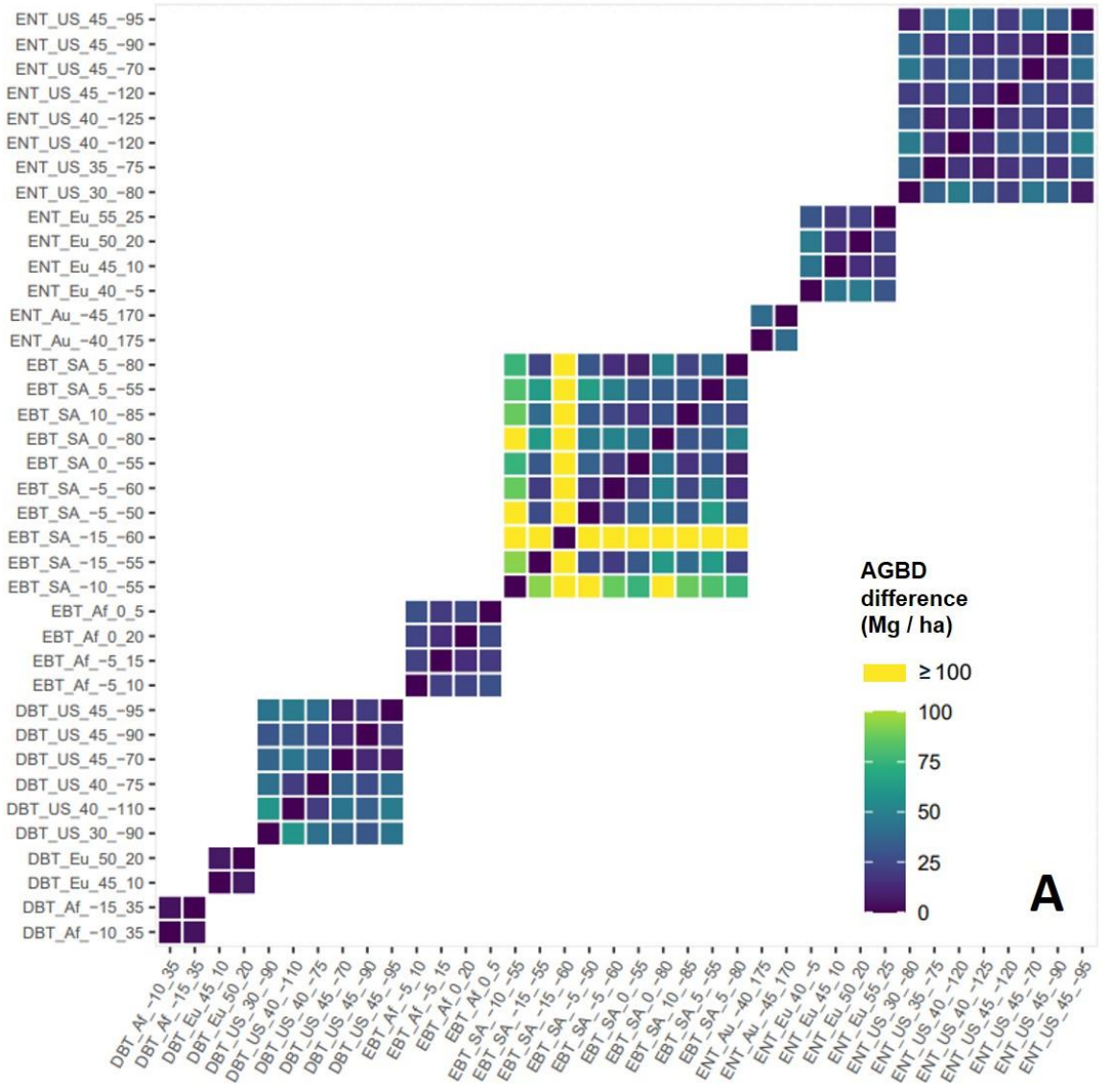
ENT_US_45_−95
ENT_US_45_−90
ENT_US_45_−70
ENT_US_45_−120
ENT_US_40_−125
ENT_US_40_−120
ENT_US_35_−75
ENT_US_30_−80
ENT_Eu_55_25
ENT_Eu_50_20
ENT_Eu_45_10
ENT_Eu_40_−5
ENT_Au_−45_170
ENT_Au_−40_175
EBT_SA_5_−80
EBT_SA_5_−55
EBT_SA_10_−85
EBT_SA_0_−80
EBT_SA_0_−55
EBT_SA_−5_−60
EBT_SA_−5_−50
EBT_SA_−15_−60
EBT_SA_−15_−55
EBT_SA_−10_−55
EBT_Af_0_5
EBT_Af_0_20
EBT_Af_−5_15
EBT_Af_−5_10
DBT_US_45_−95
DBT_US_45_−90
DBT_US_45_−70
DBT_US_40_−75
DBT_US_40_−110
DBT_US_30_−90
DBT_Eu_50_20
DBT_Eu_45_10
DBT_Af_−15_35
DBT_Af_−10_35
AGBD difference (Mg / ha)
≥ 100
100
75
50
25
0
A

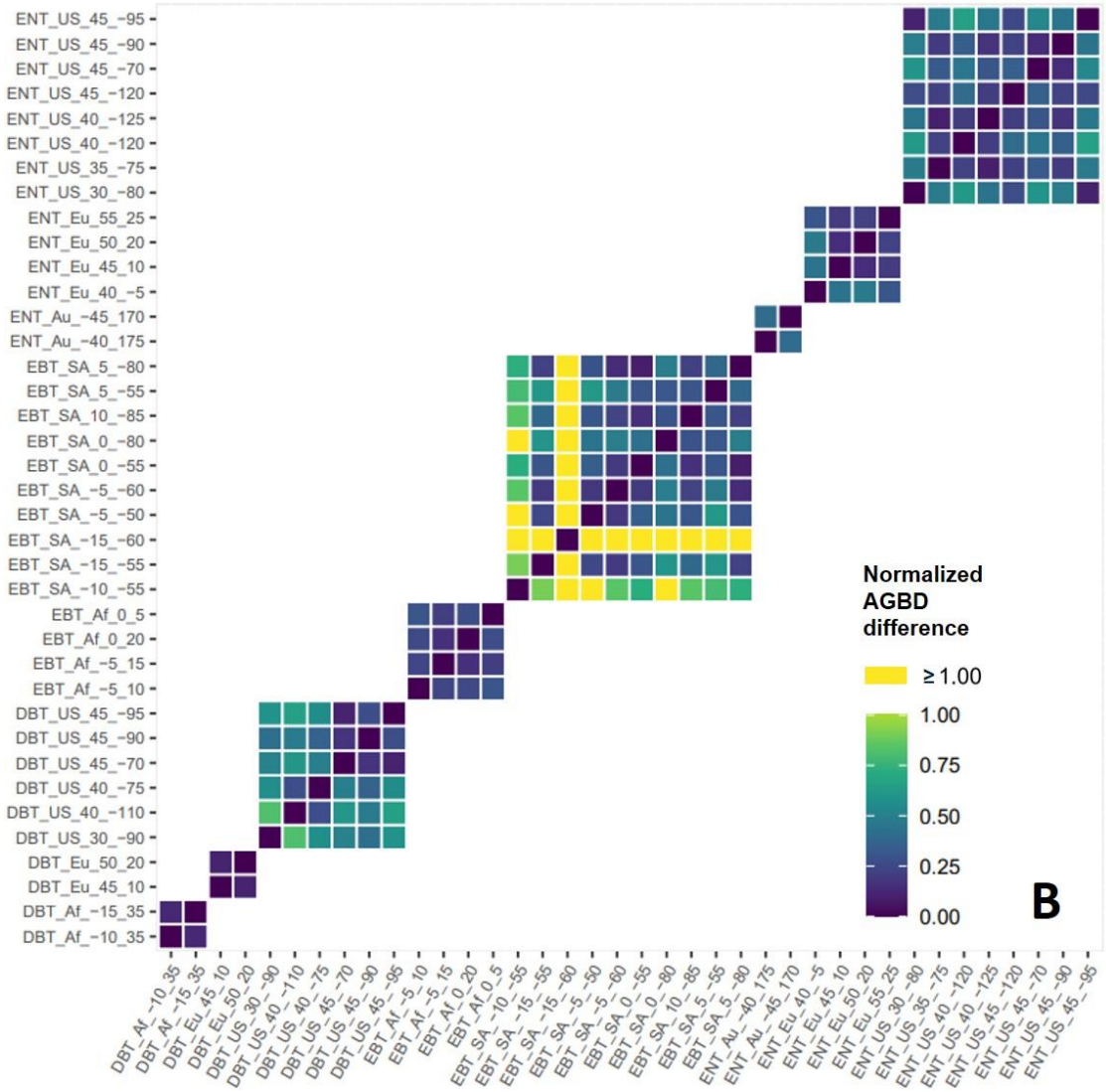

Figure 5. Difference in AGBD predictions from local models without regularization based on Version 1 predictors (i.e., 2 RH metrics). Each cell on the figure represents a pairwise AGBD difference from two local models. Each column represents a focal model. On-orbit GEDI footprints used for AGBD predictions came from the stratum of the focal model. A: Pairwise difference (unit: Mg / ha). Grid cells with differences greater than 100 Mg / ha are in yellow and are also shown in Figure S7 with actual values. B: Normalized difference by GEDI AGBD. Grid cells with normalized differences greater than 1 are in yellow.

3.2.2 Prediction difference based on 5 RH metrics

Similar to results from the 2-RH-metrics version, notable within-stratum AGBD differences were found when 5 RH metrics were used. Regularization still reduced the greatest pairwise AGBD difference, mostly for one local model in EBT × SA, as it did in results from the 2-RH-metrics version (Figure S9, Figure S10). A local model in EBT × SA had more divergent AGBD differences with the other local models within and without the EBT × SA stratum; and the difference could be greater than 600 Mg / ha (Figure S9, EBT_SA_-15_-60). After removing the differences involving this local model, there were still local models that had AGBD differences that were around 50 Mg / ha with the other local models in the same stratum, such as EBT × SA_-10_-55 (Figure 6A). Within the most prediction strata, most of the AGBD differences were above half of the mean AGBD from on-orbit GEDI footprints, similar to the results from the 2-RH-metrics version (Figure 6B).

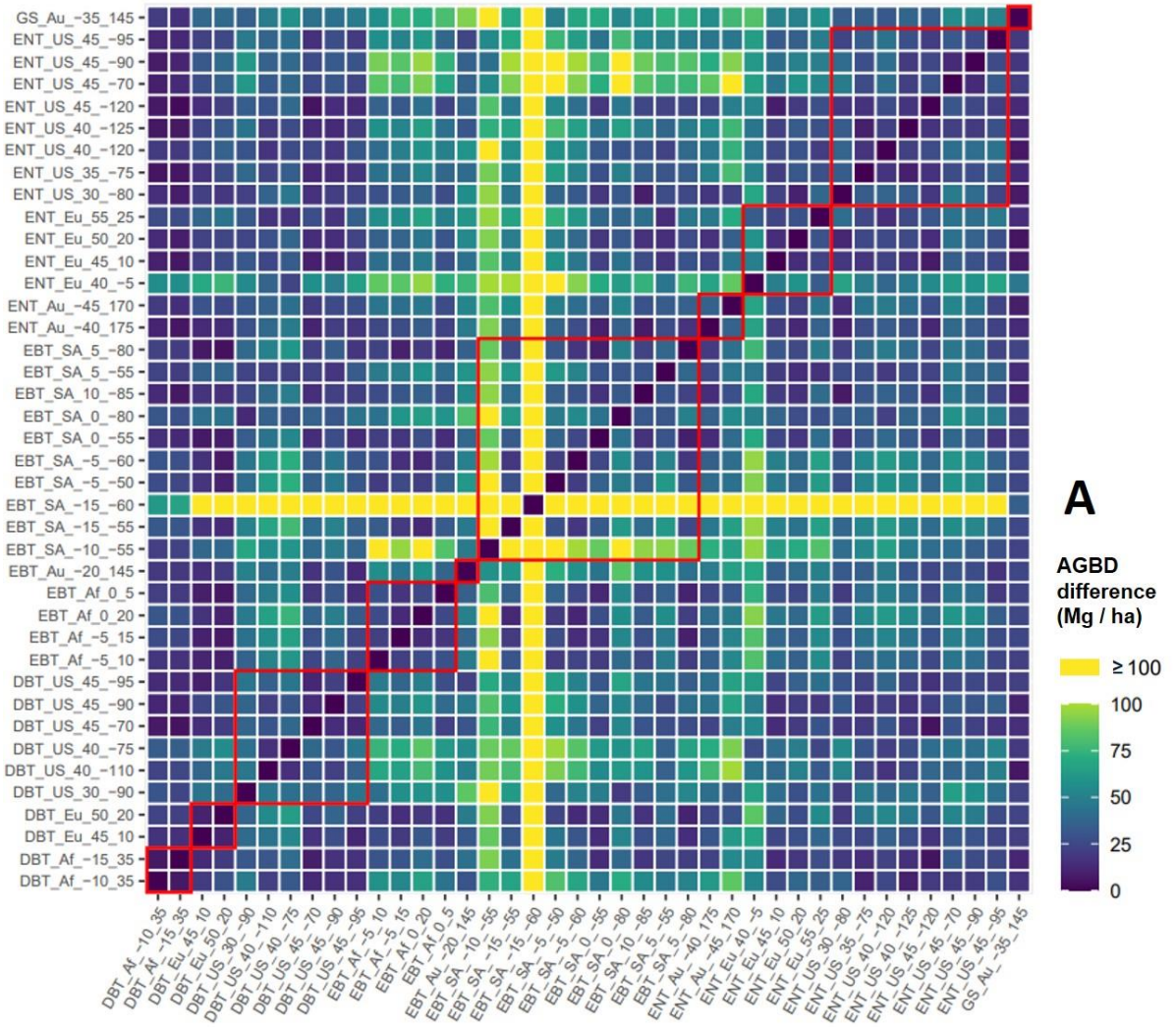
GS_Au_−35_145
ENT_US_45_−95
ENT_US_45_−90
ENT_US_45_−70
ENT_US_45_−120
ENT_US_40_−125
ENT_US_40_−120
ENT_US_35_−75
ENT_US_30_−80
ENT_Eu_55_25
ENT_Eu_50_20
ENT_Eu_45_10
ENT_Eu_40_−5
ENT_Au_−45_170
ENT_Au_−40_175
EBT_SA_5_−80
EBT_SA_5_−55
EBT_SA_10_−85
EBT_SA_0_−80
EBT_SA_0_−55
EBT_SA_−5_−60
EBT_SA_−5_−50
EBT_SA_−15_−60
EBT_SA_−15_−55
EBT_SA_−10_−55
EBT_Au_−20_145
EBT_Af_0_5
EBT_Af_0_20
EBT_Af_−5_15
EBT_Af_−5_10
DBT_US_45_−95
DBT_US_45_−90
DBT_US_45_−70
DBT_US_40_−75
DBT_US_40_−110
DBT_US_30_−90
DBT_Eu_50_20
DBT_Eu_45_10
DBT_Af_−15_35
DBT_Af_−10_35
A
AGBD difference (Mg / ha)
≥ 100
100
75
50
25
0

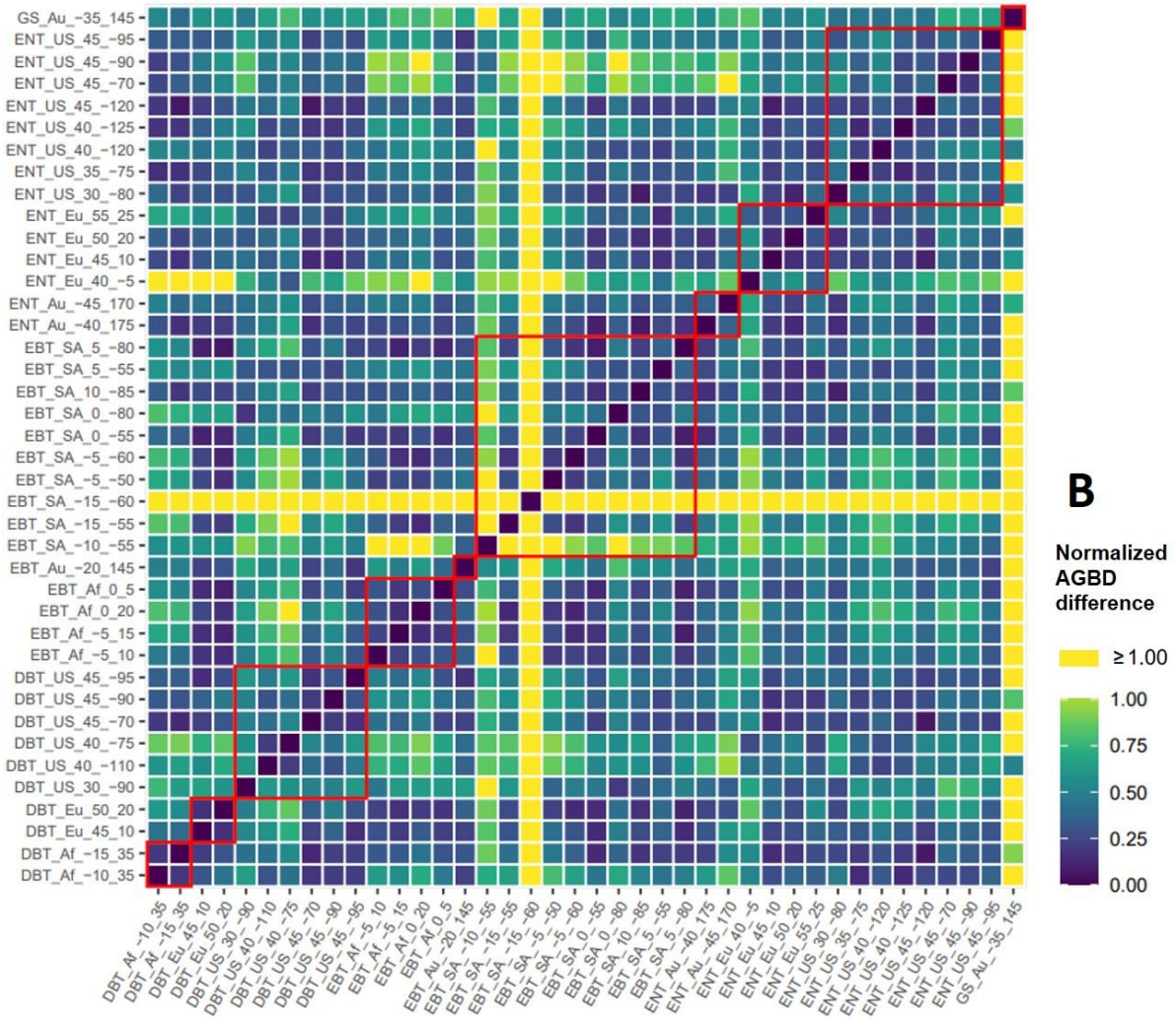

Figure 6. Difference in AGBD predictions from local models without regularization based on Version 2 predictors (i.e., 5 RH metrics). Each cell on the figure represents a pairwise AGBD difference from two local models. Each column represents a focal model. On-orbit GEDI footprints used for AGBD predictions came from the stratum of the focal model. A: Pairwise difference (unit: Mg / ha). Grid cells with differences greater than 100 Mg / ha are in yellow and are also shown in Figure S9 with actual values. B: Normalized difference by GEDI AGBD. Grid cells with normalized differences greater than 1 are in yellow.

Local models in the same stratum could be less similar than those from different strata, and no matter if certain local models were excluded, EBT × SA always had local models predicting AGBD more divergently from the same stratum than from different strata. (Figure 7, Figure S11). Only one stratum (i.e., EBT × SA) had local models with greater mean AGBD difference from the same stratum than from different strata; and all local models in EBT × SA were like this (Figure S11). When pairs of local models containing the outlier local model in EBT × SA (i.e., EBT_SA_-15_-60) were excluded from the mean difference calculation, most local models in EBT × SA predicted AGBD more convergently within the same stratum than across different strata (Figure 7), while DBT × US, ENT × Eu and ENT × US had 1 – 3 local models predicting more divergent AGBD within the same stratum than across different strata (Figure 7).

Regularization only made difference to 6 focal models in 4 strata (Figure 7, Figure S6). Regularized local models in ENT × Eu all predict AGBD more convergently within the stratum than across different strata (Figure S6). DBT × US, EBT × SA and ENT × US had 1 – 2 more focal models predicting more divergent AGBD within the same stratum than across different strata, meanwhile EBT × SA also had one less focal model like that (Figure S6).

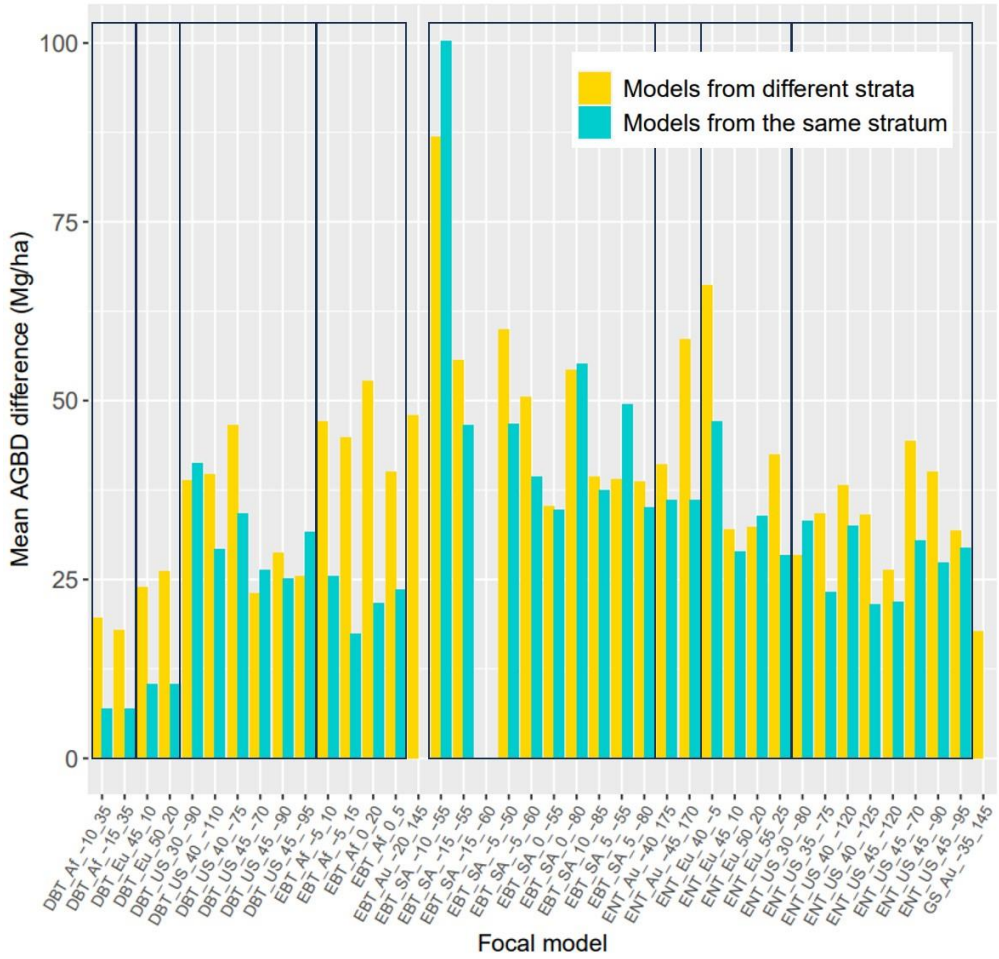

Figure 7. Mean AGBD difference from local models in the same or different strata without regularization based on Version 2 predictors (i.e., 5 RH metrics). The mean AGBD difference was calculated for each focal model based on pairwise difference within and without the red bounding box in Figure 6. Black bounding boxes represent prediction strata with more than one local model. The outlier subset (i.e., EBT_SA_-15_-60) in Figure 6 was excluded from the mean difference calculation. See Figure S11 for the mean difference including the outlier subset.

4. Discussion

4.1 Stratification

Within-stratum results based on the two versions of predictor variables (Table 1) are similar. Both versions demonstrated within-stratum variation in current prediction strata used by GEDI04_A AGBD data product by comparing both model coefficients and predictions based on on-orbit GEDI footprints. For example, EBT × SA had pairs of local models within the stratum (e.g., EBT_SA_-15_-60 and other local models in the stratum, EBT_SA_-10_-55 and other local models in the stratum) that were statistically different (Figure 3, 4) and the AGBD predictions from the models were also largely divergent (Figure 5, 6). DBT × US also had such pairs of local models (Figure 3, 4, 5, 6). Considering the precipitation gradient covered by deciduous broadleaf trees in North America (i.e., DBT × US), the variation we found in this study could be due to that the current PFT by Region stratification did not capture the precipitation gradient in the stratum.

However, the within-stratum variation should be further validated with more samples in geographic subsets with few observations. The two local models in EBT × SA mentioned above that had both statistical difference and divergent AGBD predictions with other local models in the stratum had small numbers of observations: EBT_SA_-15_-60 had 41 samples, and EBT_SA_-10_-55 had 28 samples.

We do not find evidence to split two current prediction strata: DBT × Af and DBT × Eu. Local models in DBT × Af had statistically the same model (Figure 3, 4) and predicted convergent AGBD (Figure 5, 6). DBT × Eu had statistically different local models (Figure 3, 4) but the AGBD predictions from the local models had little difference (Figure 5, 6). When 5 RH metrics were used (i.e., Table 1, Version 2), we found possibilities of combining these two strata with some geographic subsets in ENT × US (Figure 4, 6). For example, all four models in these two strata were statistically the same as some local models in ENT × US (Figure 4); and local models in DBT × Af had little pairwise AGBD differences with local models in ENT × US

(Figure 6). On the other hand, statistical hypothesis testing based on the two strata did not show the possibility for combination (Figure S1)

Version 2 predictor variables enabled comparisons across different strata. We were able to evaluate whether each prediction stratum was helpful in maintaining smaller prediction difference within the stratum than outside the stratum through comparing mean AGBD difference from the same and different strata based on focal models (Figure S11). EBT × SA was found to be a less helpful stratum because all local models had greater mean AGBD difference from the same stratum than from difference strata when they were used as focal models. Taking into consideration the impact of sample size of training data in the geographic subsets, there were still local models with a large number of samples that had greater AGBD prediction difference within the stratum than outside the stratum (e.g., Figure S11, EBT_SA_0_-55, EBT_SA_-5_-50). Results from regularized models showed two more local models with this issue (Figure S12, DBT_US_45_-95, ENT_US_45_-95), but they had small numbers of training data (Table 1).

We used on-orbit GEDI footprints to compare if the local models predicted AGBD in similar ways by quantifying the pairwise AGBD differences. This method to evaluate the stratification did not require field AGBD measurements and took advantage of on-orbit GEDI footprints. It has the potential to be used for evaluating stratification for AGBD models from other missions such as ESA BIOMASS and NASA-ISRO NISAR. The analysis also spoke to the transferability of GEDI AGBD models. Although the models used here were local models, rather than GEDI04_A models, the method of comparing AGBD prediction difference can be used to evaluate the necessity of splitting certain strata.

Note that this does not imply that finer strata are better. Regardless of the feasibility of using the finest strata to train AGBD models, finer strata may capture noise or features that cannot be generalized well on unseen data, similar to the idea of overfitting.

4.2 Regularization and training data collection of GEDI_04A models

Although regularization avoids extreme AGBD predictions, local models in most prediction strata were insensitive to regularization, except EBT_Af (Figure 4, 5, 6). This could be due to that the regularizations used in the study all penalized the model coefficients in similar ways.

Another aspect to interpret the insensitivity of the models to regularizations is that, even though the goal of regularizations was to improve the generalizability, there was still within-strata variation observed no matter whether regularization was used or not.

Considering the difficulty in training data collection, it is important to determine where to prioritize data collection. Our study shows that data collection is of higher priority in geographic subsets with few training samples (Table 1) and that caused within-stratum variation (e.g., Figure 5, 6, EBT_SA_-15_-60, EBT_SA_-10_-55). Those subsets are to be interrogated with more training data.

5. Conclusions

We interrogated the current GEDI aboveground biomass density data product by examining the variation in the relationship between RH metrics and AGBD in current prediction strata. We found statistically different local models in current prediction strata and some of them generated divergent AGBD predictions within the same stratum, exceeding 50 Mg / ha. Local models in some strata (e.g., EBT × SA) had more divergent AGBD predictions within the same

stratum than across different strata, indicating the strata were not helpful in maintaining smaller difference in AGBD predictions within the strata than across different strata. The results in most strata were not sensitive to regularization and model structure. The results revealed the heterogeneity of the relationship between carbon and structure could be more complex than current PFT-by-Region stratification. The within-stratum variation found in geographic subsets with limited training data demonstrated the need to prioritize training data collection in those regions. The research informs future versions of AGBD data products from GEDI through insights about stratification and training data collection.

Acknowledgements

This work was funded by NASA grant 80NSSC21K0195 (GEDI Science Team). We thank members of the GEDI Mission and Competed Science Teams, the NASA Terrestrial Ecology Program, and many individuals who contributed publicly available data that allowed GEDI04_A models to be developed. We thank David Laidlaw, Ziang Liu, and James Tompkin for advice on the analysis. We thank Center for Computation and Visualization at Brown University for computation resources and help.

References

Ahmed, S.E., Raheem, S.M.E., 2012. Shrinkage and absolute penalty estimation in linear regression models. WIREs Computational Statistics 4, 541–553. https://doi.org/10.1002/wics.1232

Baccini, A., Goetz, S.J., Walker, W.S., Laporte, N.T., Sun, M., Sulla-Menashe, D., Hackler, J., Beck, P.S.A., Dubayah, R., Friedl, M.A., Samanta, S., Houghton, R.A., 2012. Estimated carbon dioxide emissions from tropical deforestation improved by carbon-density maps.

Nature Clim Change 2, 182–185. https://doi.org/10.1038/nclimate1354

Cawley, G.C., 2006. Leave-One-Out Cross-Validation Based Model Selection Criteria for Weighted LS-SVMs, in: The 2006 IEEE International Joint Conference on Neural Network Proceedings. Presented at the The 2006 IEEE International Joint Conference on Neural Network Proceedings, pp. 1661–1668. https://doi.org/10.1109/IJCNN.2006.246634

Dubayah, R., Blair, J.B., Goetz, S., Fatoyinbo, L., Hansen, M., Healey, S., Hofton, M., Hurtt, G., Kellner, J., Luthcke, S., Armston, J., Tang, H., Duncanson, L., Hancock, S., Jantz, P., Marselis, S., Patterson, P.L., Qi, W., Silva, C., 2020. The Global Ecosystem Dynamics Investigation: High-resolution laser ranging of the Earth's forests and topography. Science of Remote Sensing 1, 100002. https://doi.org/10.1016/j.srs.2020.100002

Duncanson, L., Kellner, J.R., Armston, J., Dubayah, R., Minor, D.M., Hancock, S., Healey, S.P., Patterson, P.L., Saarela, S., Marselis, S., Silva, C.E., Bruening, J., Goetz, S.J., Tang, H., Hofton, M., Blair, B., Luthcke, S., Fatoyinbo, L., Abernethy, K., Alonso, A., Andersen, H.-E., Aplin, P., Baker, T.R., Barbier, N., Bastin, J.F., Biber, P., Boeckx, P., Bogaert, J., Boschetti, L., Boucher, P.B., Boyd, D.S., Burslem, D.F.R.P., Calvo-Rodriguez, S., Chave, J., Chazdon, R.L., Clark, D.B., Clark, D.A., Cohen, W.B., Coomes, D.A., Corona, P., Cushman, K.C., Cutler, M.E.J., Dalling, J.W., Dalponte, M., Dash, J., de-Miguel, S., Deng, S., Ellis, P.W., Erasmus, B., Fekety, P.A., Fernandez-Landa, A., Ferraz, A., Fischer, R., Fisher, A.G., García-Abril, A., Gobakken, T., Hacker, J.M., Heurich, M., Hill, R.A., Hopkinson, C., Huang, H., Hubbell, S.P., Hudak, A.T., Huth, A., Imbach, B., Jeffery, K.J., Katoh, M., Kearsley, E., Kenfack, D., Kljun, N., Knapp, N., Král, K., Krůček, M., Labrière, N., Lewis, S.L., Longo, M., Lucas, R.M., Main, R., Manzanera,

J.A., Martínez, R.V., Mathieu, R., Memiaghe, H., Meyer, V., Mendoza, A.M., Monerris, A., Montesano, P., Morsdorf, F., Næsset, E., Naidoo, L., Nilus, R., O'Brien, M., Orwig, D.A., Papathanassiou, K., Parker, G., Philipson, C., Phillips, O.L., Pisek, J., Poulsen, J.R., Pretzsch, H., Rüdiger, C., Saatchi, S., Sanchez-Azofeifa, A., Sanchez-Lopez, N., Scholes, R., Silva, C.A., Simard, M., Skidmore, A., Stereńczak, K., Tanase, M., Torresan, C., Valbuena, R., Verbeeck, H., Vrska, T., Wessels, K., White, J.C., White, L.J.T., Zahabu, E., Zgraggen, C., 2022. Aboveground biomass density models for NASA's Global Ecosystem Dynamics Investigation (GEDI) lidar mission. Remote Sensing of Environment 270, 112845. https://doi.org/10.1016/j.rse.2021.112845

Friedlingstein, P., Jones, M.W., O'Sullivan, M., Andrew, R.M., Hauck, J., Peters, G.P., Peters, W., Pongratz, J., Sitch, S., Le Quéré, C., Bakker, D.C.E., Canadell, J.G., Ciais, P., Jackson, R.B., Anthoni, P., Barbero, L., Bastos, A., Bastrikov, V., Becker, M., Bopp, L., Buitenhuis, E., Chandra, N., Chevallier, F., Chini, L.P., Currie, K.I., Feely, R.A., Gehlen, M., Gilfillan, D., Gkritzalis, T., Goll, D.S., Gruber, N., Gutekunst, S., Harris, I., Haverd, V., Houghton, R.A., Hurtt, G., Ilyina, T., Jain, A.K., Joetzjer, E., Kaplan, J.O., Kato, E., Klein Goldewijk, K., Korsbakken, J.I., Landschützer, P., Lauvset, S.K., Lefèvre, N., Lenton, A., Lienert, S., Lombardozzi, D., Marland, G., McGuire, P.C., Melton, J.R., Metzl, N., Munro, D.R., Nabel, J.E.M.S., Nakaoka, S.-I., Neill, C., Omar, A.M., Ono, T., Peregon, A., Pierrot, D., Poulter, B., Rehder, G., Resplandy, L., Robertson, E., Rödenbeck, C., Séférian, R., Schwinger, J., Smith, N., Tans, P.P., Tian, H., Tilbrook, B., Tubiello, F.N., van der Werf, G.R., Wiltshire, A.J., Zaehle, S., 2019. Global Carbon Budget 2019. Earth System Science Data 11, 1783–1838. https://doi.org/10.5194/essd-11-1783-2019

Goeman, J., Meijer, R., Chaturvedi, N., 2012. L1 and L2 penalized regression models. cran. r-project. or.

Hastie, T., Tibshirani, R., Friedman, J., 2009. Basis Expansions and Regularization, in: Hastie, T., Tibshirani, R., Friedman, J. (Eds.), The Elements of Statistical Learning: Data Mining, Inference, and Prediction, Springer Series in Statistics. Springer, New York, NY, pp. 139–189. https://doi.org/10.1007/978-0-387-84858-7_5

Houghton, R.A., 1996. Converting Terrestrial Ecosystems from Sources to Sinks of Carbon. Ambio 25, 267–272.

Houghton, R.A., House, J.I., Pongratz, J., van der Werf, G.R., DeFries, R.S., Hansen, M.C., Le Quéré, C., Ramankutty, N., 2012. Carbon emissions from land use and land-cover change. Biogeosciences 9, 5125–5142. https://doi.org/10.5194/bg-9-5125-2012

Kellner, J.R., Armston, J., Duncanson, L., 2022. Algorithm theoretical basis document for GEDI footprint aboveground biomass density. Earth and Space Science. https://doi.org/10.1029/2022EA002516

Rad, K.R., Maleki, A., 2020. A Scalable Estimate of the Out-of-Sample Prediction Error via Approximate Leave-One-Out Cross-Validation. Journal of the Royal Statistical Society Series B: Statistical Methodology 82, 965–996. https://doi.org/10.1111/rssb.12374

Ruehr, S., Keenan, T.F., Williams, C., Zhou, Y., Lu, X., Bastos, A., Canadell, J.G., Prentice, I.C., Sitch, S., Terrer, C., 2023. Evidence and attribution of the enhanced land carbon sink. Nature Reviews Earth & Environment 4, 518–534.

Saatchi, S.S., Harris, N.L., Brown, S., Lefsky, M., Mitchard, E.T.A., Salas, W., Zutta, B.R., Buermann, W., Lewis, S.L., Hagen, S., Petrova, S., White, L., Silman, M., Morel, A., 2011. Benchmark map of forest carbon stocks in tropical regions across three continents.

PNAS 108, 9899–9904. https://doi.org/10.1073/pnas.1019576108

Schimel, D.S., 1995. Terrestrial ecosystems and the carbon cycle. Global Change Biology 1, 77–91. https://doi.org/10.1111/j.1365-2486.1995.tb00008.x

Tian, Y., Zhang, Y., 2022. A comprehensive survey on regularization strategies in machine learning. Information Fusion 80, 146–166. https://doi.org/10.1016/j.inffus.2021.11.005

Vapnik, V.N., Chervonenkis, A.Y., 1991. The necessary and sufficient conditions for consistency in the empirical risk minimization method. Pattern Recognition and Image Analysis 1, 283–305.

Weerahandi, S., 1987. Testing Regression Equality with Unequal Variances. Econometrica 55, 1211–1215. https://doi.org/10.2307/1911268

Supplemental materials

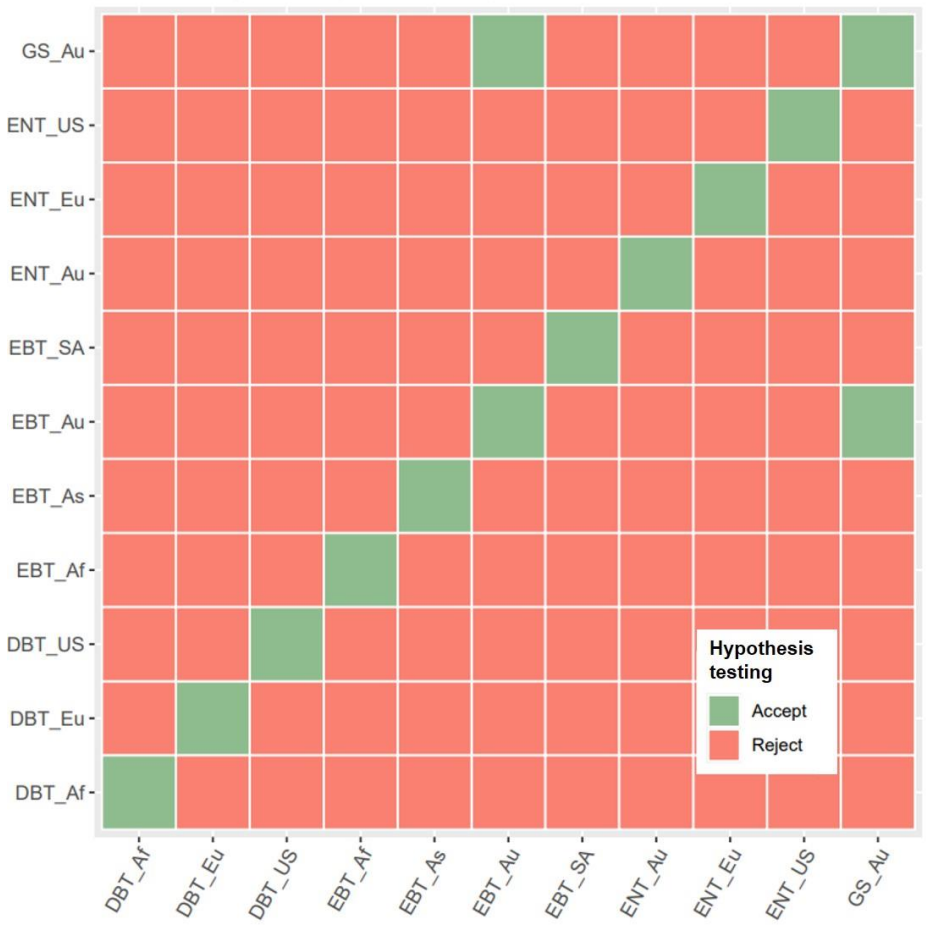

Figure S1. Hypothesis testing results using GEDI04_A PFT × Region prediction strata based on Version 2 predictors (i.e., 5 RH metrics). A red cell represents a pair of statistically different local models. A red cell represents a pair of local models with statistically different model coefficients. A green cell represents a pair of local models with the same model coefficients statistically.

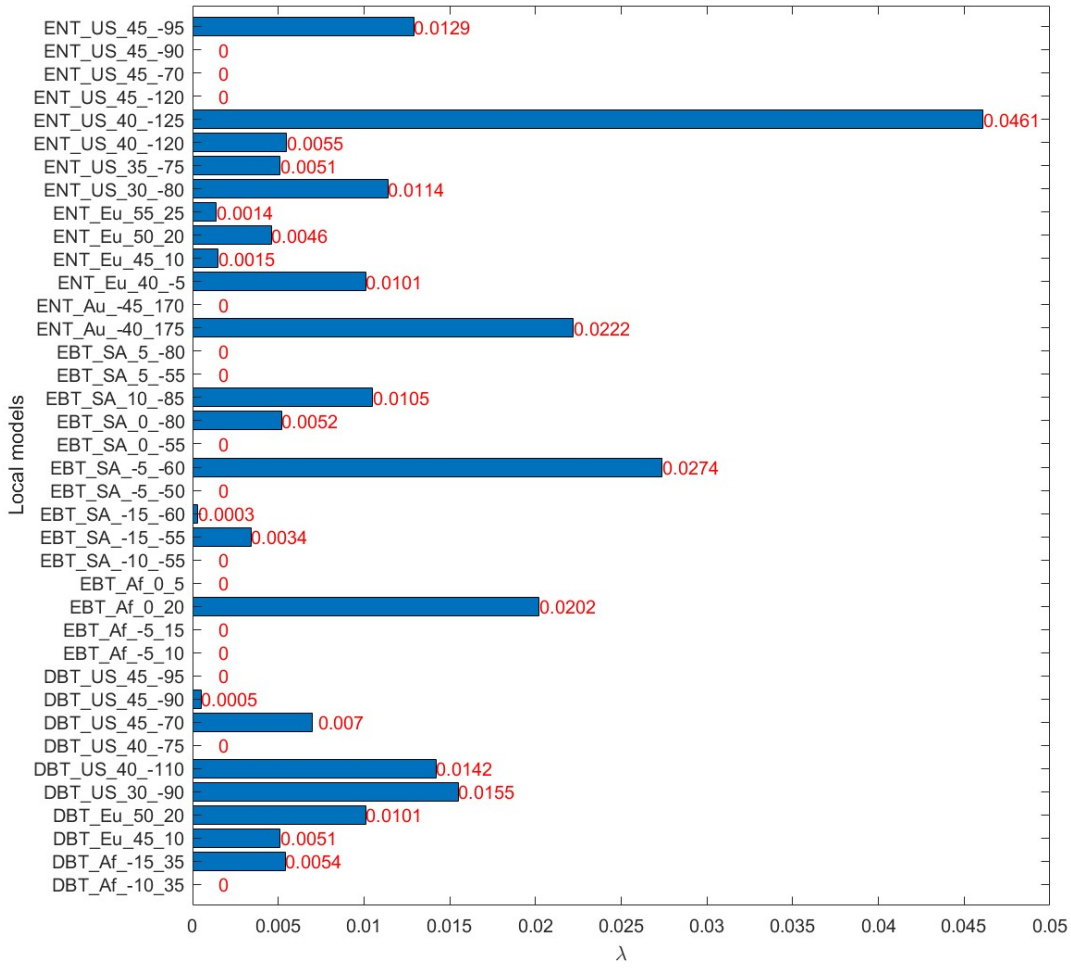

Figure S2. λ of the local model in L2 regularization based on 2 RH metrics

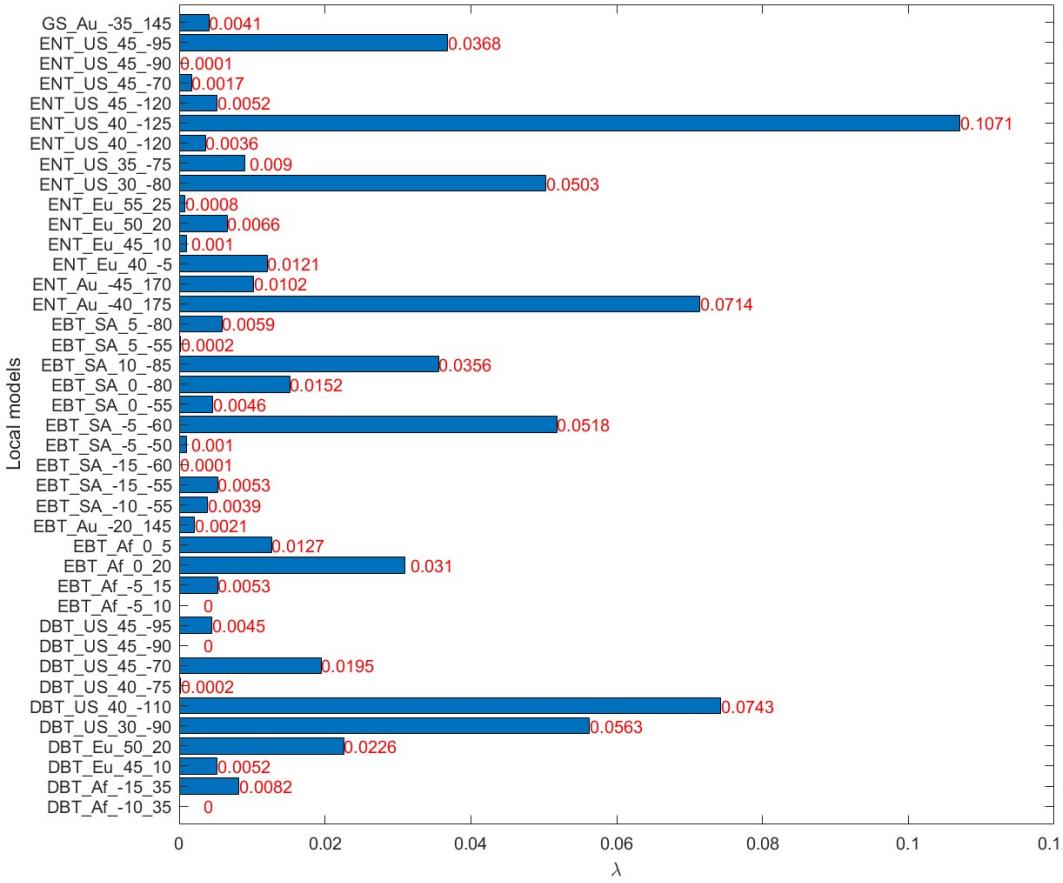

Figure S3. λ of the local model in L2 regularization based on 5 RH metrics

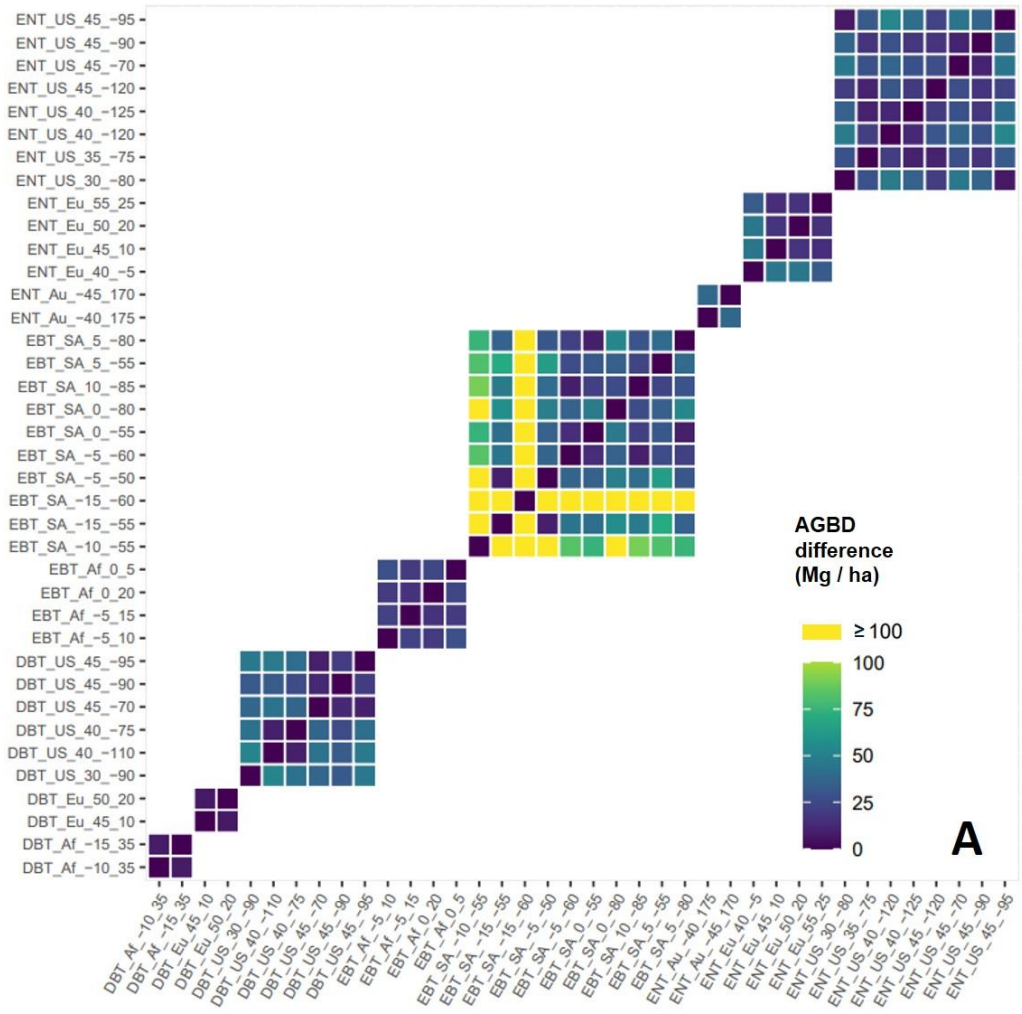
ENT_US_45_−95
ENT_US_45_−90
ENT_US_45_−70
ENT_US_45_−120
ENT_US_40_−125
ENT_US_40_−120
ENT_US_35_−75
ENT_US_30_−80
ENT_Eu_55_25
ENT_Eu_50_20
ENT_Eu_45_10
ENT_Eu_40_−5
ENT_Au_−45_170
ENT_Au_−40_175
EBT_SA_5_−80
EBT_SA_5_−55
EBT_SA_10_−85
EBT_SA_0_−80
EBT_SA_0_−55
EBT_SA_−5_−60
EBT_SA_−5_−50
EBT_SA_−15_−60
EBT_SA_−15_−55
EBT_SA_−10_−55
EBT_Af_0_5
EBT_Af_0_20
EBT_Af_−5_15
EBT_Af_−5_10
DBT_US_45_−95
DBT_US_45_−90
DBT_US_45_−70
DBT_US_40_−75
DBT_US_40_−110
DBT_US_30_−90
DBT_Eu_50_20
DBT_Eu_45_10
DBT_Af_−15_35
DBT_Af_−10_35
AGBD
difference
(Mg / ha)
≥ 100
100
75
50
25
0
A

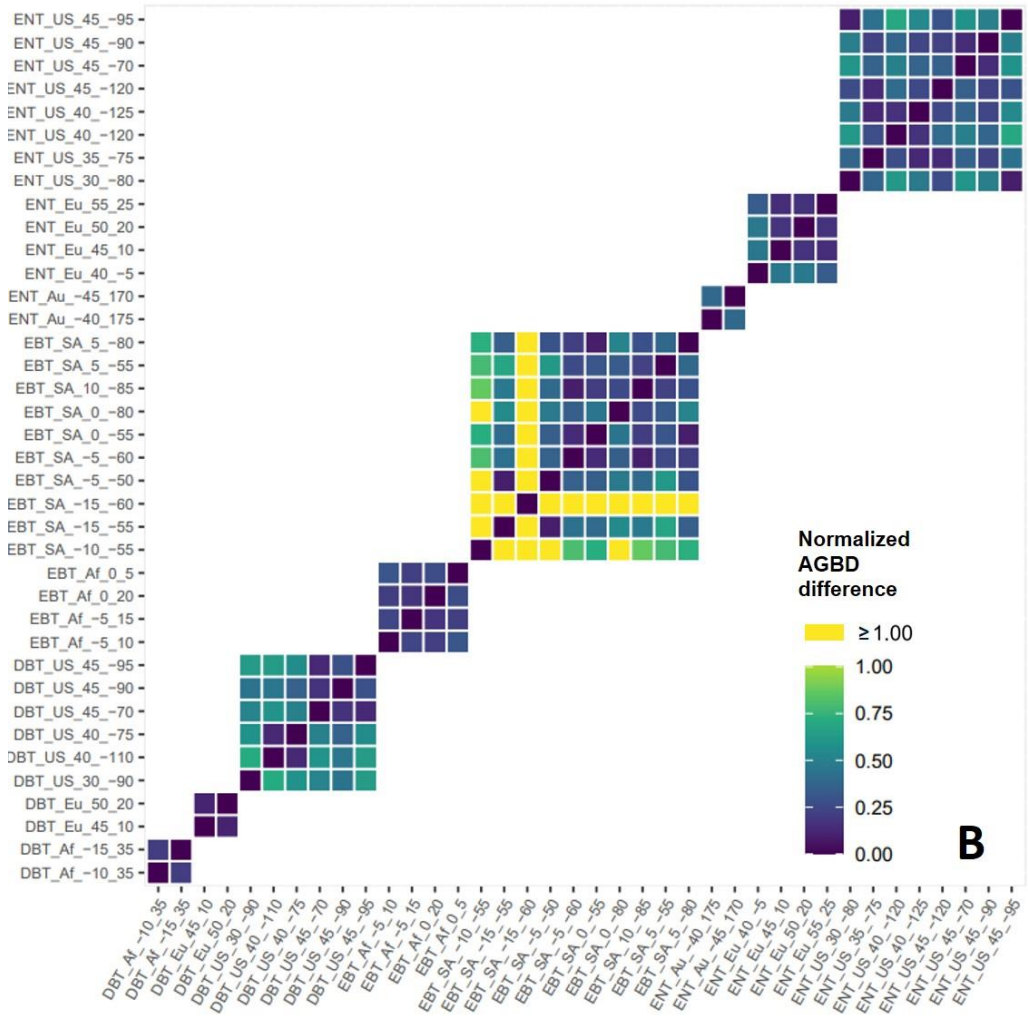

Figure S4. Difference in AGBD predictions from local models with L2 regularization based on Version 1 predictors (i.e., 2 RH metrics). Each cell on the figure represents a pairwise AGBD difference from two local models. Each column represents a focal model. On-orbit GEDI footprints used for AGBD predictions came from the stratum of the focal model. A: Pairwise difference (unit: Mg / ha). Grid cells with differences greater than 100 Mg / ha are in yellow and are also plotted based on actual values in Figure S8. B: Normalized difference by GEDI AGBD. Grid cells with normalized differences greater than 1 are in yellow.

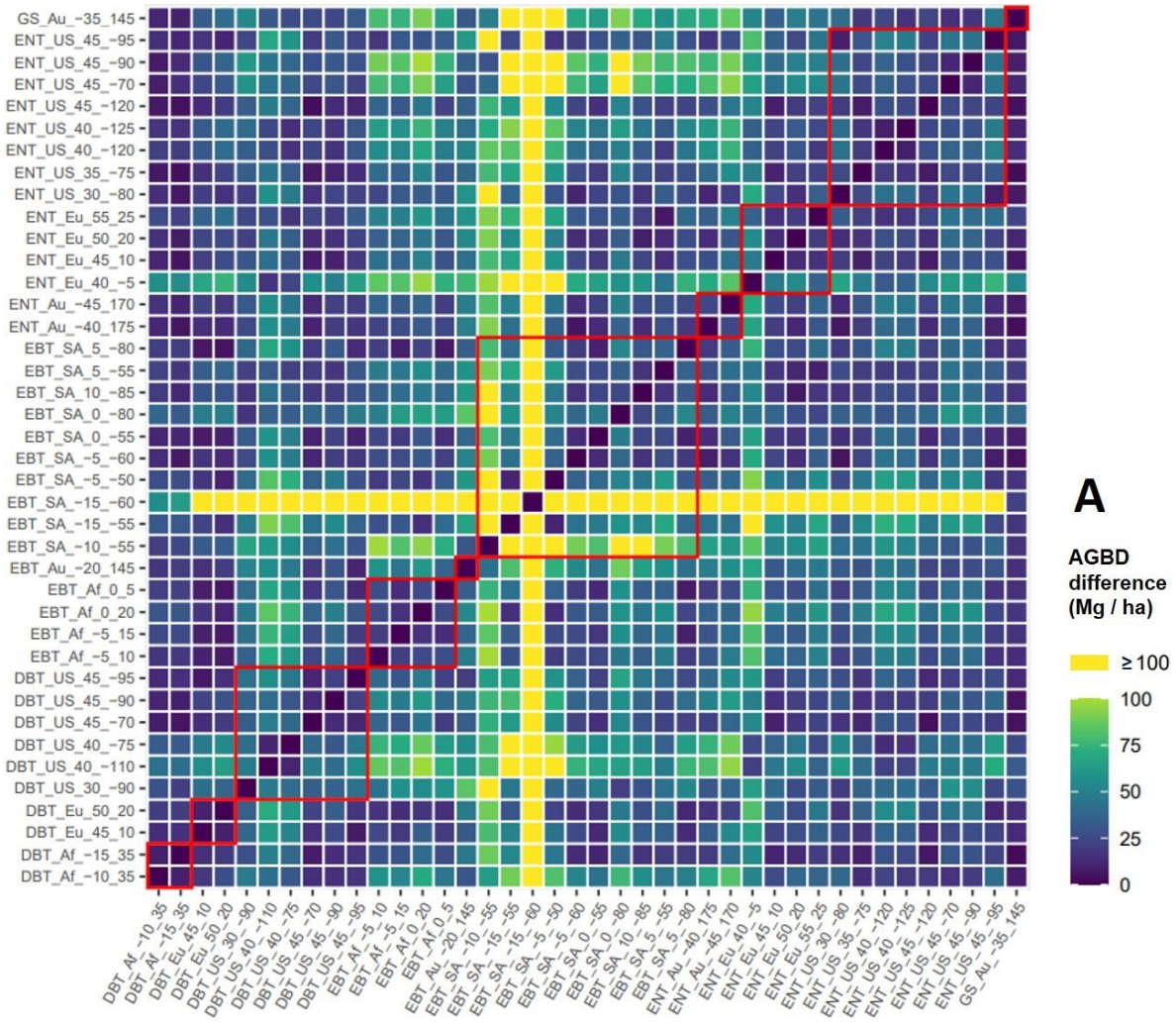
GS_Au_−35_145
ENT_US_45_−95
ENT_US_45_−90
ENT_US_45_−70
ENT_US_45_−120
ENT_US_40_−125
ENT_US_40_−120
ENT_US_35_−75
ENT_US_30_−80
ENT_Eu_55_25
ENT_Eu_50_20
ENT_Eu_45_10
ENT_Eu_40_−5
ENT_Au_−45_170
ENT_Au_−40_175
EBT_SA_5_−80
EBT_SA_5_−55
EBT_SA_10_−85
EBT_SA_0_−80
EBT_SA_0_−55
EBT_SA_−5_−60
EBT_SA_−5_−50
EBT_SA_−15_−60
EBT_SA_−15_−55
EBT_SA_−10_−55
EBT_Au_−20_145
EBT_Af_0_5
EBT_Af_0_20
EBT_Af_−5_15
EBT_Af_−5_10
DBT_US_45_−95
DBT_US_45_−90
DBT_US_45_−70
DBT_US_40_−75
DBT_US_40_−110
DBT_US_30_−90
DBT_Eu_50_20
DBT_Eu_45_10
DBT_Af_−15_35
DBT_Af_−10_35
A
AGBD difference (Mg / ha)
≥ 100
100
75
50
25
0

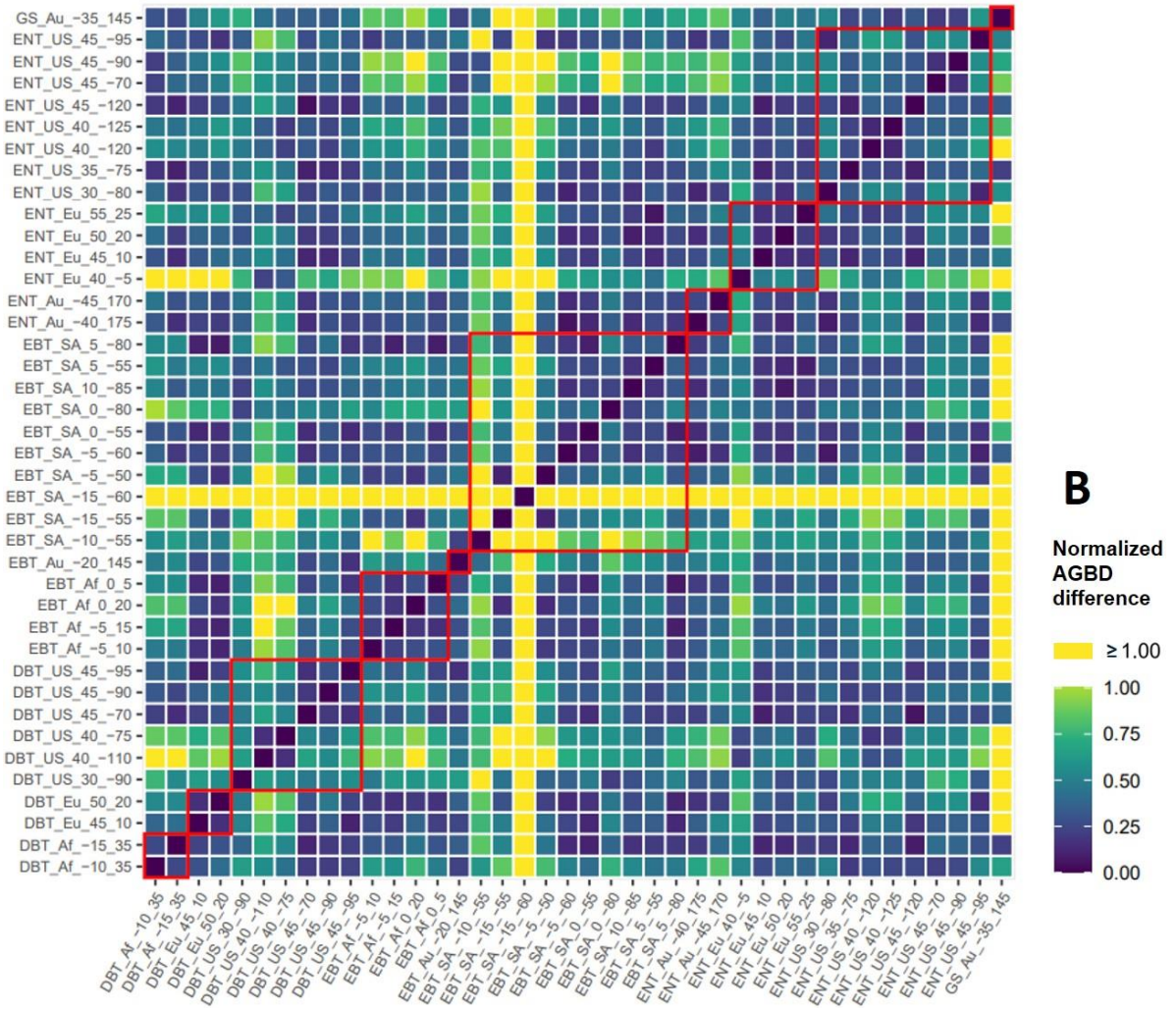

Figure S5. Difference in AGBD predictions from local models with L2 regularization based on Version 2 predictors (i.e., 5 RH metrics). Each cell on the figure represents a pairwise AGBD difference from two local models. Each column represents a focal model. On-orbit GEDI footprints used for AGBD predictions came from the stratum of the focal model. A: Pairwise difference (unit: Mg / ha). Grid cells with differences greater than 100 Mg / ha are in yellow and are also plotted based on actual values in Figure S10. B: Normalized difference by GEDI AGBD. Grid cells with normalized differences greater than 1 are in yellow.

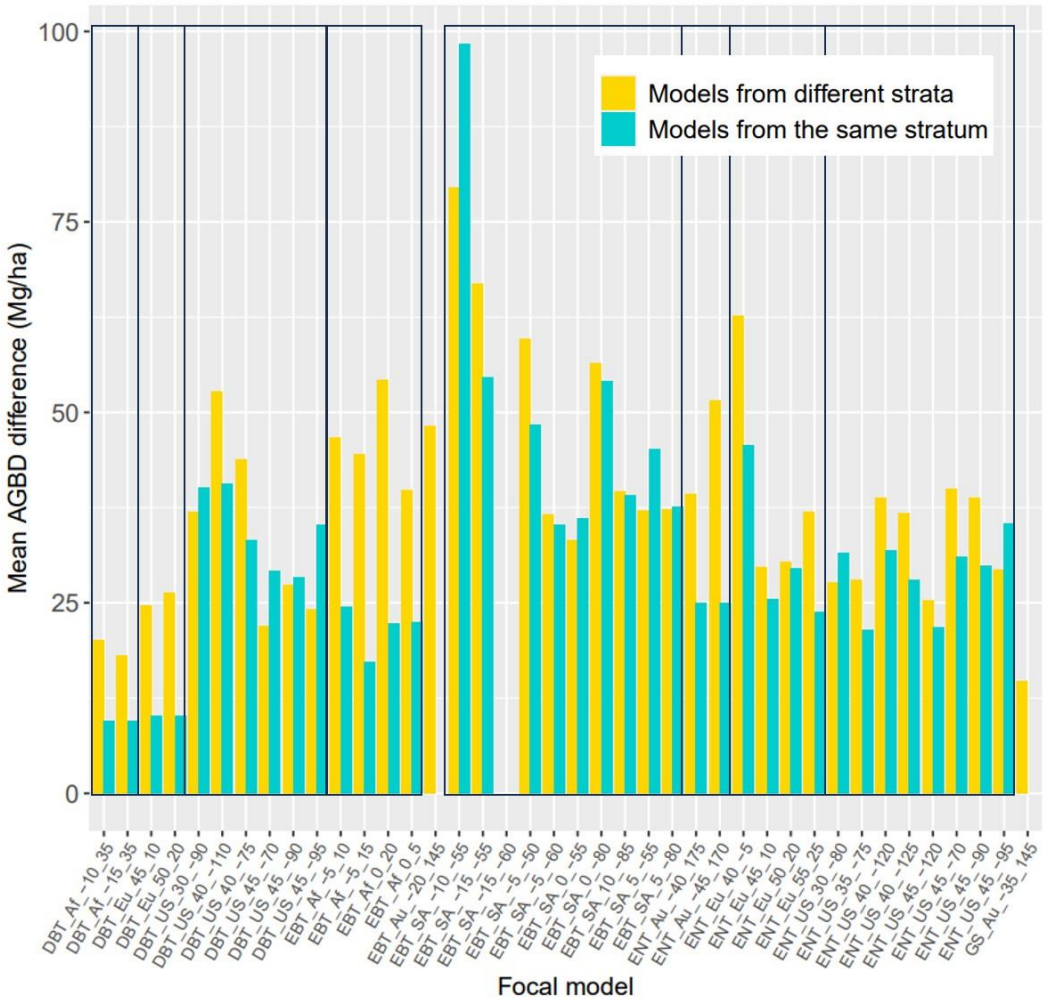

Figure S6. Mean AGBD difference from local models in the same or different strata with L2 regularization based on Version 2 predictors (i.e., 5 RH metrics). The mean AGBD difference was calculated for each focal model based on pairwise difference within and without the red bounding box in Figure 6. Black bounding boxes represent prediction strata with more than one local model. The outlier subset (i.e., EBT_SA_-15_-60) in Figure S5 was excluded from the mean difference calculation. See Figure S12 for the mean difference including the outlier subset.

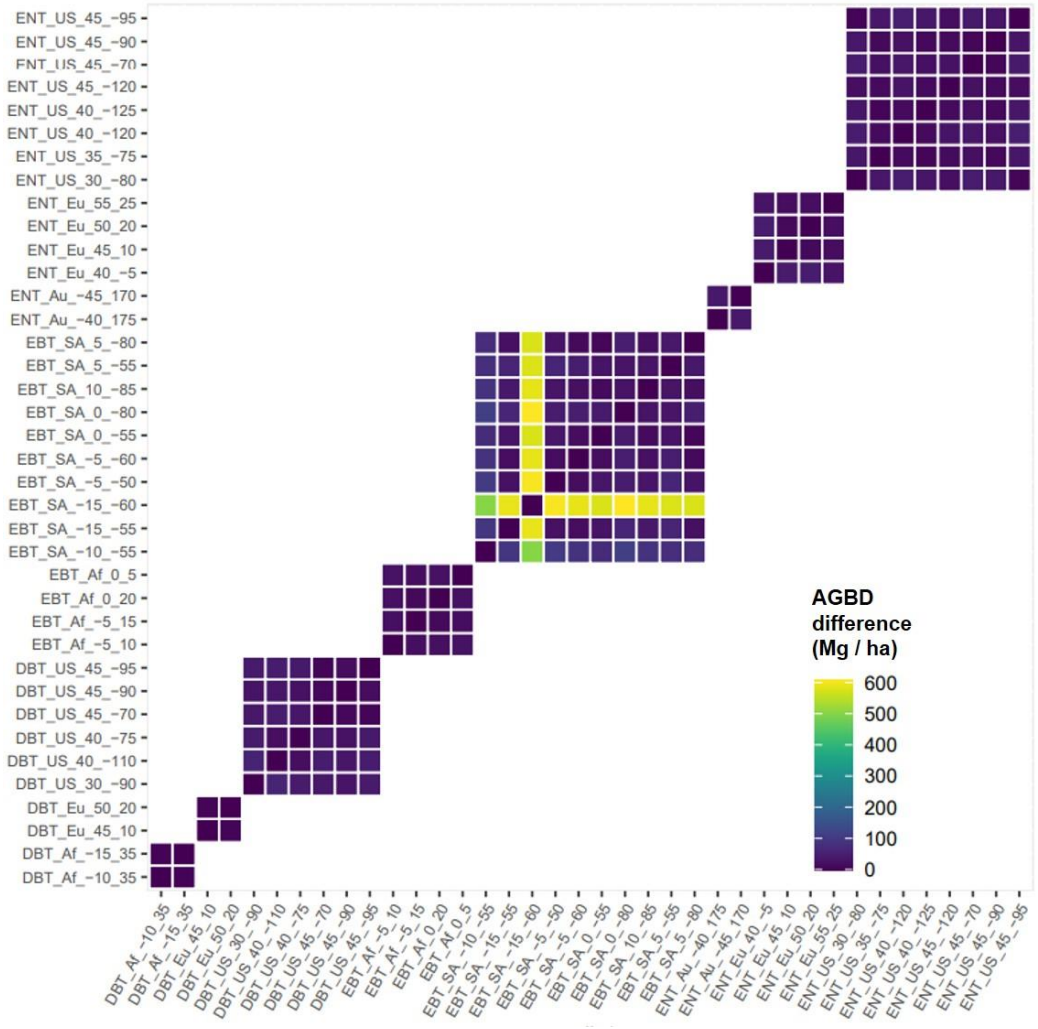

Figure S7. Difference in AGBD predictions from local models without regularization based on Version 1 predictors (i.e., 2 RH metrics). Each cell on the figure represents a pairwise AGBD difference from two local models. Each column represents a focal model. On-orbit GEDI footprints used for AGBD predictions came from the stratum of the focal model.

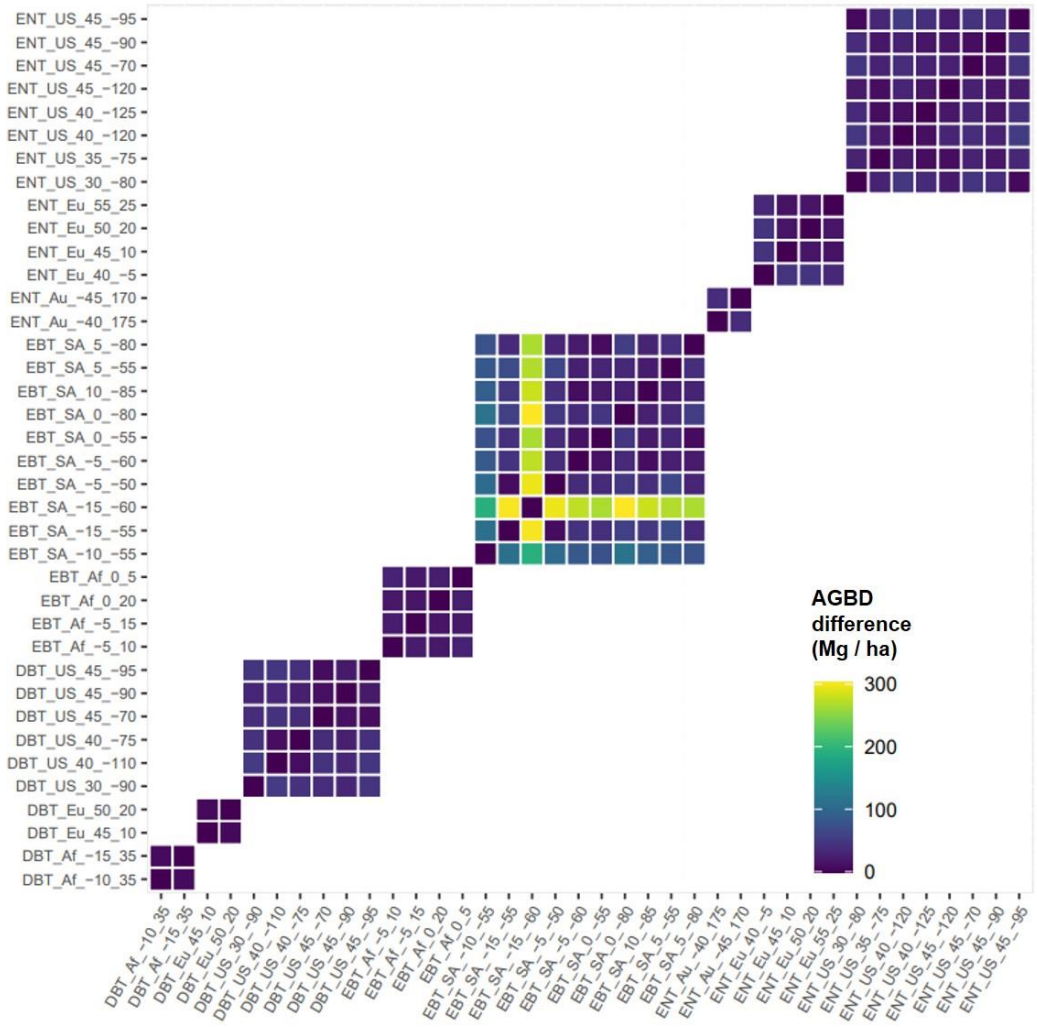

Figure S8. Difference in AGBD predictions from local models with L2 regularization based on Version 1 predictors (i.e., 2 RH metrics). Each cell on the figure represents a pairwise AGBD difference from two local models. Each column represents a focal model. On-orbit GEDI footprints used for AGBD predictions came from the stratum of the focal model.

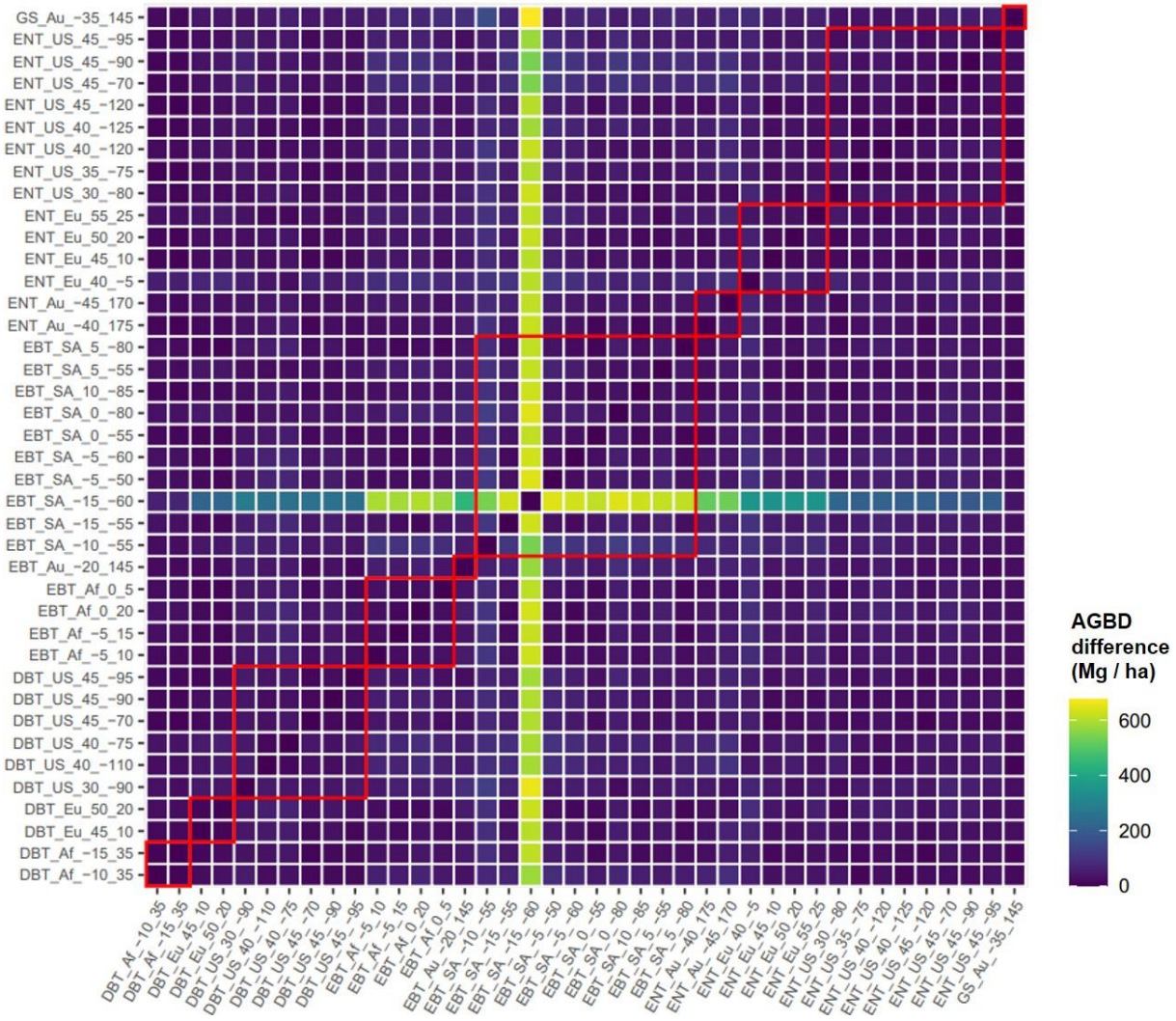

Figure S9. Difference in AGBD predictions from local models without regularization based on Version 2 predictors (i.e., 5 RH metrics). Each cell on the figure represents a pairwise AGBD difference from two local models. Each column represents a focal model. On-orbit GEDI footprints used for AGBD predictions came from the stratum of the focal model.

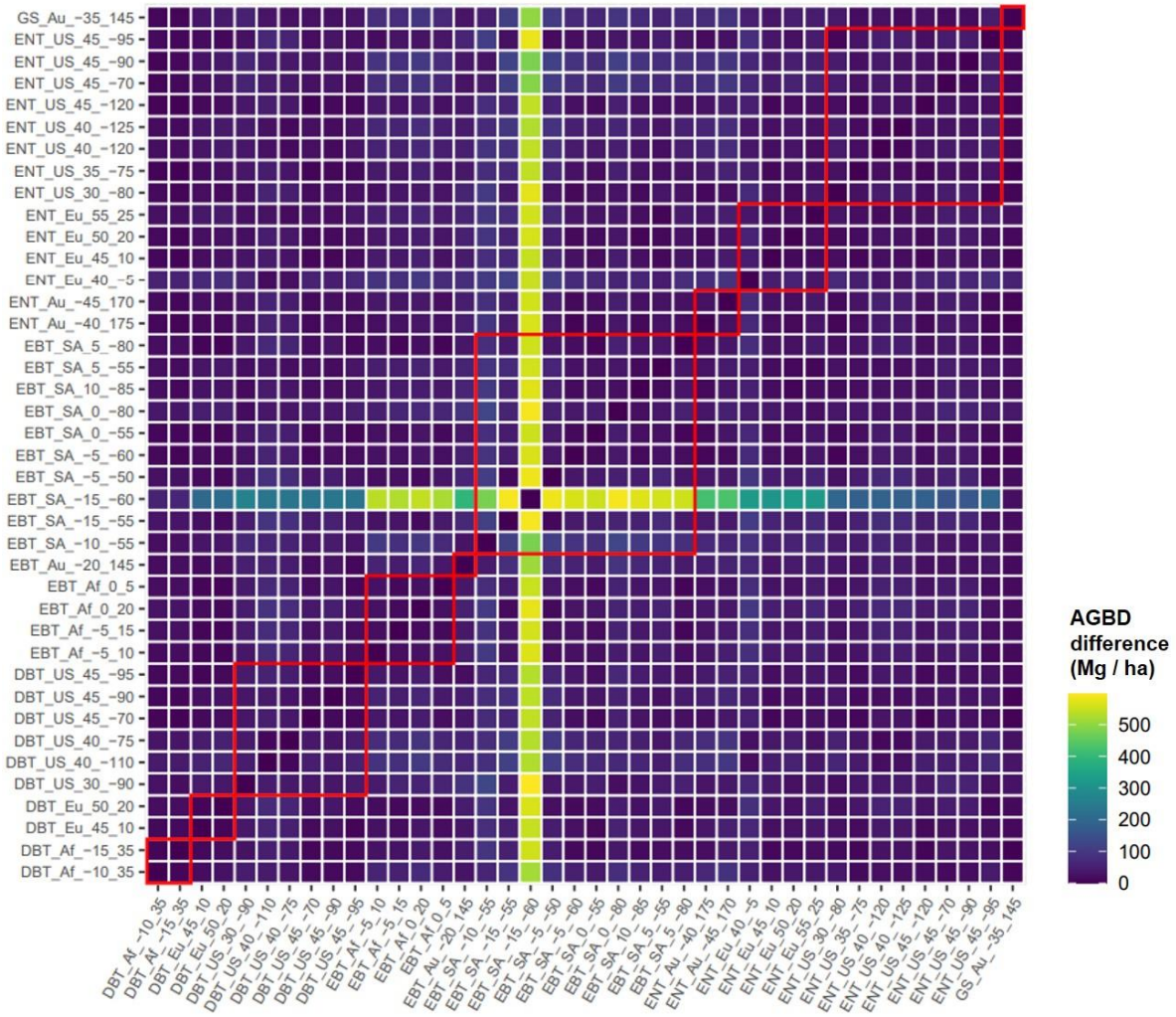

Figure S10. Difference in AGBD predictions from local models with L2 regularization based on Version 2 predictors (i.e., 5 RH metrics). Each cell on the figure represents a pairwise AGBD difference from two local models. Each column represents a focal model. On-orbit GEDI footprints used for AGBD predictions came from the stratum of the focal model.

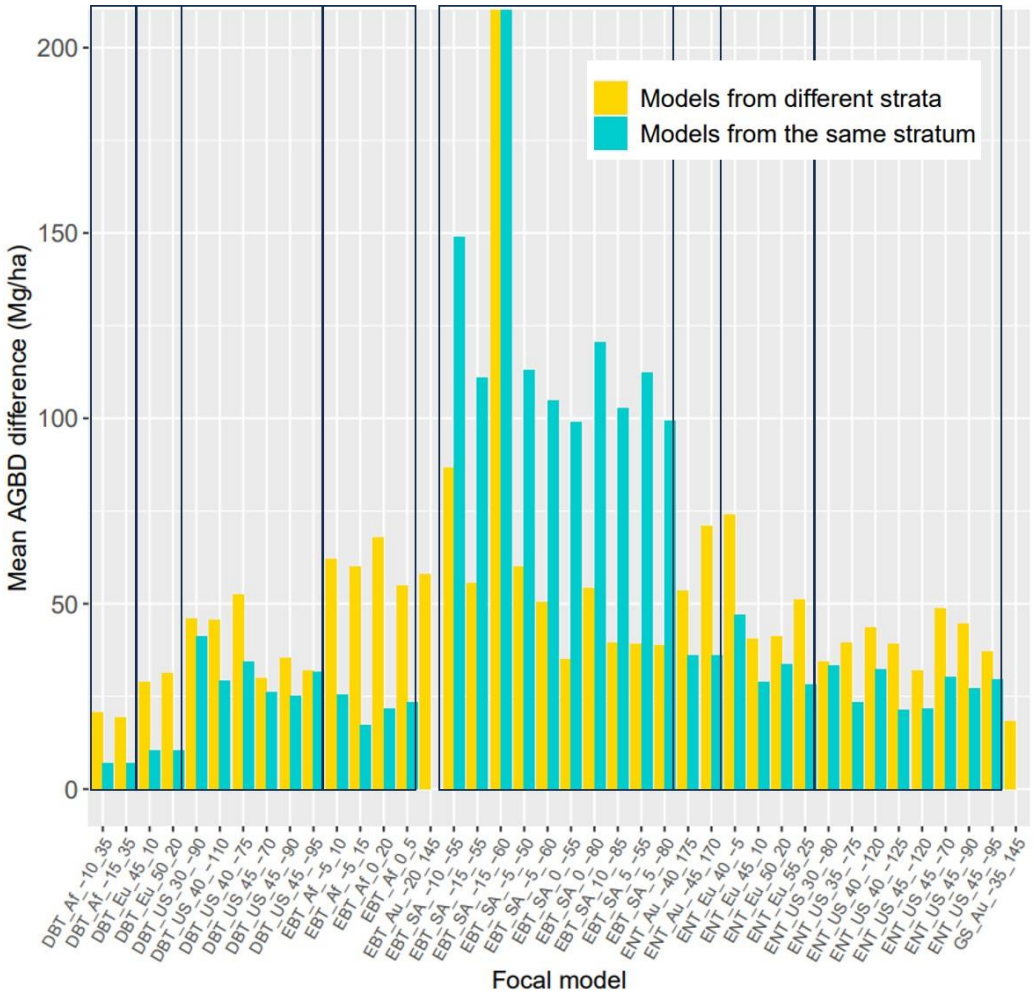

Figure S11. Mean AGBD difference from local models in the same or different strata without regularization based on Version 2 predictors (i.e., 5 RH metrics). The mean AGBD difference was calculated for each focal model based on pairwise difference within and without the red bounding box in Figure 6. Black bounding boxes represent prediction strata with more than one local model. The bars for EBT_SA_-15_-60 were cut off; the yellow bar was at 602.67 Mg / ha, and the cyan bar was at 616.05 Mg / ha.

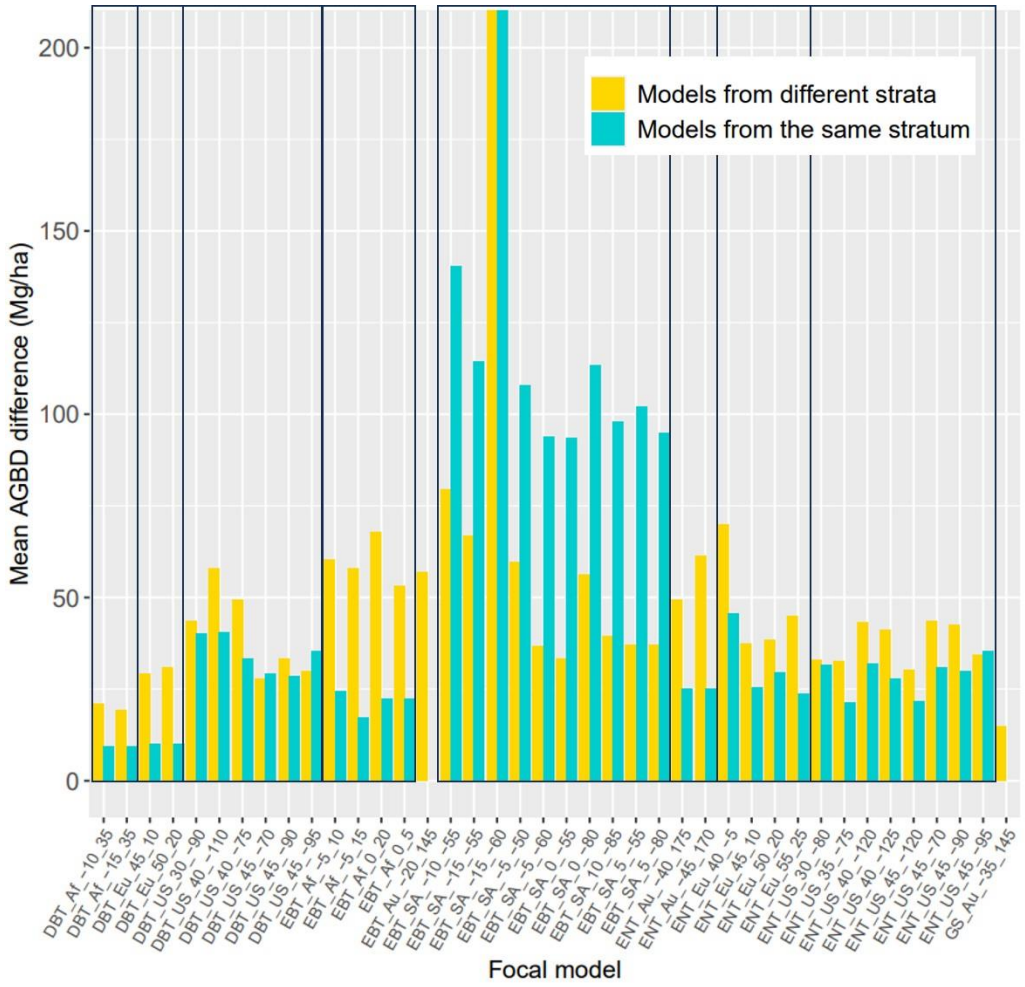

Figure S12. Mean AGBD difference from local models in the same or different strata with L2 regularization based on Version 2 predictors (i.e., 5 RH metrics). The mean AGBD difference was calculated for each focal model based on pairwise difference within and without the red bounding box in Figure 6. Black bounding boxes represent prediction strata with more than one local model. The bars for EBT_SA_-15_-60 were cut off; the yellow bar was at 543.65 Mg / ha, and the cyan bar was at 559.26 Mg / ha.